UNIVERSITY OF OKLAHOMA

GRADUATE COLLEGE

THE IMPACT OF SURFACE HETEROGENEITY ON SURFACE FLUX ESTIMATES OF THE STABLE BOUNDARY LAYER USING SINGLE COLUMN MODELING

A THESIS

SUBMITTED TO THE GRADUATE FACULTY

in partial fulfillment of the requirements for the

Degree of

MASTER OF SCIENCE IN METEOROLOGY

By

DOMINIC CANDELA
Norman, Oklahoma
2022

THE IMPACT OF SURFACE HETEROGENEITY ON SURFACE FLUX ESTIMATES OF THE STABLE BOUNDARY LAYER USING SINGLE COLUMN MODELING

A THESIS APPROVED FOR THE
SCHOOL OF METEOROLOGY

BY THE COMMITTEE CONSISTING OF

Dr. Scott Salesky, Chair

Dr. Jeremy A. Gibbs

Dr. James Ruppert

Acknowledgments

Firstly, the work here would not be possibly without the support of funding through NSF award number AGS-1660367. I am very grateful for the support through my graduate studies.

I would like to thank my committee members, Dr. Jeremy Gibbs, Dr. Scott Salesky, and Dr. James Ruppert. Their comments and suggestions improved the quality of this paper and contributed towards making this a stronger thesis. I would also like to thank Dr. Rob Stoll, who laid a foundation for this work and whose thoughts and recommendation were especially helpful in understanding surface heterogeneity.

Am especially grateful to Dr. Jeremy Gibbs, who has always been available for me to pick his brain through coding, academics, and life. Only two short years ago in the middle of a pandemic he took on a student who had no real programming experience. Jeremy has been there every step of the way, through debugging my coding issues which, even when the "world-ending" issues were solved by changing a 0.5 to a 1. I've learned so much being able to with Jeremy as an advisor and mentor and I'm lucky to have been able to work with an incredible scientist and human.

Also to my family who have always supported me, no matter what choices I have made in my career. Without my family's support I would not have been able to make it as far as I have today. They have sacrificed so much for me to get to where I am and I am forever grateful to them. Finally, thanks to my friends who have continued to support me in my studies.

Table of Contents

Acknowledgments **iv**

List Of Tables **vii**

List Of Figures **viii**

Abstract **xiii**

1 Introduction **1**
1.1 Motivation 1
1.2 The Single Column Model 2
1.3 Goals 4
1.4 Outline 5

2 Model Parameterization **6**
2.1 Surface Layer (SL) Schemes 6
2.1.1 Monin-Obukhov Similarity Theory (MOST) 7
2.1.2 Empirical Businger-Dyer 9
2.1.3 Tile Model (TM) 11
2.1.4 Modified Tile Model (MTM) 12
2.1.5 Surface Roughness Model (RM) 14
2.2 Planetary Boundary Layer (PBL) Schemes 15
2.2.1 First-Order Schemes 16
2.2.1.1 ECMWF 16
2.2.2 1.5-Order Schemes 18
2.2.2.1 Mellor-Yamada Janjic (MYJ) 20
2.2.2.2 Mellor-Yamada Nakanishi-Niino (MYNN) 23

3 Model Setup **28**
3.1 Single Column Model 28
3.2 Numerical Implementation of SCM 30
3.2.1 Computational Grid 30
3.3 Numerical Schemes 31
3.3.1 Runge-Kutta III 32
3.3.2 Crank–Nicolson 32

4 Validation of SCM against GABLS1 **35**
4.1 Introduction . . . 35
4.2 Surface Temperature Differences . . . 37
4.2.1 Time Series . . . 37
4.2.2 Vertical Profiles . . . 48
4.3 Roughness Differences . . . 62
4.4 Discussion . . . 70

5 Validation of SCM against GABLS2 **73**
5.1 Introduction . . . 73
5.2 Surface Temperature Differences . . . 76
5.2.1 Time Series . . . 76
5.2.2 Vertical Profiles . . . 88
5.3 Roughness Differences . . . 96
5.4 Discussion . . . 101

6 Validation of SCM against BLISSFUL **103**
6.1 Introduction . . . 103
6.2 Results . . . 111
6.2.1 Vertical Profiles . . . 111
6.2.2 Time Series . . . 119
6.3 Roughness Differences . . . 121
6.4 Discussion . . . 126

7 Summary and Conclusions **128**
7.1 Closing Remarks . . . 128
7.2 Future Work . . . 130

Reference List **133**

List Of Tables

4.1 Surface cooling rates for the homogeneous case, as well as for the two patches when using temperature heterogeneity of 3K and 6K. 36

4.2 Mean values for the final hour of the simulation using surface temperature heterogeneity for the boundary layer height (h), Obukhov Length (L), friction velocity (u_*), surface heat flux ($\langle w'\theta' \rangle$) and surface momentum flux ($\langle u'w' \rangle$). 47

4.3 Mean values for the final hour of the simulation using z_0 heterogeneity for the effective roughness length (z_{0e}), boundary layer height (h), Obukhov Length (L), friction velocity (u_*), surface heat flux ($\langle w'\theta' \rangle$) and surface momentum flux ($\langle u'w' \rangle$). Here z_{01} is the roughness length for patch 1, and z_{02} for patch 2. 64

5.1 Mean values during the hour prior to surface heating using surface temperature heterogeneity for the boundary layer height (h), Obukhov Length (L), friction velocity (u_*), surface heat flux ($\langle w'\theta' \rangle$) and surface momentum flux ($\langle u'w' \rangle$). 88

5.2 Mean values during the hour prior to surface heating using z_0 heterogeneity for the effective roughness length (z_{0e}), boundary layer height (h), Obukhov Length (L), friction velocity (u_*), surface heat flux ($\langle w'\theta' \rangle$) and surface momentum flux ($\langle u'w' \rangle$). Here z_{01} is the roughness length for patch 1, and z_{02} for patch 2. 97

6.1 Mean values for the final hour of the simulation using surface temperature heterogeneity for the boundary layer height (h), Obukhov Length (L), friction velocity (u_*), surface heat flux ($\langle w'\theta' \rangle$) and surface momentum flux ($\langle u'w' \rangle$). 118

6.2 Mean values for the final hour of the simulation using z_0 heterogeneity for the effective roughness length (z_{0e}), boundary layer height (h), Obukhov Length (L), friction velocity (u_*), surface heat flux ($\langle w'\theta' \rangle$) and surface momentum flux ($\langle u'w' \rangle$). Here z_{01} is the roughness length for patch 1, and z_{02} for patch 2. 125

List Of Figures

3.1 Schematic of the numerical grid used in the SCM as well as where certain variables are located. 31

4.1 Time series of the boundary layer height (top) and Obukhov length (bottom) with the homogeneous case (solid) and surface heterogeneity with the TM with 3K patches (dashed), and the MTM with 3K patches (dotted). The ECMWF model is colored black, the MYJ blue, and the MYNN red. The shaded grey represents the spread of the LES from GABLS1. 39
4.2 Same as previous but for 6K patches. 40
4.3 Time series of the friction velocity (top) and surface kinematic heat flux magnitude (bottom) with the homogeneous case (solid) and the TM with 3K patches (dashed). The ECMWF model is colored black, the MYJ blue, and the MYNN red. The shaded grey represents the spread of the LES from GABLS1. 42
4.4 Same as previous but for 6K patches. 43
4.5 Time series of the friction velocity (top) and surface kinematic heat flux magnitude (bottom) with the homogeneous case (solid), the TM with 3K patches (dashed), and the MTM with 3K patches (dotted). The ECMWF model is colored black, the MYJ blue, and the MYNN red. The shaded grey represents the spread of the LES from GABLS1. . . . 45
4.6 Same as previous but for 6K patches. 46
4.7 Vertical profile of the wind speed (top-left), potential temperature (top-right), kinematic heat flux (bottom-left), and kinematic momentum flux (bottom-right) averaged over the final hour of the simulation for the homogeneous case (solid) and the TM with 3K patches (dashed). The ECMWF model is colored black, the MYJ blue, and the MYNN red. The shaded grey represents the spread of the LES from GABLS1. . . . 51
4.8 Same as previous but for 6K patches. 52
4.9 Vertical profile of the wind speed (top-left), potential temperature (top-right), kinematic heat flux (bottom-left), and kinematic momentum flux (bottom-right) averaged over the final hour of the simulation for the homogeneous case (solid), the TM with 3K patches (dashed), and the MTM with 3K patches (dotted). The ECMWF model is colored black, the MYJ blue, and the MYNN red. 54
4.10 Same as previous but for 6K patches. 55

4.11 Vertical profile of the eddy diffusivities for heat and momentum for the homogeneous case (solid) and the TM with 6K patches (dashed). The ECMWF model is colored black, the MYJ blue, and the MYNN red. . 56
4.12 Vertical profile of the bulk turbulent Prandtl number for the homogeneous case (solid) and the TM with 6K patches (dashed). The ECMWF model is colored black, the MYJ blue, and the MYNN red. 57
4.13 Vertical profiles of the turbulence length scale (left) and TKE (right) for the homogeneous case (solid) and the TM with 6K patches (dashed). The ECMWF model is colored black, the MYJ blue, and the MYNN red. 60
4.14 Vertical profiles of the various length scales from the MYNN scheme that define the turbulence length scale (red) including the surface length scale (blue), ABL based length scale (green), and buoyancy length scale (orange). 61
4.15 Time series of the boundary layer height (top) and Obukhov length (bottom) with the homogeneous case (solid) and surface heterogeneity for patch 2 values of $z_{02} = 0.01\,\mathrm{m}$ (dotted) and $z_{02} = 0.001\,\mathrm{m}$ (dashed). The ECMWF model is colored black, the MYJ blue, and the MYNN red. The shaded grey represents the spread from the LES of GABLS1. 66
4.16 Time series of the friction velocity (top) and surface kinematic heat flux (bottom) with the homogeneous case (solid) and surface heterogeneity for patch 2 values of $z_{02} = 0.01\,\mathrm{m}$ (dotted) and $z_{02} = 0.001\,\mathrm{m}$ (dashed). The ECMWF model is colored black, the MYJ blue, and the MYNN red. The shaded grey represents the spread from the LES of GABLS1. 67
4.17 Vertical profile of the wind speed(top-left), potential temperature (top-right), kinematic heat flux (bottom-left), and kinematic momentum flux (bottom-right) with the homogeneous case (solid) and surface heterogeneity for patch 2 values of $z_{02} = 0.01\,\mathrm{m}$ (dotted) and $z_{02} = 0.001\,\mathrm{m}$ (dashed). The ECMWF model is colored black, the MYJ blue, and the MYNN red. The shaded grey represents the spread from the LES of GABLS1. 69

5.1 Initial profiles of the potential temperature (top), surface temperature (middle), and TKE (bottom) for the GABLS2 case. 75
5.2 Time series of the surface potential temperature (top) and wind speed (bottom) for the homogeneous case (solid), the TM with 3K patches (dotted), and 6K patches (dashed). The ECMWF model is colored black, the MYNN red, and the shaded grey represents the spread of the SCM models from GABLS2. 78
5.3 Time series of the surface potential temperature (top) and wind speed (bottom) for the homogeneous case (solid), the TM with 3K patches (dashed), and MTM with 3K patches (dotted). The ECMWF model is colored black, the MYNN red, and the shaded grey represents the spread of the SCM models from GABLS2. 80

5.4 Time series of the surface potential temperature (top) and wind speed (bottom) for the homogeneous case (solid), the TM with 6K patches (dashed), and MTM with 6K patches (dotted). The ECMWF model is colored black, the MYNN red, and the shaded grey represents the spread of the SCM models from GABLS2. 81
5.5 Time series of the friction velocity (top) and sensible heat flux (bottom) for the homogeneous case (solid), the TM with 3K patches (dotted), and 6K patches (dashed). The ECMWF model is colored black, the MYNN red, and the shaded grey represents the spread of the SCM models from GABLS2. 83
5.6 Time series of the friction velocity (top) and sensible heat flux (bottom) for the homogeneous case (solid), the TM with 3K patches (dotted), and 6K patches (dashed) focused on the period from 20 LT to 05 LT. The ECMWF model is colored black, the MYNN red, and the shaded grey represents the spread of the SCM models from GABLS2. 84
5.7 Time series of the friction velocity (top) and sensible heat flux (bottom) for the homogeneous case (solid), the TM with 3K patches (dashed), and the MTM with 3K patches (dotted). The ECMWF model is colored black, the MYNN red, and the shaded grey represents the spread of the SCM models from GABLS2. 85
5.8 Time series of the friction velocity (top) and sensible heat flux (bottom) for the homogeneous case (solid), the TM with 6K patches (dashed), and the MTM with 6K patches (dotted). The ECMWF model is colored black, the MYNN red, and the shaded grey represents the spread of the SCM models from GABLS2. 86
5.9 Time series of TKE for the homogeneous case (solid), the TM with 3K patches (dotted) and 6K patches (dashed). The shaded grey represents the spread of the SCM models from GABLS2. 87
5.10 Same as above but focused on the period from 20 LT to 05 LT. 87
5.11 Vertical profiles of potential temperature (left) and wind speed (right) at 05 LT for the homogeneous case (solid), the TM with 6K patches (dashed). The ECMWF model is colored black, and the MYNN red. The shaded grey represents the spread of the SCM models from GABLS2. 90
5.12 Vertical profiles of potential temperature (left) and wind speed (right) at 05 LT for the homogeneous case (solid), the TM with 6K patches (dashed), and the MTM with 6K patches (dotted). The ECMWF model is colored black, and the MYNN red. The shaded grey represents the spread of the SCM models from GABLS2. 91
5.13 Vertical profiles of potential temperature (left) and wind speed (right) at 14 LT for the homogeneous case (solid), the TM with 6K patches (dashed), and the MTM with 6K patches (dotted). The ECMWF model is colored black, and the MYNN red. The shaded grey represents the spread of the SCM models from GABLS2. 93

5.14 Vertical profile of TKE at 14 LT for the MYNN (red) and MYNN 6K (dashed red) cases. The shaded grey represents the spread of the SCM models from GABLS2. 95
5.15 Time series of the friction velocity (top) and sensible heat flux (bottom) with the homogeneous case (solid) and surface heterogeneity for patch values of $z_0 = 0.3\,\mathrm{m}$ (dashed) and $z_0 = 0.0003\,\mathrm{m}$ (dotted). The ECMWF model is colored black, the MYNN red, and the shaded grey represents the spread of the SCM models from GABLS2. 98
5.16 Time series of the potential temperature (top) and wind speed (bottom) with the homogeneous case (solid) and surface heterogeneity for patch values of $z_0 = 0.3\,\mathrm{m}$ (dashed) and $z_0 = 0.0003\,\mathrm{m}$ (dotted). The ECMWF model is colored black, the MYNN red, and the shaded grey represents the spread of the SCM models from GABLS2. 99
5.17 Vertical profiles of wind speed (left) and potential temperature (right) at 14 LT with the homogeneous case (solid) and surface heterogeneity for patch values of $z_0 = 0.3\,\mathrm{m}$ (dashed) and $z_0 = 0.0003\,\mathrm{m}$ (dotted). The ECMWF model is colored black, and the MYNN red. 100

6.1 Dr. Jeremy Gibbs, Dr. Elizabeth Smith, Dr. Tyler Bell, and author at the LEMS 03 location. 105
6.2 Surface potential temperature from the LEMS (red) and the Washington mesonet site (blue) from July 6, 16 UTC to July 7, 16 UTC (top) and the focused period during the simulation from July 7, 02 UTC to July 7, 10 UTC (bottom). 107
6.3 Vertical profiles of the two different soundings of wind speed on the top are shown at July 6, 23:30 UTC (black) and July 7, 10:30 UTC (green) and the forcing used in the simulations (dashed black). On the bottom is the initial profiles of potential temperature from the AERI (orange) and coptersonde (red) at July 7, 02 UTC and the initial profile used in the model (blue). 108
6.4 LEMS 04 location next to the Washington Mesonet site with Dr. Elizabeth Smith pictured. 110
6.5 Vertical profiles of wind speed (left) and potential temperature (right) averaged over the final hour of the simulation using no nudging (dashed) and nudging (solid). The ECMWF model is colored black, the MYJ blue, and the MYNN red along with observations from the Doppler Lidar (grey) and retrievals from the AERI (dark purple). 112
6.6 Same as previous but the vertical axis has changed to $z \in [0, 200]$. . . . 113
6.7 Vertical profiles of the kinematic momentum flux (left) and kinematic heat flux (right) averaged over the final hour of the simulation using no nudging (dashed) and nudging (solid). The ECMWF model is colored black, the MYJ blue, and the MYNN red. 114
6.8 Same as previous but the vertical axis has changed to $z \in [0, 200]$. . . . 115

6.9 Vertical profiles of wind speed (left) and potential temperature (right) averaged over the final hour of the simulation for the homogeneous case (solid) and the TM with 6K patches (dashed). The ECMWF model is colored black, the MYJ blue, and the MYNN red. 116
6.10 Vertical profiles of kinematic momentum flux (left) and kinematic heat flux (right) averaged over the final hour of the simulation for the homogeneous case (solid) and the TM with 6K patches (dashed). The ECMWF model is colored black, the MYJ blue, and the MYNN red. . 117
6.11 Time series of the friction velocity and surface kinematic heat flux with the homogeneous case (solid) and using the TM with 6K patches (dashed). The ECMWF model is colored black, the MYJ blue, and the MYNN red. 120
6.12 Time series of the boundary layer height and Obukhov length with the homogeneous case (solid) and using the TM with 6K patches (dashed). The ECMWF model is colored black, the MYJ blue, and the MYNN red.121
6.13 Vertical profiles of wind speed (left) and potential temperature (right) averaged over the final hour of the simulation with the homogeneous case (solid) and surface heterogeneity for patch values of $z_{02} = 0.01\,\mathrm{m}$ (dotted) and $z_{02} = 0.001\,\mathrm{m}$ (dashed). The ECMWF model is colored black, the MYJ blue, and the MYNN red. 123
6.14 Time series of the friction velocity and surface kinematic heat flux with the homogeneous case (solid) and surface heterogeneity for patch values of $z_{02} = 0.01\,\mathrm{m}$ (dotted) and $z_{02} = 0.001\,\mathrm{m}$ (dashed). The ECMWF model is colored black, the MYJ blue, and the MYNN red. 124

Abstract

The surface fluxes of momentum and heat play an important role in the evolution of the atmospheric boundary layer (ABL). Accurate representation of the fluxes in weather and climate forecasting models, especially when dealing with heterogeneous land surfaces. This is complicated under stable conditions where the fluxes are often smaller in magnitude and turbulence cannot be relied on to mix out the heterogeneity effects. Here the role of surface heterogeneity in determining the average surface fluxes is investigated through the development of a single column model (SCM) in Python. The SCM features some of the most popular PBL scheme currently implemented in the Weather Research and Forecasting model (WRF) as well as various surface layer (SL) parameterizations that can account for surface heterogeneity.

The SCM is validated against with three different cases with varying complexities. The first two cases, GABLS1 and GABLS2, are idealized atmospheric boundary layer studies that have been well cited in the literature. The third case used with the SCM is from a recent field project during the summer of 2021 by the Boundary Layer Integrated Sensing and Simulation (BLISS) group at the University of Oklahoma, where multiple different boundary layer observational instruments were deployed.

The role of heterogeneity on flux properties was investigated by altering the type and strength of the surface heterogeneity. Both surface temperature heterogeneity and surface roughness heterogeneity are investigated with the current surface models implemented in the SCM. It was found that both types of surface heterogeneity impacted the magnitude of the surface fluxes of heat and momentum, especially under stable conditions. The surface temperature heterogeneity impacted the surface heat fluxes more significantly than the surface momentum fluxes. With surface roughness heterogeneity, the surface fluxes of heat and momentum were impacted equally. Future expansion to this work is discussed including further additions to the SCM.

Chapter 1

Introduction

1.1 Motivation

The turbulent fluxes at the earth's surface must be known in order to correctly set the bottom boundary conditions for numerical weather and climate forecasting models. These fluxes are generally not known, so either a land surface model must be used that couples the land surface to the atmosphere or the fluxes must be prescribed and calculated. As land surface models are difficult to implement, one approach is to use Monin-Obukhov similarity theory (MOST; Monin and Obukhov 1954), which has been used extensively and proven successful in the literature. MOST theory gives a simple relation for the surface fluxes of heat and momentum by relating them to their respective non-dimensionalized gradients, which are universal functions.

MOST relies on four key assumptions: stationary flow, high Reynolds number flow, the flow is horizontally homogeneous, and flow restricted to the surface layer. This works for most situations, but the assumption of horizontally homogeneity can break down. The spatial distribution of surface roughness and temperature is highly variable. Stable conditions further complicate the issue because the fluxes of heat and momentum can be very small, turbulence can be intermittent, and vertical mixing inhibited. Accordingly, surface heterogeneity becomes more important under these conditions because turbulence may not mix out the large-scale effects of such heterogeneity.

Today there are numerous PBL schemes that have been developed with varying degrees of complexity. While each PBL scheme is parameterized differently, each of the schemes need to have some information about the fluxes at the underlying surface. Therefore the surface-layer (SL) model can be interchanged between PBL schemes, allowing for investigation of how surface heterogeneity impacts the surface fluxes under stable condition.

1.2 The Single Column Model

A simplified model is used to investigate the role of surface heterogeneity in determining the surface fluxes. Instead of running a three-dimensional simulation, the model is run in just the vertical dimension. This is known as single-column modeling (SCM) and has been used in testing parameterization schemes for numerical weather models in recent years (Bogenschutz et al., 2020). In a SCM, the model is run in isolation with prescribed atmospheric dynamics. In this case it allows us to investigate differences between turbulence parameterizations by isolating the model to only include effects from the PBL (i.e. no radiation or microphysical schemes are used).

While other SCMs have been developed, a user can get lost in choosing schemes without the understating of the principles behind the model closure. To gain a stronger understanding of the intricacies in the parameterization of turbulence and surface schemes, the OU-NSSL SCM was developed from scratch. Additionally, other SCMs may be too complex to study the current problem, or are lacking the features desired to investigate it. With these thoughts in mind, the popular programming language Python was chosen here, leveraging the object-oriented programming approach of Python to create a flexible SCM.

The SCM features some of the more popular PBL schemes: European Centre for Medium-Range Weather Forecasts (ECMWF; Louis et al. 1982), Mellor-Yamada Janjic (MYJ; Janjic 2002), Mellor-Yamada Nakanishi-Niino (MYNN; Nakanishi and Niino 2009). Each of these PBL models have been used frequently over the years and available in the popular numerical weather prediction model The Weather Research and Forecasting (WRF) model (Skamarock et al., 2021). Each of the PBL schemes uses an eddy diffusivity type model to parameterize the fluxes of momentum and heat. The ECMWF is considered a first-order model, where all moments higher than first order must be parameterized. The MYJ and MYNN schemes are more advanced than the ECMWF scheme and considered 1.5-order, as MYJ and MYNN have an extra prognostic equation for turbulence kinetic energy (TKE).

Additionally four different surface layer schemes are available: Monin-Obukhov Similarity Theory (MOST; Monin and Obukhov 1954), Tile Model (TM; Stoll and Porté-Agel 2009), Modified Tile Model (MTM; Stoll and Porté-Agel 2009), and Surface Roughness Model (RM; Miller and Stoll 2013). The core of each model is based upon MOST, but modifications are made to account for non-validity of horizontally homogeneous flow. The TM and MTM are both focused on accounting for surface temperature heterogeneity by locally applying MOST over homogeneous subareas, then summing each subareas together to get a total flux. The RM uses a different approach for surface roughness heterogeneity by calculating an effective roughness length parameter based on the homogeneous subareas. This parameter is then used to calculate the fluxes from classic MOST.

1.3 Goals

The turbulent fluxes and their interaction with the surface play an import role in determining profiles and time tendencies of heat, momentum, and moisture in the boundary layer. The transport and interaction of turbulent fluxes in the boundary layer are done through turbulent eddies of various size. Some eddies are not resolved by the numerical mesh and must be parameterized. There are a variety of ways to account for these unresolved motions in modern closures.

Characterizing turbulence at the surface is an equally difficult problem. The fluxes at the surface must be either set by a land surface model that solves for the fluxes based on the coupling of the land to the atmosphere, or prescribed in some way based on the surface temperature or surface heat flux. In addition, with stable conditions turbulence is often intermittent and weaker, making the fluxes of heat and momentum small in comparison to convective conditions. Stable conditions further complicate things as turbulence cannot be relied on to mix out the effects of surface heterogeneity, as can be done during convective conditions. Previous work by Stoll and Porté-Agel (2009) looked at the impact of surface heterogeneity on regional scale fluxes in the ABL under stable conditions with the TM and MTM. With the TM it was found that the surface kinematic heat fluxes can have the wrong sign. Additionally the warmer (unstable) patch can end up dominating the surface heat flux calculations, especially with strong advection. The MTM was implemented to correct for this and found to improve the surface kinematic heat fluxes by improving the surface heat flux calculation of the cold (stable). Additionally, Miller and Stoll (2013) studied the effects of roughness transitions on surface fluxes in the heterogeneous stable boundary layer. They found that existing models are unable to accurately reproduce both the values of the effective roughness length and their trends as functions of patch length scale and stability.

Here the TM, MTM, and RM are used to investigate the impact surface heterogeneity has on surface flux estimations in stable boundary layer. While Stoll and Porté-Agel (2009) and Miller and Stoll (2013) previously used turbulence closure models that are focused towards research, here the heterogeneity accounting surface models are applied with popular turbulence schemes that are currently used in weather and climate forecasting models. The SCM developed provides a simple way to study this with the flexibility to add different turbulence and surface layer schemes easily. Based on the findings, a recommendation will be made on the best combination of PBL and SL schemes that account for land surface heterogeneity to use with operational weather and climate models.

1.4 Outline

Chapter 2 will discuss in detail the different turbulence and surface layer schemes that have been implemented in the OU-NSSL SCM. This includes a full mathematical description of each scheme and how they are implemented in the SCM. In Chapter 3 a description of the SCM is given, including details of the model grid and numerical methods. Chapters 4-6 prevent the results from the SCM for three different test cases. Two of the cases are well-cited atmospheric boundary layer studies from GABLS1 and GABLS2 while the third case is from a recent field campaign conducted at OU during the summer of 2021. Chapter 7 focuses on a discussion of the importance of the results in Chapters 4-6 and a path forward for future research on the topic.

Chapter 2

Model Parameterization

The parameterization of turbulence is at the core of accurate numerical weather prediction. Current numerical weather prediction run with various sorts of parameterization schemes including radiation schemes, cloud microphysics schemes, land-surface schemes, and turbulence schemes. In this thesis, the focus is on the impact surface-layer schemes that can account for heterogeneity have on the choice of turbulence parameterization scheme.

2.1 Surface Layer (SL) Schemes

The surface layer (SL) scheme provides fluxes of momentum and heat as lower boundary conditions to the PBL scheme. The SL schemes can be thought of as setting the lower boundary conditions for the boundary layer schemes. In this way the surface boundary conditions and are not tied to an individual boundary layer scheme and can be interchanged with PBL schemes. Here we are not coupling the surface to the atmosphere as is done in a LSM. The fluxes are diagnosed by using MOST, but this does not modify the atmosphere directly as a LSM would.

In this section, four SL models are discussed, including MOST, the Tile Model (TM), the Modified Tile Model (MTM), and the Surface Roughness Model (SRM). The TM scheme uses MOST, but applies it locally over homogeneous tiles to obtain surface fluxes. The MTM uses the blending height and new stability functions for

stable conditions to improve the surface heat flux estimations. The SRM calculates an effective roughness length based upon the surface roughness for each patch which is then used in MOST.

2.1.1 Monin-Obukhov Similarity Theory (MOST)

Monin and Obukhov (1954) hypothesized that in the surface layer the fluxes of heat and momentum can be related to the mean dimensionless mean velocity and temperature gradients as universal functions of z/L when the mean flow variables and turbulent quantities are normalized by their respective non-dimensionalized surface scales. Additionally MOST relies on four assumption: stationary flow, high Reynolds number flow, the flow is horizontally homogeneous, and flow restricted to the surface layer. Here z is the vertical distance above the surface and L is a stability parameter called the Obukhov Length defined as

$$L = -\frac{\theta_0 {u_*}^3}{\kappa g \langle w'\theta' \rangle_s} \tag{2.1}$$

where u_* is the friction velocity, θ_0 is a reference potential temperature, g is gravity, κ is the von Kármán constant, and $\langle w'\theta' \rangle_s$ is the surface heat flux. The $(...)'$ term represents a fluctuating quantity where Reynolds averaging is used so that $(...)$ is decomposed into a mean and fluctuating quantity, $(...) = \langle (...) \rangle + (...)'$. The Obukhov length is a length scale based on surface layer variables that when compared to the the height scale z represents the stability of the atmosphere in the atmospheric surface layer. Under unstable or convective conditions, L is negative as the surface heat flux $\langle w'\theta' \rangle$ is positive. Under neutral conditions the Obukhov length is undefined as the surface heat flux is zero. For stably stratified conditions the Obukhov length is positive. In the atmospheric surface layer, the lowest 10% of the BL, the Obukhov length is considered constant under the assumption that the fluxes are constant with height.

The friction velocity is also known as the turbulent velocity scale and is defined as

$$u_* = (-\langle u'w' \rangle)^{1/2}, \tag{2.2}$$

where $\langle u'w' \rangle$ is the surface momentum flux, along with the relevant turbulent scale for temperature

$$\theta_* = -\frac{\langle w'\theta' \rangle}{u_*}. \tag{2.3}$$

Following MOST, the gradients of potential temperature and wind speed are written as empirically derived universal functions of $\zeta = z/L$,

$$\phi_m(\zeta) = \frac{\kappa z}{u_*}\frac{\partial U}{\partial z} \tag{2.4}$$

$$\phi_h(\zeta) = \frac{\kappa z}{\theta_*}\frac{\partial \theta}{\partial z}. \tag{2.5}$$

The turbulence scales u_* and θ_* can be related to the kinematic surface flux values as

$$\langle \tau \rangle_s = -u_*^2 \tag{2.6}$$

$$\langle w'\theta' \rangle_s = -u_*\theta_* \tag{2.7}$$

Equations 2.38 and 2.39 can be integrated and solved to give the stability corrected form of the log-law

$$\langle u \rangle = \frac{u_*}{\kappa}\left[\ln\left(\frac{z}{z_{0m}}\right) - \psi_m(\zeta, \zeta_{0m})\right] \tag{2.8}$$

$$\langle \theta \rangle - \theta_s = \frac{\theta_*}{\kappa}\left[\ln\left(\frac{z}{z_{0h}}\right) - \psi_h(\zeta, \zeta_{0h})\right] \tag{2.9}$$

where U and θ are the mean wind wind speed and potential temperature at the first model level, θ_s is the potential temperature at the roughness height z_0, and ψ_m and ψ_h are the integral stability correction functions defined as

$$\psi_m = \int_{\zeta_{0m}}^{\zeta} \frac{1 - \phi_m(\zeta_X)}{\zeta_X} d\zeta_X \tag{2.10}$$

$$\psi_h = \int_{\zeta_{0h}}^{\zeta} \frac{1 - \phi_h(\zeta_X)}{\zeta_X} d\zeta_X. \tag{2.11}$$

The use of dimensional analysis allowed Monin and Obukhov to simplify the problem of determining fluxes in the atmospheric surface down to four key variables: L, u_*, κz, and $\partial u/\partial z$. Despite its wide adoption in the literature, MOST suffers from well-known shortcomings due to the assumptions underlying its derivation. Some of the models discussed later are designed to alleviate these issues, namely we assume turbulence is horizontally homogeneous over a plane.

2.1.2 Empirical Businger-Dyer

The dimensionless functions $\phi_m(\zeta)$ and $\phi_h(\zeta)$ must be determined empirically from observations, in this case taken to be from Dyer and Hicks (1970), defined as

$$\phi_m = \begin{cases} 1 + 5\zeta & \zeta \geq 0 \\ (1 - 16\zeta)^{-0.25} & \zeta < 0 \end{cases} \tag{2.12}$$

$$\phi_h = \begin{cases} 1 + 5\zeta & \zeta \geq 0 \\ (1 - 16\zeta)^{-0.50} & \zeta < 0 \end{cases} \tag{2.13}$$

Using these function, also called the Businger-Dyer formulations, above Eq. 2.10 and Eq. 2.11 can be integrated to yield

$$\psi_m = \begin{cases} -5\zeta & \zeta \geq 0 \\ 2\ln\left(\frac{1+x}{2}\right) + \ln\left(\frac{1+x^2}{2}\right) - 2\arctan x + \frac{\pi}{2} & \zeta < 0, x = \left[(1-16\zeta)^{-0.25}\right]^{-1} \end{cases} \tag{2.14}$$

$$\psi_h = \begin{cases} -5\zeta & \zeta \geq 0 \\ 2\ln\left(\frac{1+x}{2}\right) & \zeta < 0, x = \left[(1-16\zeta)^{-0.50}\right]^{-1} \end{cases} \tag{2.15}$$

Combining these results with Eq. 2.8 and Eq. 2.9, the average surface fluxes of momentum and heat can be calculated as

$$\langle \tau \rangle_s = \left[\frac{\kappa U}{\ln\left(\frac{z}{z_{0m}}\right) - \psi_m(\zeta) + \psi_m(\zeta_0)} \right]^2 \tag{2.16}$$

$$\langle w'\theta' \rangle_s = -\frac{\kappa^2 U(\theta - \theta_s)}{\left[\ln\left(\frac{z}{z_{0m}}\right) - \psi_m(\zeta) + \psi_m(\zeta_0)\right]\left[\ln\left(\frac{z}{z_{0h}}\right) - \psi_h(\zeta) + \psi_h(\zeta_{0h})\right]}. \tag{2.17}$$

Here U is the wind speed at the first grid point above the surface, θ the potential temperature at the first grid point above the surface, θ_s the surface potential temperature, z is the height of the first grid point, z_{0m} and z_{0h} are the surface roughness values for heat and momentum, and ζ, ζ_0, and ζ_{0h} are the dimensionless variable z/L evaluated at z and z_0.

2.1.3 Tile Model (TM)

As stated in the previous section, MOST relies upon four key assumptions: stationary flow, high Reynolds number flow, the flow is horizontally homogeneous, and flow restricted to the surface layer. While most of these assumptions are frequently valid in the atmospheric surface layer, the horizontally homogeneity assumption is not often satisfied. This is an issue since land heterogeneity is ubiquitous to the earth.

While different approaches have been taken incorporating land-surface heterogeneity into surface flux models, one of the popular methods is the Tile Model (TM) (Avissar and Pielke, 1989). In the TM scheme, the interactions between each surface type (or patch) with the atmosphere are modeled separately, and then the fluxes from each patch are added to get the total flux into the ABL. Mathematically the average surface fluxes take the form

$$\langle \tau_s \rangle = -\sum_i^n f_i \left[\frac{\langle M(Z_m) \rangle \kappa}{\ln\left(Z_m/z_{o,i}\right) - \Psi_m(Z_m/L_i)} \right]^2 \tag{2.18}$$

$$\langle q_s \rangle = -\sum_i^n f_i \frac{\kappa^2 \langle M(Z_m) \rangle [\langle \theta(Z_m) \rangle - \theta_{s,i}]}{[\ln\left(Z_m/z_{0,i}\right) - \Psi_m(Z_m/L_i)][\alpha \ln\left(Z_m/z_{0h,i}\right) - \Psi_h(Z_m/L_i)]} \tag{2.19}$$

Here $M(Z_m)$ represents the wind speed at the first grid point above ground Z_m, $z_{o,i}$ is the roughness length over each tile, Ψ_m and Ψ_h are the stability correction terms, L_i is the Obukhov length over each patch, and α is a constant. The Obukhov length as before is defined as

$$L = -\frac{\theta_0 {u_*}^3}{\kappa g \langle w'\theta' \rangle_s} \tag{2.20}$$

which is composed of the mean horizontally averaged surface flux and the surface friction velocity. It is important to note this as the order of averaging is important as

the Obukhov length of the mean fluxes does not equal the mean Obukhov length of the patches, or

$$L \neq \langle L_i \rangle. \tag{2.21}$$

2.1.4 Modified Tile Model (MTM)

While the TM scheme seems to work well to correct problem with the bulk parameterization method from MOST, it is not perfect. Stoll and Porté-Agel (2009) found that using the TM with no feedback between the surface fluxes and atmospheric variables, the wrong sign can be predicted for the surface heat fluxes. This was due to poor estimation of the stable patches surface heat flux. To address this issue, Stoll and Porté-Agel (2009) combined local scaling ideas from Nieuwstadt (1984) and the TM and blending height concepts to improve the heat flux estimations over the stable patch.

Using these ideas, the new integral stability functions that account for advection over the stable patches are

$$\Psi_m(\zeta) = -A\zeta - \beta_M \left[\frac{B-A}{A^2(A\zeta+1)} - \frac{B-A}{A^2} + \frac{B}{A^2} \ln\left(A\zeta+1\right) \right] \tag{2.22}$$

.

$$\Psi_h(\zeta) = \alpha \frac{B-A}{B} \ln\left(A\zeta+1\right) + \beta_H \left[\frac{(3B^2\zeta^2 + 3B\zeta + 1)A^2 + (3B\zeta+1)BA + B^2}{3A^3(A\zeta+1)^3} - \frac{A^2 + BA + B^2}{3A^3} \right] \tag{2.23}$$

where A and B are defined as

$$A = \left(\frac{u_{*,b}}{u_{*,i}} - 1 \right) \frac{L_i}{l_b} \quad \text{and} \quad B = \left(\frac{q_b}{q_{s,i}} - 1 \right) \frac{L_i}{l_b}. \tag{2.24}$$

Here $u_{*,b}$ is the friction velocity at the blending height l_b, $u_{*,i}$ is the friction velocity at the surface for a given patch, q_b is the heat flux at the blending height, and $q_{s,i}$ is the surface heat flux for a given patch.

To implement the new model, the blending height must first be calculated. The blending height is the height at which the impact from fluxes originating at the individual patches is considered homogeneous (Mason, 1988). The blending height can be found by balancing terms in the momentum equation and is expressed as

$$l_b \left[\ln \left(\frac{l_b}{z_{o,e}} \right) \right]^2 = 2\kappa^2 L_c \tag{2.25}$$

where L_c is the scale of horizontal variation based on the surface heterogeneity and $z_{o,e}$ is an effective roughness length. With only temperature heterogeneity, $z_{0e} = z_0$, and Eq. 2.25 can be solved using a number of different methods.

The temperature and wind speed must be extrapolated from the first model grid level to the blending height since it can often be lower than the lowest model grid point. This is accomplished using MOST for the grid-averaged flow as

$$\frac{\langle M(Z_m) \rangle}{\langle M(l_b) \rangle} = \frac{\ln \left(Z_m / z_{o,e} \right) - \Psi_m (Z_m / L_{eff})}{\ln \left(l_b / z_{o,e} \right) - \Psi_m (l_b / L_{eff})}, \text{ and} \tag{2.26}$$

$$\frac{\langle \theta(Z_m) - \theta_{s,i} \rangle}{\langle \theta(l_b) - \theta_{s,i} \rangle} = \frac{\alpha \ln \left(Z_m / z_{t,e} \right) - \Psi_h (Z_m / L_{eff})}{\alpha \ln \left(l_b / z_{t,e} \right) - \Psi_h (l_b / L_{eff})}. \tag{2.27}$$

In the above, α is a constant, $\theta_{s,i}$ is the surface potential temperature over each patch, L_{eff} is an effective Obukhov length, and $z_{t,e}$ is the effective roughness length for heat. Here the stability functions are defined based on local scaling

$$\Psi_m = \frac{z}{H} + \beta_M \frac{H}{L} \ln \left(\frac{H - z}{H} \right) \tag{2.28}$$

$$\Psi_h = -\beta_H \frac{z}{H} \frac{H}{H-z} \tag{2.29}$$

where H is the boundary layer height and β is a constant. While the MTM is much more complicated in the underlying equations, it does make improvements notable improvements to the TM by improving the heat flux from the colder patch. Results from Stoll and Porté-Agel (2009) indicated better agreement in the surface fluxes of heat and momentum when comparing to offline LES results.

2.1.5 Surface Roughness Model (RM)

While the TM and MTM account for surface temperature heterogeneity, the following model accounts for surface roughness heterogeneity. This is done using an approach where the surface roughness from each patch is added to get an effective surface roughness value (Miller and Stoll, 2013). This surface roughness value is then used in the calculations following classic MOST with the Businger-Dyer functions.

While it seems trivial to calculate the effective surface roughness value, is not the case. Unlike the surface temperature differences that add linearly, surface roughness values do not which makes determining effective roughness challenging. The effective surface roughness values are then instead tied to the blending height described earlier in the previous section, and the scale of horizontal variability, L_c. Mason (1988) expressed the effective roughness as the harmonic average of the square of the natural log of the ratio between l_b and $z_{o,i}$, or expressed mathematically

$$\frac{1}{\left[\ln\left(\frac{l_b}{z_{o,e}}\right)\right]^2} = \frac{f_1}{\left[\ln\left(\frac{l_b}{z_{o,1}}\right)\right]^2} + \frac{f_2}{\left[\ln\left(\frac{l_b}{z_{o,2}}\right)\right]^2} \tag{2.30}$$

To compute the fluxes, the blending height in Eq. 2.25 is first calculated using an estimated z_{0e}, such as the average of the z_0 values. Using this l_b value, the effective

roughness z_{0e} can then be calculated using Eq. 2.30. This new z_{0e} is used again in Eq. 2.25, and the loop continues until a value converges for z_{0e}.

2.2 Planetary Boundary Layer (PBL) Schemes

The PBL scheme determines the subgrid scale fluxes that are transported by eddies in the vertical direction. Here the PBL scheme plays an important role in quantifying the amount of vertical diffusion happening in the processes. As there is only one direction in the single column model, no special treatments have to be made for the horizontal diffusion. A lower boundary condition is needed to drive the PBL scheme, which can be computed through MOST or a LSM. The PBL model then can compute time tendencies of temperature, moisture, and momentum for the entire vertical profile.

Many different types of PBL closure have been proposed. These include the K-profile closure technique, the K-ϵ model, and the Mellor-Yamada closure. The K profile technique models the fluxes based on integral profiles for the entire PBL using the boundary layer height and the surface fluxes as scaling parameters. The weaknesses here is that all of these models are local in nature, meaning that the second-order moments are only related to local gradients at one point. In this sense turbulence does not feel any effects from large scale motions of the boundary layer.

The turbulence parameterizations can be broken up into different categories based upon the order of moment that is used in parameterizing unknown terms. One of the more popular ways this is done is using the Mellor and Yamada (1982) hierarchy, where closure equations were derived for both first-, second-, and third-order moments. Second- and third-order moment closure is almost exclusively used for research purposes as the computational resources increase with increasing complexity. Theoretically this can be extended to n^{th} order, but the number of terms that need to be modeled increases

with order and the interpretation of the newly derived terms becomes difficult, making choices for parameterization not always clear. In between first- and second-order closure lies 1.5-order, where the turbulence kinetic energy (TKE) is used in place of the vertical velocity variance. Here, both first-order and 1.5-order schemes used in the SCM are described thoroughly.

2.2.1 First-Order Schemes

The first-order schemes are those in which first order moments are retained, and all higher order moments are modelled. The first order models are the simplest to implement as only two equations need to be parameterized for the turbulent fluxes of momentum and heat. One of the more common ways this is done is with an eddy diffusivity type model which relates the turbulent fluxes to a constant and the vertical gradients of either heat or momentum.

2.2.1.1 ECMWF

The ECMWF model uses the K-type closure where the fluxes are assumed to be proportional to gradients of potential temperature and wind speed (Louis et al., 1982; Beljaars, 2002). It is similar to the other models by closing the equations using K-theory and and uses Prandtl's mixing length hypothesis to define a mixing length l_m (Prandtl 1925). Here the idea is to use the fact that Ri, the Richardson number, can be related to surface layer quantities including the Obukhov length (L) as

$$Ri = \frac{g}{\theta_0} \frac{\partial\theta/\partial z}{(\frac{\partial u}{\partial z})^2 + (\frac{\partial v}{\partial z})^2} = \frac{l_m}{\kappa L} \frac{\phi_h}{\phi_m^2} \tag{2.31}$$

where θ is the potential temperature, θ_0 is a reference potential temperature, g is gravity, z is the height, u and v are the streamwise and spanwise velocity components,

$\kappa = 0.4$ is the von Kármán constant, and l is the mixing length. Using ideas from surface layer similarity theory, stability functions are then defined in terms of the Richardson number

$$\phi_m = \left(1 + \frac{10Ri}{\sqrt{1+5Ri}}\right)^{-1} \tag{2.32}$$

$$\phi_h = \left(1 + 15Ri\sqrt{1+5Ri}\right)^{-1} \tag{2.33}$$

Since the gradient Richardson number can be used as an alternative to ζ and involves gradients of buoyancy and velocity, it can be easily calculated for most stable boundary layers. In the SCM, the Richardson number is bounded by ($0 < Ri < 10^{12}$), limiting Ri to stable conditions and removing the the possible for large spurious values.

The turbulence length scale l is computed as

$$l = \frac{l_0 \kappa z}{l_0 + \kappa z} \tag{2.34}$$

where κ is the von Kármán constant and $l_0 = 150\,\mathrm{m}$ is an asymptotic length scale. This is based upon the typical scaling law $l = \kappa z$ in the surface layer, but with a correction applied to limit the length scale l for large values of z. Using this length scale, the eddy diffusivities are written as functions of l, the stability functions ϕ_m and ϕ_h, and the velocity gradient $\partial U/\partial t$

$$K_m = l^2 \phi_m \left|\frac{\partial U}{\partial z}\right| \tag{2.35}$$

$$K_h = K_m \frac{\phi_h}{\phi_m}. \tag{2.36}$$

When applying the ECMWF model, the gradients of heat and momentum are first calculated to evaluate the Richardson number (left side of Eq. 2.31). The turbulence length scale is then calculated using Eq. 2.34. The stability functions (Eq. 2.32 and

2.33) are calculated using the Richardson number, and then the eddy diffusivities (Eq. 2.5 and 2.6) are updated using l, ϕ_m, and ϕ_h.

While the ECMWF model is not complex and makes fairly reasonable approximations, there are many issues that arise with the simplistic approach here. First, it is known that in reality there are more variables that should be considered including higher-order moments of temperature and momentum, as well as an inclusion of the TKE.

2.2.2 1.5-Order Schemes

Beyond first-order closure is second-order where the second order moments are predicted and all high order moments moments are parameterized. This increases the degree of difficulty to the problem by increasing the total number of terms needed to derive closure equations. Some turbulence schemes achieve a halfway point between first and second-order closure named 1.5-order. These schemes are more advanced than first-order and use TKE as an additional prognostic equation to be solved. The TKE is defined as

$$e = \frac{1}{2}\left(\langle u'^2\rangle + \langle v'^2\rangle + \langle w'^2\rangle\right) \tag{2.37}$$

where e is TKE, and $\langle u'^2\rangle$, $\langle v'^2\rangle$, $\langle w'^2\rangle$ are the plane mean values of the variances of u, v, and w. The TKE can can be thought of as a measure of the turbulence intensity Stull (1988). The idea is that 1.5-order is an improvement over first-order closure by solving an additional prognostic equation for TKE, which is a second order moment. The time tendency of TKE is then solved using parameterized terms in the TKE budget equation.

The most important equation for 1.5-order schemes is the prognostic TKE equation parameterized for the boundary layer following Mellor and Yamada (1982) MY82 as

$$\frac{\partial(q^2/2)}{\partial t} = \frac{\partial}{\partial z}\left(lqS_q\frac{\partial(q^2/2)}{\partial z}\right) + P_s + P_b - \epsilon. \tag{2.38}$$

Here the TKE is defined to be TKE $= q^2/2$, l is the turbulence length scale, S_q is a constant stability function for q set equal to 0.2, P_s and P_b are the shear and buoyancy production terms of TKE, and ϵ is the dissipation of TKE. The shear and buoyancy production terms are defined as

$$P_s = -\langle w'u'\rangle\frac{\partial\langle u\rangle}{\partial z} - \langle w'v'\rangle\frac{\partial\langle v\rangle}{\partial z} \tag{2.39}$$

$$P_b = \beta g\langle w'\theta'\rangle \tag{2.40}$$

and the dissipation term is parameterized using dimensional analysis as

$$\epsilon = \frac{q^3}{B_1 l} \tag{2.41}$$

where B_1 is a constant and $\beta = \frac{g}{\theta_0}$.

In the MY82 scheme, the turbulent fluxes are related through an eddy diffusivity defined as

$$\langle u'w'\rangle = -K_m\frac{\partial\langle u\rangle}{dz} \tag{2.42}$$

$$\langle v'w'\rangle = -K_m\frac{\partial\langle v\rangle}{dz} \tag{2.43}$$

$$\langle w'\theta'\rangle = -K_h\frac{\partial\langle\theta\rangle}{dz} \tag{2.44}$$

$$K_M = lqS_M \tag{2.45}$$

$$K_H = lqS_H \tag{2.46}$$

where S_M and S_H are stability functions. The stability functions are then defined to be functions of buoyancy and shear and written as

$$S_M(6A_1A_2G_M) + S_H(1 - 3A_2B_2G_H - 12A_1A_2G_H) = A_2 \tag{2.47}$$

$$S_M(1 + 6A_1^2G_M - 9A_1A_2G_H) - S_H(12A_1^2G_H + 9A_1A_2G_H) = A_1(1 - 3C_1) \tag{2.48}$$

where A_1, A_2, B_1, B_2, C_1 are all empirically derived constants and G_M and G_H are

$$G_M = \frac{l^2}{q^2}\left[\left(\frac{\partial u}{\partial z}\right)^2 + \left(\frac{\partial v}{\partial z}\right)^2\right] \tag{2.49}$$

$$G_H = -\frac{l^2}{q^2}\beta g\frac{\partial \theta}{\partial z}. \tag{2.50}$$

The MY82 is a popular scheme, and is included in WRF in MYNN and MYJ. At the core these two schemes are based upon MY82 due to its relative simplicity, but aim to improve on known issues.

2.2.2.1 Mellor-Yamada Janjic (MYJ)

Janjic (2002) aimed to improve upon the MY82 scheme by taking into account that the TKE can have singular solutions in the parameterization of the TKE production. The contributions from production and dissipation in the TKE equation from MY82 can be written in the form:

$$l\frac{d\left(\frac{1}{q}\right)}{dt} = -\frac{A\left(\frac{l}{q}\right)^4 + B\left(\frac{l}{q}\right)^2}{C\left(\frac{l}{q}\right)^4 + D\left(\frac{l}{q}\right)^2 + 1} + \frac{1}{B_1} \tag{2.51}$$

where l is the turbulence length scale, and B_1 is a constant. The other coefficients A, B, C, and D are all constants based upon shear, buoyancy and other model constants

A_1, A_2, B_1, B_2, C_1. Singularities can arise in Eq. 2.51 depending on the ratio of l/q. In the unstable case for growing turbulence, the denominator of Eq. 2.51 can go to zero and is given by

$$C\left(\frac{l}{q}\right)^4 + D\left(\frac{l}{q}\right)^2 + 1 = 0. \tag{2.52}$$

This polynomial can be solved to yield a constraint on l for convective conditions as

$$l < q\sqrt{\frac{1}{p_1}} \tag{2.53}$$

where p_1 is the root from Eq. 2.52.

In the stable regime there are no singular points, but the behavior of $\overline{w'w'}/q^2$ is investigated to find the limit of $\overline{w'w'}/q^2$ for the case of vanishing turbulence,

$$R_s = \frac{\overline{w'w'}}{q^2} = \frac{1}{3} - 2A_1 S_M G_M + 4A_1 S_H G_H. \tag{2.54}$$

Simplifying and rearranging Eq. 2.54 yields another polynomial that can be solved,

$$I\left(\frac{q}{l}\right)^4 + H\left(\frac{q}{l}\right)^2 + G = 0. \tag{2.55}$$

Here again I, H, and G are all functions of buoyancy and solving Eq. 2.55 yields another constraint on the turbulence length scale

$$l < q\sqrt{\frac{1}{t_1}} \tag{2.56}$$

where t_1 is the root of Eq. 2.55. Based on these two constraints, a unified condition can be developed where

$$0 < l < aq, \qquad a = \sqrt{\frac{1}{p_1}} \tag{2.57}$$

and

$$0 < l < bq, \qquad b = \sqrt{\frac{1}{t_1}}. \tag{2.58}$$

Note that here, this is an "and" statement, meaning that both conditions in Eq. 2.57 and Eq. 2.58 must be satisfied simultaneously.

The turbulence length scale is first computed following the MY82 diagnostic form

$$l = l_0 \frac{\kappa z}{\kappa z + l_0}, \quad l_0 = \alpha \frac{\int zqdz}{\int qdz} \tag{2.59}$$

where $\alpha = 0.25$ is an empirical constant, before adjustments are made to satisfy the conditions in Eq. 2.57. The behavior of Eq. 2.59 is that l will tend towards κz for small z, but approach l_0 for large z. The boundary layer height is defined as the lowest model level at which the equilibrium turbulence energy becomes negative, or in other word the height of the lowest model level at which TKE approaches its prescribed lower bound. Outside of the boundary layer the length scale follows Mason (1989)

$$l = \kappa \Delta z \tag{2.60}$$

where Δz is the vertical grid spacing of the model.

The production and dissipation terms of the TKE equation are considered separately as they are the dominant terms in the TKE equation (2.38). To determine these contributions alone, the focus will be on solving Eq. 2.51 where the TKE equations are written in terms of only production and dissipation. The idea proposed is to linearize Eq. 2.51 and use an iterative procedure to solve for q. The solution is then

$$\left(\frac{l}{q}\right)_{i+1} = \left(\frac{l}{q}\right)_i - \frac{R\left(l/q\right)_i}{R'\left(l/q\right)_i} + \left[\frac{R\left(l/q\right)_i}{R'\left(l/q\right)_i} + \left(l/q\right)_0 - \left(l/q\right)_i)\right] \exp\left[\Delta t R'\left(l/q\right)_i\right] \tag{2.61}$$

where $(l/q)_0$ is the initial value of (l/q) at the beginning of time step Δt, R is the right hand side of Eq. 2.51, and R' is the derivative of R. The time to reach convergence is not long and is typically in two iterations.

The MYJ scheme first computes the turbulence length scale based on Eq. 2.59 and 2.60. Adjustments are then made based on the non-singular constraints defined in Eq. 2.57. Then the contributions from production and dissipation are added to the TKE. The diffusion coefficients are then updated without the re-computation of the turbulence length scale l. The vertical diffusion of TKE is computed after the computation of the turbulence exchange coefficients. Due to the linearization of Eq. 2.61 and the iterative process used, virtually the same parameters determine the TKE production/dissipation and vertical diffusion of the large-scale variables.

2.2.2.2 Mellor-Yamada Nakanishi-Niino (MYNN)

The Mellor-Yamada Nakanishi-Niino (MYNN) scheme improves upon the MY82 scheme by including the effects of stability on the turbulent length scale and buoyancy effects on the pressure covariance (Nakanishi (2001); Nakanishi and Niino (2004, 2006, 2009). In addition, the model constants from MY82 were reevaluated and tuned from a LES database based upon one-dimensional simulations from day 33 of the Wangara field experiment in southeastern Australia in 1967 (Clarke et al., 1971). From the Wangara experiment the MYNN scheme improved upon a few weak points of the MY82 model, including insufficient growth of the convective boundary layer, and the underestimation of TKE and the turbulence length scale. The main improvements of MYNN are due to the new formulation of the turbulence length scale that increases with decreasing stability.

The turbulence length scale l needs to be reliably determined for different conditions of stratification and buoyancy. The original MY82 scheme proposed a constant l only

based on the boundary layer height as defined in Eq. 2.59. Here MYNN proposes a new formulation for the turbulence length scale based upon three respective scales: l_s, l_b, and l_t. MYNN takes a harmonic average of the three length scales in order to limit the turbulence length scale to the smallest of the three scales.

$$\frac{1}{l} = \frac{1}{l_s} + \frac{1}{l_b} + \frac{1}{l_t}. \tag{2.62}$$

Here, l_s is a length scale meant to capture surface effects through MOST, the turbulent length scale l_t is the length scale dependent upon the depth of the ABL, and the buoyancy length scale l_b is related to the quantity q/N which relates TKE to buoyancy from the background stratification.

The prior formulations for the length scale in the surface layer from MY82 have assumed the length scale should follow κz, but observations have shown stability influences the length scale. To determine the length scale based on stability, the TKE in the surface layer is assumed to be in local equilibrium, and based on data from LES the length scale in the surface layer takes the form

$$l_s = \begin{cases} \kappa z(1 + 2.7\zeta)^{-1} & \zeta > 0 \\ \kappa z(1 - 100\zeta)^{0.2} & \zeta \leq 0. \end{cases} \tag{2.63}$$

The buoyancy length scale l_b is defined as

$$l_b = \begin{cases} q/N & \partial\theta/\partial z > 0, \quad \zeta \geq 0 \\ \left[1 + 5\left(q_c/L_T N\right)^{1/2}\right] q/N & \partial\theta/\partial z > 0, \quad \zeta < 0 \\ \infty & \partial\theta/\partial z \leq 0 \end{cases} \tag{2.64}$$

where $N = [(g/\theta_0)\partial\theta/\partial z]^{1/2}$ is the Brunt-Vaisala frequency and $q_c = [(g/\theta_0)\langle w\theta\rangle_0 L_T]^{1/3}$ is a velocity scale similar to that of w_*, the Deardorff scale (Deardorff, 1970), defined as

$$w_* = \left(\frac{g}{\theta} z_i \langle w\theta\rangle_0\right)^{1/3}. \tag{2.65}$$

Here z_i represents the height of the convective mixed layer. The buoyancy length scale l_b characterizes the distance an air parcel having TKE of $q^2/2$ can move vertically against the buoyancy force. The behavior of q/N for l_b will tend to underestimate the length scale in the upper part of the convective PBL due to buoyancy production and turbulent transport of TKE.

The length scale l_t is the length scale based upon the boundary layer height. It uses similar looking formulation to that of MY82, but instead follows the length scale definition from Mellor and Yamada (1974) where l_t is defined as

$$l_t = \alpha \frac{\int zqdz}{\int qdz} \tag{2.66}$$

with $\alpha = 0.23$. As this value is based on the boundary layer height, it has the greatest contribution to to the turbulence length scale l in the middle to upper portions of the boundary layer.

The MYNN model has the the option to use a first-, 1.5-, or second-order model. In the first order model (level 2 model) the time tendency, advection, and diffusion terms of the TKE equation are neglected. This allows for the TKE to be calculated diagnostically as

$$q_2^2 = B_1 l^2 S_{M2}(1 - Rf)\left[\left(\frac{\partial u}{\partial z}\right)^2 + \left(\frac{\partial v}{\partial z}\right)^2\right] \tag{2.67}$$

where B_1 is a constant, l is the turbulence length scale, S_{M2} is a level 2 stability function, and Rf is the flux Richardson number. The 1.5-order (level 2.5) model does not simplify to as much of a degree, retaining a prognostic TKE equation. In the second order (level 3) model, the variance of potential temperature, and covariance of potential temperature and specific humidity are included as prognostic equations to be predicted.

The stability functions used in the level 3 model is split into a level 2.5 term and a correction term, namely,

$$S_M = S_{M2.5} + S'_M \tag{2.68}$$

$$S_H = S_{H2.5} + S'_H \tag{2.69}$$

where $S_{M2.5}$, $S_{H2.5}$ are the level 2.5 stability functions and S'_M, S'_M is the difference between the level 3 and level 2.5 stability functions. Each stability functions are defined as

$$S_M = \alpha_c A_1 \frac{\Phi_3 - 3C_1\Phi_4}{D_{2.5}} \tag{2.70}$$

$$S_H = \alpha_c A_2 \frac{\Phi_2 + 3C_1\Phi_5}{D_{2.5}} \tag{2.71}$$

and

$$S'_M = \alpha_c A_1 \frac{\Phi_3 - \Phi_4}{D'}\Phi' \tag{2.72}$$

$$S'_H = \alpha_c A_2 \frac{\Phi_2 + \Phi_5}{D'}\Phi'. \tag{2.73}$$

A_1, A_2, and C_1 are model constants, $D_{2.5}, D'$ and the Φ terms are constants based on buoyancy and wind shear and α_c is defined as

$$\alpha_c = \begin{cases} q/q_2, & q < q_2 \\ 1, & q \geq q_2. \end{cases} \tag{2.74}$$

In the 1.5 closure, the correction terms S'_M and S'_H are considered zero and the only contribution arise from the level 2.5 scheme, $S_{M2.5}$ and $S_{H2.5}$. The stability functions are then related to the eddy diffusivity as before from MY82

$$K_m = lqS_m \tag{2.75}$$

$$K_h = lqS_h. \tag{2.76}$$

For MYNN, the vertical diffusion of TKE is carried out along with the calculation of production and dissipation. For the vertical diffusion term, the stability function for TKE S_q is set to be a multiple of the stability function for momentum, $S_q = 3S_M$.

The scheme is implemented by first calculating closure constants and stability functions for the level 2 implementation of the model that neglects the time tendency, advection, and diffusion of TKE. The turbulence length scale is then determined from the surface, buoyancy, and boundary layer length scales. The level 2.5 stability functions are then calculated along with the eddy diffusivities and the production and dissipation terms of TKE. Finally, the vertical diffusion of TKE is carried out and the time tendencies of temperature and momentum for the entire vertical profile are updated.

Chapter 3

Model Setup

3.1 Single Column Model

As noted in the introduction, the SCM uses a set of simplified equations for the boundary layer. As this thesis is interested in the impacts of the turbulence schemes, there is no radiation scheme or land-surface model available in the SCM. The three core equations to be solved are then

$$\frac{\partial\langle u\rangle}{\partial t} = f(\langle v\rangle - V_g) - \frac{\partial\langle u'w'\rangle}{\partial z} + F_{nudge} \tag{3.1}$$

$$\frac{\partial\langle v\rangle}{\partial t} = -f(\langle u\rangle - U_g) - \frac{\partial\langle v'w'\rangle}{\partial z} + F_{nudge} \tag{3.2}$$

$$\frac{\partial\langle \theta\rangle}{\partial t} = -\frac{\partial\langle w'\theta'\rangle}{\partial z} + F_{nudge} + F_{LS} \tag{3.3}$$

In the equations above $\langle u\rangle$ and $\langle v\rangle$ are the mean streamwise and spanwise velocities respectively, $\langle\theta\rangle$ is the mean potential temperature, U_g and V_g are the streamwise and spanwise geostrophic wind values, F is a forcing term, $\langle u'w'\rangle$ and $\langle v'w'\rangle$ are the kinematic turbulent fluxes for momentum in each component direction, and $\langle w'\theta'\rangle$ is the vertical heat flux. Eq 3.1, 3.2, and 3.3 make up a system of 3 equations and three unknowns u, v, and θ making it fully deterministic when suitable closure schemes are selected for $\langle u'w'\rangle$, $\langle v'w'\rangle$, and $\langle w'\theta'\rangle$. As described in the previous chapter $\langle u'w'\rangle$, $\langle v'w'\rangle$ and $\langle w'\theta'\rangle$ are parameterized and determined by the chosen PBL scheme.

To force the SCM, different values of U_g and V_g are set in the namelist values as constant in time and height. The SCM has the ability to add in the effects of large-scale forcing through the term F_{LS} defined as

$$F_{LS} = w\frac{\partial\theta}{\partial z} \tag{3.4}$$

where w is the vertical velocity component. This large scale forcing term is only applied to Eq. 3.3.

Another option available to force the simulation is a nudging term. This nudging term is based upon observations of vertical profiles of u, v, and θ. These observations can be from real data including Doppler LIDAR and atmospheric emitted radiance interferometer (AERI) profiles, or vertical profiles from high-resolution mesoscale model output. The method is employed to nudge the model to realistic atmospheric solutions in order to keep the simulation from diverging towards unrealistic solutions. The difference between the observations and model output are calculated at each time step in the simulation and divided by a relaxation time scale set to $\alpha = 10\,800\,\mathrm{s} = 3\,\mathrm{h}$, as seen in Eq. 3.5

$$F_{nudge} = \frac{X_{SCM} - X_{Ob}}{\alpha}, \tag{3.5}$$

where X_{SCM} is the variable of interest (u, v, or θ) from the simulation, and X_{Ob} is the observation at the same time. This value of α was chosen based upon how strongly the simulation reacted to the forcing. A smaller values of $\alpha = 3600\,\mathrm{s} = 1\,\mathrm{h}$ was tested and resulted in an over-forcing of the the model simulation, leading the simulation variables to be equal to the observations. Larger values were tested and a value of $\alpha = 10\,800\,\mathrm{s} = 3\,\mathrm{h}$ was found to have a balance between the model simulation and forcing. A more rigorous formulation for α can be implemented in the future.

The two additional forcing terms, F_{LS} and F_{nudge} are terms that are added to the right hand side of Eq. 3.1 – 3.3, represented as generically as F. The nudging force can be applied to each field, but based on how the large scale forcing term F_{LS} is defined, F_{LS} is only added to Eq. 3.3.

3.2 Numerical Implementation of SCM

3.2.1 Computational Grid

The vertical grid uses a staggered approach where the grid is split into full levels and half levels. The u, v, and θ variables are placed at the half levels ($z_h = \frac{1}{2}\Delta z, \frac{3}{2}\Delta z$,...), while the eddy diffusivity, turbulence kinetic energy, momentum and heat fluxes are defined on the full levels ($z_f = \Delta z, 2\Delta z$,...). Gradients of u, v, and θ on the full levels can be calculated as

$$\left(\frac{\partial C}{\partial z}\right)_N = \frac{C_{N+\frac{1}{2}} - C_{N-\frac{1}{2}}}{z_{N+\frac{1}{2}} - z_{N-\frac{1}{2}}}. \tag{3.6}$$

Placing the variables this way allows for easy calculation of the gradients of u, v, and θ, which are then used in the calculation of the turbulent fluxes. A schematic of the vertical grid and the variables are shown below in Figure 3.1. The bottom boundary condition is set to be no-slip, so $u = v = 0$ at the roughness height z_{0m}, along with a prescribed surface temperature at the roughness height for heat z_{0h}. The SCM has the option to choose z_{0m} to be different than z_{0h}. The top off the domain uses Neumann boundary conditions, or equivalently

$$\frac{\partial u}{\partial z} = \frac{\partial v}{\partial z} = 0, \quad \frac{\partial \theta}{\partial z} = C \tag{3.7}$$

where C is a constant equal to the specified lapse rate.

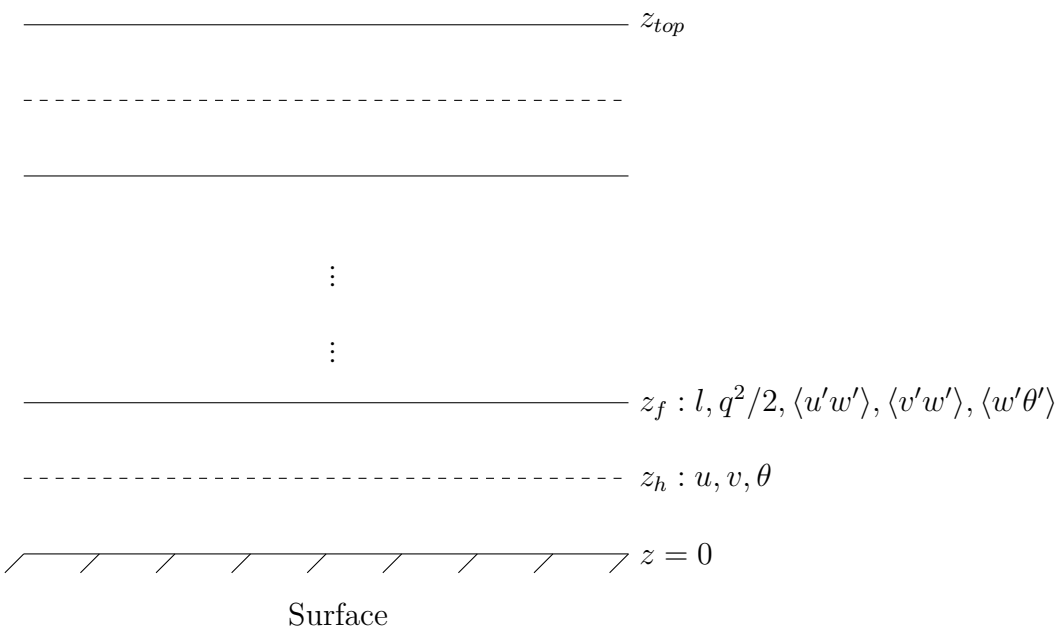

Figure 3.1: Schematic of the numerical grid used in the SCM as well as where certain variables are located.

3.3 Numerical Schemes

The gradients are calculated using second-order centered finite differences, while the time integration is done using a low-storage, third-order Runge-Kutta scheme. In the case of the 1.5-order models, the TKE equation is solved using a fully implicit Crank-Nicholson scheme.

3.3.1 Runge-Kutta III

The third-order Runge-Kutta time integration is carried out following Williamson (1980). For an ordinary differential equation of the form

$$\frac{dx}{dt} = f(x) \tag{3.8}$$

the solution using third order Runge-Kutta follows as

$$q_j = a_j q_{j-1} + h f(x_{j-1}) \tag{3.9}$$

$$x_j = x_{j-1} + b_j q_j \tag{3.10}$$

$$j = 1, 2, 3 \tag{3.11}$$

with coefficients $a_j = [0, -5/9, -153/128]$, $b_j = [1/3, 15/16, 8/15]$, and h the desired time step. This is a three sub-time process where the tendencies are calculated through Eq. 3.8, and the field of u, v, and θ are updated in Eq. 3.9.

3.3.2 Crank–Nicolson

The TKE equation is not a simple ODE that can be solved readily with the Runge-Kutta method. The two schemes implemented have different methods of solving the TKE equation, but both rely on the Crank–Nicolson method for time advancement. In the MYNN scheme, the contributions due to production and dissipation are retained in the equation. Using definitions from MY82, the TKE equation can be written as

$$\frac{\partial q^2}{\partial t} = \frac{\partial}{\partial z}\left(K(z)\frac{\partial q^2}{\partial z}\right) + (P - \epsilon) \tag{3.12}$$

where $K(z)$, P and ϵ are defined as

$$K(z) = 3lqS_M \tag{3.13}$$

$$P = lq\left(S_M g_M + S_H g_H\right) \tag{3.14}$$

$$\epsilon = \frac{q^3}{B_1 l} \tag{3.15}$$

with g_M and g_H defined as

$$g_M = \left(\frac{\partial u}{\partial z}\right)^2 + \left(\frac{\partial v}{\partial z}\right)^2 \tag{3.16}$$

$$g_H = -\beta\frac{\partial \theta}{\partial z} \tag{3.17}$$

As described in Chapter 2, for the MYJ scheme the TKE equation is simplified to remove the contributions due to production and dissaption which are calculated together using a linearization method. This simplifies the TKE equation to

$$\frac{\partial q^2}{\partial t} = \frac{\partial}{\partial z}\left(K(z)\frac{\partial q^2}{\partial z}\right). \tag{3.18}$$

Here $K(z)$ is an eddy diffusivity defined as:

$$K(z) = 0.2lqS_M. \tag{3.19}$$

Eq. 3.18 in the MYJ scheme is now a partial differential equation in the form of a 1-D diffusion equation. To solve this 1-D diffusion equation, a variable coefficient Crank–Nicolson method is used. In the Crank-Nicolson scheme, the weighted mean of the forward and backward, centered space scheme is applied, with a weighting coefficient of $\Phi_F = 1 - \Phi_B$. With $\Phi_F = \Phi_B = 0.5$, the scheme is considered fully C-N

as both forward and backward in time scheme are used. With $\Phi_F = 1$, the scheme is considered fully implicit. Through tedious algebra Eq. 3.18 can then be written in finite difference form as

$$AQ^{n+1} = R \tag{3.20}$$

where

$$R = C_p Q_{j+1} + CQ_j + C_m Q_{j-1} \tag{3.21}$$

where A is a coefficient matrix, Q represents twice the TKE, C_p, C_m, and C are matrix coefficients. Eq. 3.21 is written as a tridiangonal matrix which is then solved by using Thomas' algorithm, an efficient method for solving tridiangonal matrices (Lee, 2011).

In the MYNN scheme a similar procedure is used, but the difference between the two is in the definition of the constant C. In Eq. 3.12 the production and dissipation terms can be written as a multiple of q^2, resulting in an additional term in the makeup of the C constant in Eq. 3.22.

$$C = 1 - C_p - C_m + C_e \tag{3.22}$$

where C_e is the additional term based upon production and dissipation of TKE.

Chapter 4

Validation of SCM against GABLS1

4.1 Introduction

The Global Energy and Water Cycle Experiment (GEWEX) Atmospheric Boundary Layer Study (GABLS) was an intercomparison study performed to simulate weakly stably stratified atmospheric boundary layers (Beare et al. 2006, Cuxart et al. 2006). A series of LES experiments was performed from 11 different research groups with varying subgrid scale models to evaluate the performance and reliability of the LES. The GABLS1 study is based upon the data from Kosović and Curry (2000), which used the Beaufort Sea Arctic Stratus Experiment (BASE) dataset to provide the initial and boundary conditions (Curry et al., 1997).

The geostrophic wind is set to $8\,\mathrm{m\,s^{-1}}$, with an initial potential temperature of 265 K from the surface to 100 m. Above 100 m a lapse rate of $0.01\,\mathrm{K\,m^{-1}}$ is imposed up to the top of the simulation domain of $z = 400\,\mathrm{m}$. The surface temperature is prescribed using a cooling rate of $0.25\,\mathrm{K\,hr^{-1}}$. For PBL schemes that use TKE as a prognostic variable, the TKE field is initialized as $0.4(1-z/250)^3\mathrm{m^2\,s^{-2}}$ below $z = 250\,\mathrm{m}$. Above $z = 250\,\mathrm{m}$, the TKE is set to the minimum value allowed for the PBL scheme, $0.01\,\mathrm{m^2\,s^{-2}}$ for the MYJ scheme and $10^{-4}\,\mathrm{m^2\,s^{-2}}$ for MYNN.

To investigate the effects of surface temperature heterogeneity, two patches of equal fractional area were used in the domain and set with different cooling rates. The fractional areas was therefore 0.5 for both patches. Here how the surface temperature

heterogeneity is spatially distributed is not accounted for, only the fractional area of each type in the domain of interest. Two temperature differences of 3K and 6K were used between the patches. To generate the temperature heterogeneity, the cooling rates between the two patches were altered for the first six hours of the simulation. At the end of six hours the difference between the two patches is the desired temperature difference. While the cooling rates are different, the average between the two patches is set to be equal to the GABLS1 cooling rate. After six hours both patches were set to the GABLS1 cooling rate to reach steady state. This method for setting the cooling rates for the patches follows a similar methodology from Stoll and Porté-Agel (2009). In the 3K case, the cooling rate for the cooler patch is set to $0.5\,\mathrm{K\,hr^{-1}}$ and $0\,\mathrm{K\,hr^{-1}}$ for the warmer patch. For the 6K difference, a cooling rate of $0.75\,\mathrm{K\,hr^{-1}}$ is set for the cooler patch and a warming rate of $-0.25\,\mathrm{K\,hr^{-1}}$ for the warmer patch. This is summarized in Table 4.1.

Surface Heterogeneity Setup					
Case	Cooling Rate Patch 1 [$\mathrm{K\,h^{-1}}$]	Cooling Rate Patch 2 [$\mathrm{K\,h^{-1}}$]	Patch 1 θ at 6 hours [K]	Patch 1 θ at 6 hours [K]	θ Difference
Homogeneous	0.25	0.25	263.5	263.5	0
3K	0.5	0	262	265	3
6K	0.75	-0.25	260.5	266.5	6

Table 4.1: Surface cooling rates for the homogeneous case, as well as for the two patches when using temperature heterogeneity of 3K and 6K.

4.2 Surface Temperature Differences

4.2.1 Time Series

Time series of the Obukhov length (L) and boundary layer height (h) are shown in Figure 4.2. The boundary layer height is determined following Kosović and Curry (2000), defined as 95% of the height where the momentum flux reaches 5% of the surface value, or $h = h_{.05}/0.95$. With the homogeneous case, the boundary layer height for the ECMWF is a significant outlier with $h = 350\,\mathrm{m}$. The spread of the GABLS1 LES (Cuxart et al. 2006) has a clustering of values between $h = 150\,\mathrm{m}$ and $h = 200\,\mathrm{m}$. The MYJ and MYNN schemes perform the best by being in and very near to the spread of the LESs from GABLS1. The MYNN scheme is the best of the three and is in the center of the spread throughout the almost the entire nine hour simulations period. The MYJ scheme is has much more variability which could be due to the time increment used. For the LES from GABLS1, the clustering of the Obukhov length is between 110 m to 160 m. The ECMWF scheme is also the largest outlier with an average L of approximately 230 m. The Obukhov length for the MYJ scheme is slightly lower with an average L of approximately 200 m. The MYNN has the lowest values of approximately 130 m which is in the center of the spread of the LES simulations.

Surface temperature heterogeneity of 3K and 6K is investigated using the TM scheme (Figure 4.1 and 4.2). In both figures, the homogeneous case is denoted by the solid lines. With the 3K case with the TM, small differences were observed in the boundary layer height for the ECMWF scheme, but there is a slight increase in the boundary layer height. The boundary layer height also increased for the MYNN and MYJ scheme, even though the MYJ boundary layer height is noisy. These values can also be seen in 4.2 which are averaged over the final hour of the simulation. More

noticeably, the Obukhov lengths in all three schemes increased indicating a trend toward more neutral conditions. This is due to the effects of the warmer, unstable patch dominating the heat fluxes.

With a 6K difference between patches (Figure 4.2), significant differences are apparent in the first six hours of the simulation. The increase in the Obukhov length in time until six hours into the simulation time is a result of how the temperature heterogeneity is defined using the TM scheme. After six hours the Obukhov length begins to decrease towards a steady state value. The final value at the end of the simulation period is approximately 50 m higher than the homogeneous case. This is similar to the MYJ scheme but a smaller difference was noted in the ECMWF scheme. Steady state conditions may not be fully achieved at nine hours, but the simulation time was not extended in order to compare with the suite of LES from GABLS1.

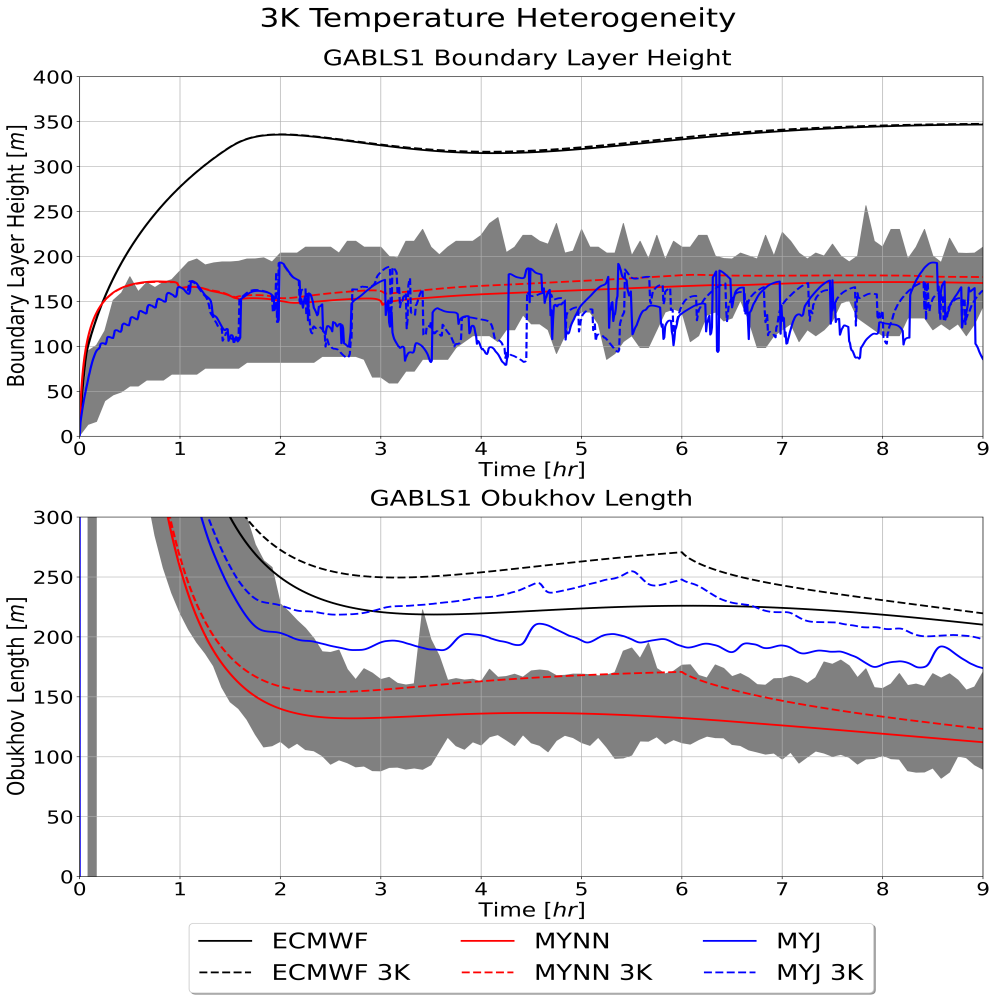

Figure 4.1: Time series of the boundary layer height (top) and Obukhov length (bottom) with the homogeneous case (solid) and surface heterogeneity with the TM with 3K patches (dashed), and the MTM with 3K patches (dotted). The ECMWF model is colored black, the MYJ blue, and the MYNN red. The shaded grey represents the spread of the LES from GABLS1.

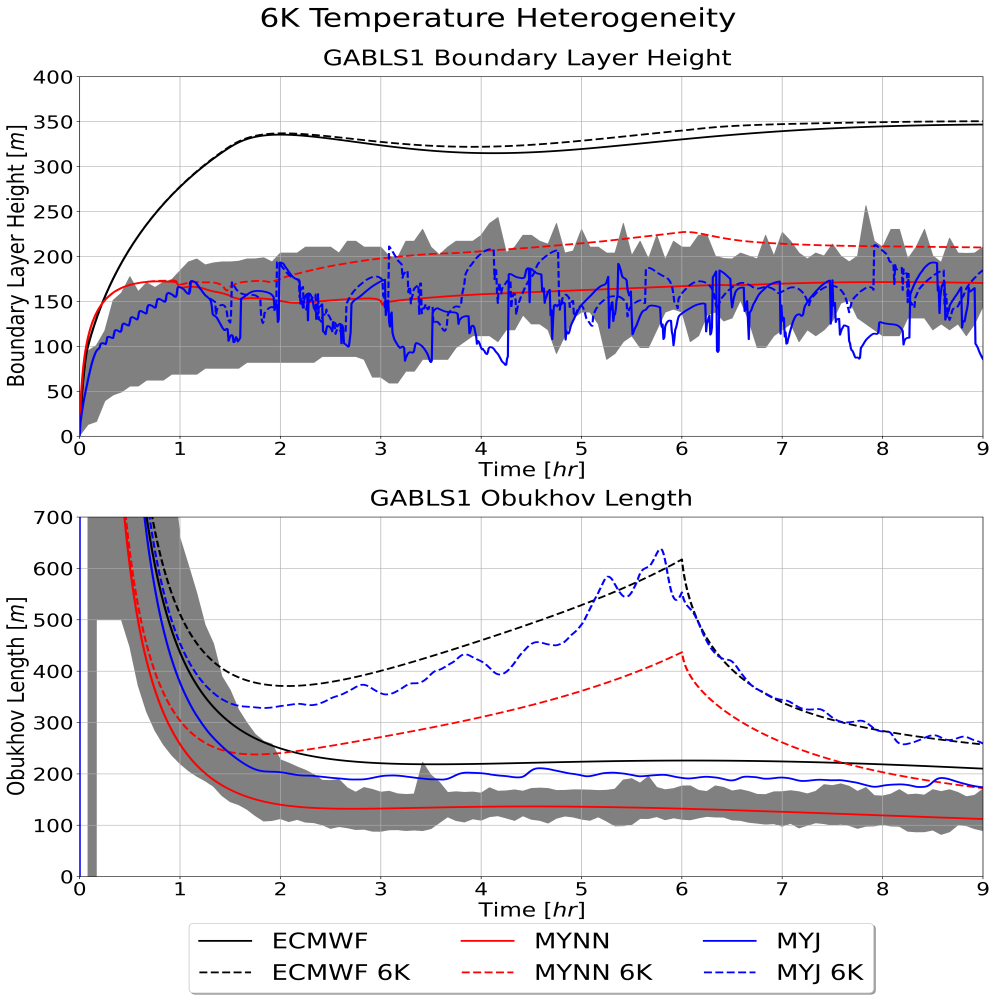

Figure 4.2: Same as previous but for 6K patches.

The friction velocity (u_*), and surface heat flux ($\langle w\theta \rangle$) in Figure 4.4 show similar behavior to the GABLS1 LES. All PBL schemes have a relative minimum approximately two hours into the simulation period, followed by a slight rise and asymptote after six hours. Similar to the time series of the Obukhov length and boundary layer height, the MYNN is in the center of the spread of the LES. The MYJ and ECMWF have slightly larger friction velocities than the MYNN and are at the upper end of the spread of the LES. The surface heat fluxes have the best agreement of all the variables investigated with each PBL scheme being in the center of the spread of the LES.

There are some notable differences in the friction velocity and surface heat flux when using the TM scheme. The surface heat flux values are lower in magnitude across each PBL scheme for both the 3K and 6K cases. In the 6K case (Figure 4.4), the surface heat flux values asymptote to values around $\langle wT \rangle \approx -0.005 K m s^{-1}$ in the first six hours of the simulation. Afterwards, the values increase until the end of the simulation period. This again is an artifact of how the surface temperature was generated over the first six hours of the simulation. The time series of friction velocity in the 3K case shows nearly indistinguishable differences between the homogeneous case. With more significant patch differences of 6K, friction velocity values were slightly larger than before, which verifies with the behavior seen with higher boundary layer heights in the heterogeneous cases.

As noted before, the time series of surface heat flux and Obukhov length have very different behavior than other variables in the first six hours of the simulation when the temperature difference between patches is set 6K. This behavior is not reflected in the time series of boundary layer height or the friction velocity due to the strong dependence the Obukhov length and surface heat fluxes have to the surface temperature. This can be seen in equations 2.1, 2.2 and 2.3 as the heat flux is defined in terms of the temperature at the surface, while the friction velocity is not. While the friction velocity calculation does involve the surface heat flux and Obukhov length in the calculations, it is indirectly affected by those terms through the stability correction. This may also explain the relatively small differences with the 3K patches, but larger differences with 6K patches in the time series of the friction velocity.

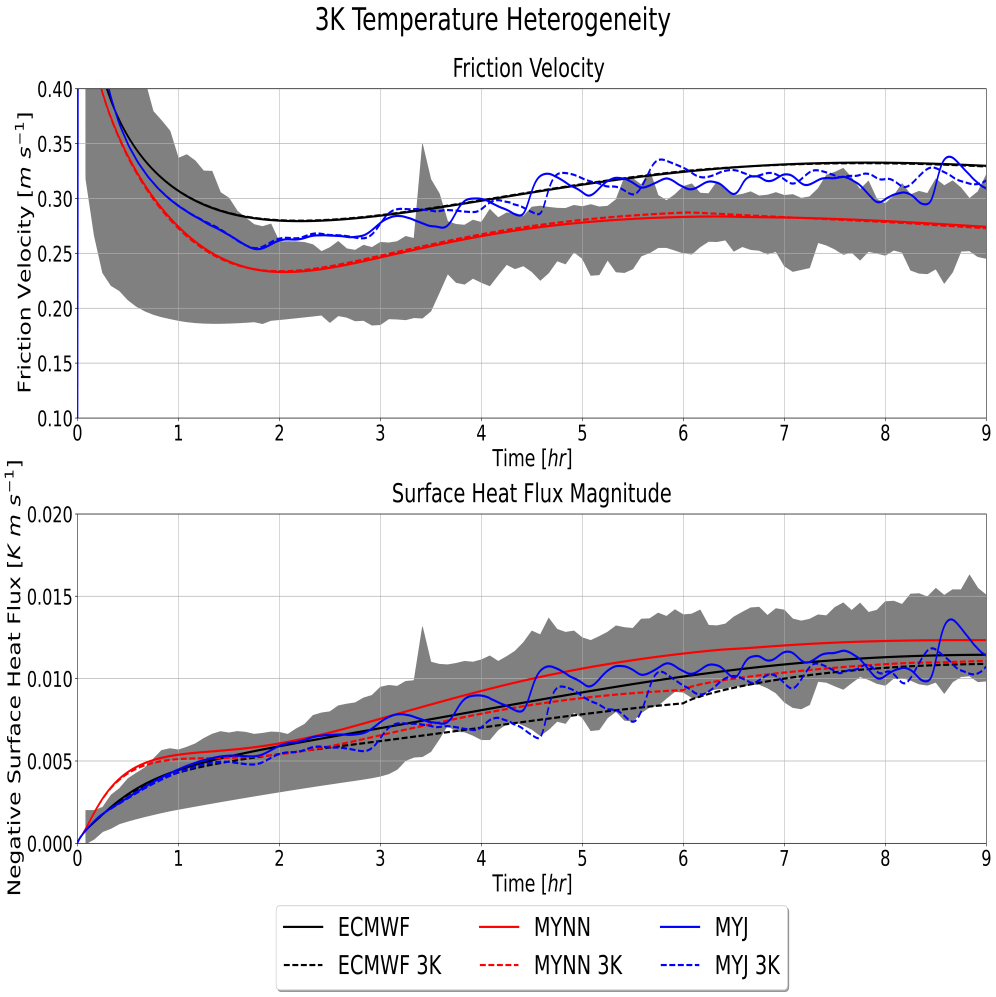

Figure 4.3: Time series of the friction velocity (top) and surface kinematic heat flux magnitude (bottom) with the homogeneous case (solid) and the TM with 3K patches (dashed). The ECMWF model is colored black, the MYJ blue, and the MYNN red. The shaded grey represents the spread of the LES from GABLS1.

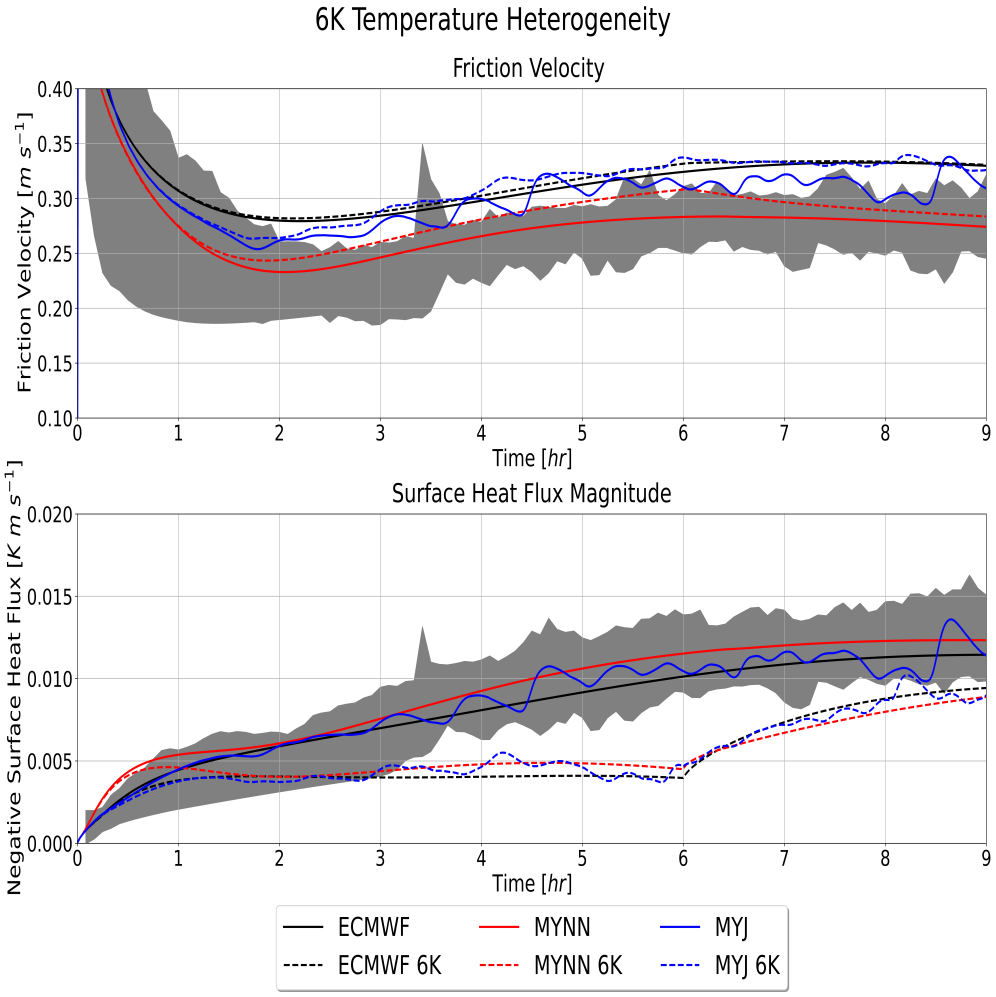

Figure 4.4: Same as previous but for 6K patches.

With the Modified Tile Model (MTM) the Obukhov length is smaller in magnitude for each scheme when compared to the original TM scheme, but larger than the original (see Table 4.2). The MYNN scheme shows the same type of pattern in the time series of the boundary layer height, with the MTM boundary layer height being lower than the tile model but higher than the homogeneous simulation. A similar pattern is observed in the ECMWF scheme, but converge on approximately the same value in the final hour of the simulation with difference between all the ECMWF schemes being less than $5m$. As previously seen, the time series data of the MYJ scheme is very noisy so

a visual trend is hard to pick out, but mean final hour values in Table 4.2 indicate the same trend of h being less than the TM scheme but larger than the homogeneous case.

A similar type of pattern is exhibited in the time series of the kinematic heat fluxes for the PBL schemes with the MTM as shown in Figure 4.5 and 4.6. For the MTM with 3K patches, the same trend from before is seen with all of the MTM simulations across the PBL schemes falling between the homogeneous case and the TM. This is due to the modification made to the stability corrections described in Chapter 2, where the kinematic heat fluxes estimations are improved over the stable patch. The time series trace of the friction velocity in do not exhibit this same trend that has been seen before, but now approach the same value with little differences. This is due to the direct relation the surface heat fluxes have to the temperature heterogeneity, while the friction velocity does not. For patches of 6K, similar trends in the time series of the surface heat flux and momentum flux are found. The values of these variables lined up between the TM scheme and the homogeneous case. The trend in the 6K case was more clear as the differences between the homogeneous case and the TM were larger than the 3K case.

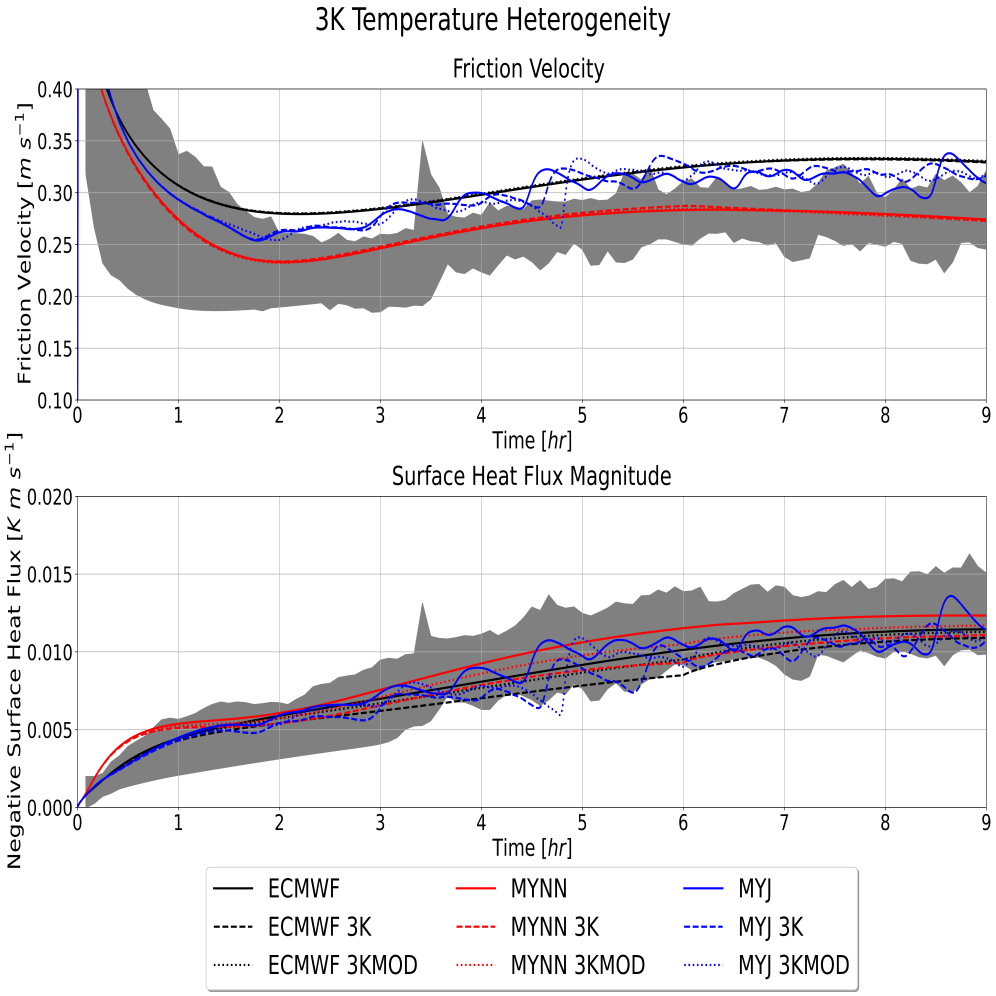

Figure 4.5: Time series of the friction velocity (top) and surface kinematic heat flux magnitude (bottom) with the homogeneous case (solid), the TM with 3K patches (dashed), and the MTM with 3K patches (dotted). The ECMWF model is colored black, the MYJ blue, and the MYNN red. The shaded grey represents the spread of the LES from GABLS1.

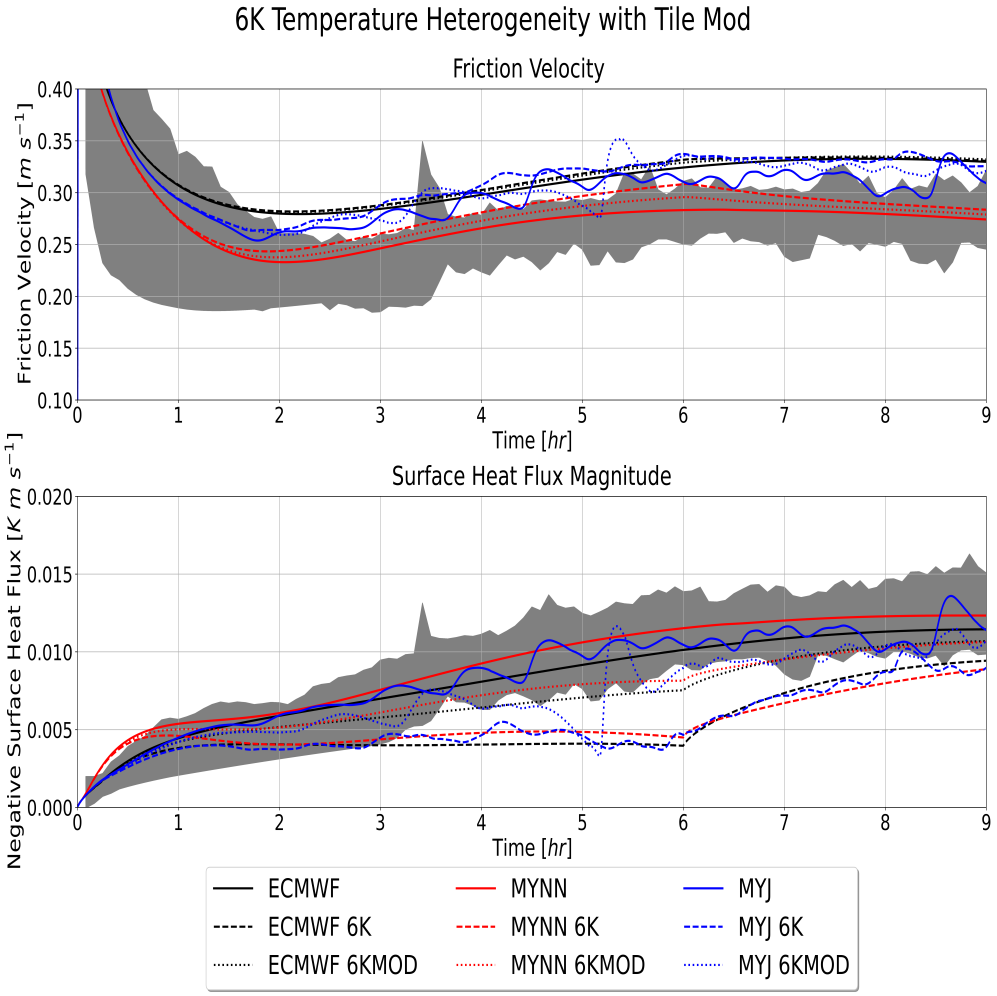

Figure 4.6: Same as previous but for 6K patches.

Simulation Runs					
Case	h [m]	L [m]	u_* [ms^{-1}]	$\langle w'\theta' \rangle$ [Kms^{-1}]	$\langle u'w' \rangle$ [m^{2}s^{-2}]
LES Min	149.1	112.2	0.257	-0.013	0.066
LES Max	198.2	162.4	0.307	-0.010	0.094
ECMWF	346.0	214.6	0.331	-0.011	0.110
ECMWF 3K	346.9	225.2	0.331	-0.011	0.110
ECMWF 6K	350.1	269.4	0.332	-0.009	0.114
ECMWF 6K Mod	348.7	236.3	0.334	-0.011	0.113
MYJ	147.3	180.7	0.313	-0.011	0.098
MYJ 3K	148.7	202.4	0.318	-0.011	0.102
MYJ 6K	170.4	268.5	0.332	-0.009	0.113
MYJ 6K Mod	157.7	214.9	0.322	-0.010	0.105
MYNN	171.2	115.7	0.277	-0.012	0.077
MYNN 3K	177.9	128.3	0.276	-0.011	0.0773
MYNN 6K	210.7	186.5	0.286	-0.009	0.086
MYNN 6K Mod	188.8	143.3	0.282	-0.010	0.082

Table 4.2: Mean values for the final hour of the simulation using surface temperature heterogeneity for the boundary layer height (h), Obukhov Length (L), friction velocity (u_*), surface heat flux ($\langle w'\theta' \rangle$) and surface momentum flux ($\langle u'w' \rangle$).

4.2.2 Vertical Profiles

Vertical profiles of temperature and wind speed averaged over the final hour of the simulation are shown in Figure 4.7. The MYNN and MYJ both have a clearly defined low-level jet (LLJ) that develops about 200 m above the ground. The MYJ LLJ is slightly stronger than the MYNN but lower in height. The ECMWF scheme does not produce this feature but has a monotonically increasing wind profile that peaks at the top of the domain $z = 400\,\mathrm{m}$. In terms of verification, the MYJ and MYNN profiles both closely resemble the profiles from the LES of GABLS1 as shown in the shaded grey area of Figure 4.7.

Upon initial inspection the temperature profiles look to be very similar between all three PBL schemes. The MYJ and MYNN schemes are located in the center of the spread of the LES results from GABLS1. The ECMWF scheme is warmer than the other schemes above $z = 75\,\mathrm{m}$ to approximately $z = 200\,\mathrm{m}$ with a near linearly decreasing profile. In this layer the MYJ and MYNN schemes have more curvature, especially in the region $z = 150\,\mathrm{m} - 250\,\mathrm{m}$, resulting in a kink in the potential temperature profile. The height at which this occurs is slightly higher for the MYNN scheme (220 m) than the MYJ (190 m).

The profile of the kinematic momentum flux show disparities between the three PBL schemes. The MYNN scheme is the best performer of the three by being near to the center of the spread of the LES. The MYJ and ECMWF both have surface momentum flux values that are larger than the edge of the LES by approximately $0.2\,\mathrm{m^2\,s^{-2}} - 0.3\,\mathrm{m^2\,s^{-2}}$. Despite having different surface values, all of the schemes generally have the same shape to the profile. The MYJ and MYNN schemes decrease to zero the fastest and reaching a minimum near $z = 200\,\mathrm{m}$, while the ECMWF obtains its minimum at the top of the model domain at $z = 400\,\mathrm{m}$.

The profiles of heat flux exhibit the same behavior across all three PBL scheme. The best behavior of the three PBL schemes occurs in the kinematic heat flux profiles with each scheme located in the center of the spread of the LES. The three PBL schemes have surface values of approximately $-0.012\,\mathrm{K\,m\,s^{-1}}$ that decrease to zero at different rates. the MYJ scheme decreases the fastest obtaining a minimum value at around 250 m. The MYNN scheme is slightly slower decreasing to zero near $z = 250\,\mathrm{m}$, while the ECMWF doesn't reach zero until the model top.

With the TM there were no visually distinguishable differences with the ECMWF scheme in the profiles of wind speed. The 1.5-order schemes showed more significant differences between the two. In the MYNN scheme, the height of the LLJ increased, but the maximum wind speed is lower. For MYJ the height of the LLJ also increased, but had the same peak wind speed. The wind maximum for the MYJ scheme occurs at approximately the same location but has a different shape to the profile with a sharper LLJ. Increasing the temperature difference to 6K reveals more striking differences between the surface schemes. The height of the LLJ is higher in the MYNN and MYJ scheme, and the peak maximum velocity is lower in magnitude.

Surface patches of 3K and 6K using the TM show a warming of the boundary layer in the vertical profile of potential temperature. All three PBL schemes have approximately the same level of warming at the surface, but the MYJ and MYNN scheme have a smaller lapse rate than the ECMWF scheme in the lower boundary layer. In the 6K case, the warming is more pronounced with the vertical profiles of temperature becoming near neutral in the lower part of the boundary layer. In the MYNN scheme specifically, an increase in the boundary layer height is evident with the temperature inversion located approximately 50 m higher.

Using the TM with patches of 3K, the kinematic momentum flux at the surface showed almost no change, while a more clear increase in the surface momentum flux

was seen in the 6K case. With the increase in surface momentum flux, the height at which the fluxes decreased to zero slightly increased in each case. This agrees with the time series data of the boundary layer height which is defined in terms of the momentum flux. More striking differences were noted for both the 3K and 6K case in the profiles of the kinematic heat fluxes. At the surface the kinematic heat flux value decreased across all three PBL schemes.

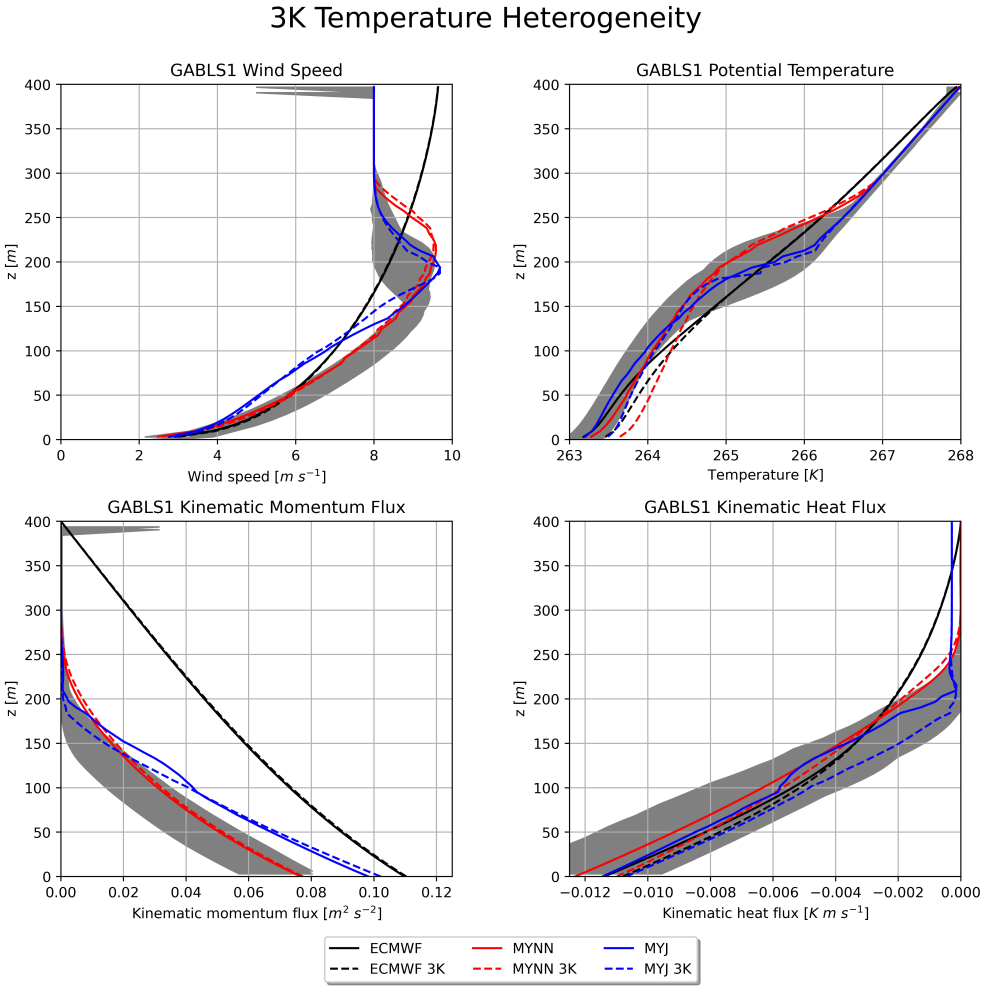

Figure 4.7: Vertical profile of the wind speed (top-left), potential temperature (top-right), kinematic heat flux (bottom-left), and kinematic momentum flux (bottom-right) averaged over the final hour of the simulation for the homogeneous case (solid) and the TM with 3K patches (dashed). The ECMWF model is colored black, the MYJ blue, and the MYNN red. The shaded grey represents the spread of the LES from GABLS1.

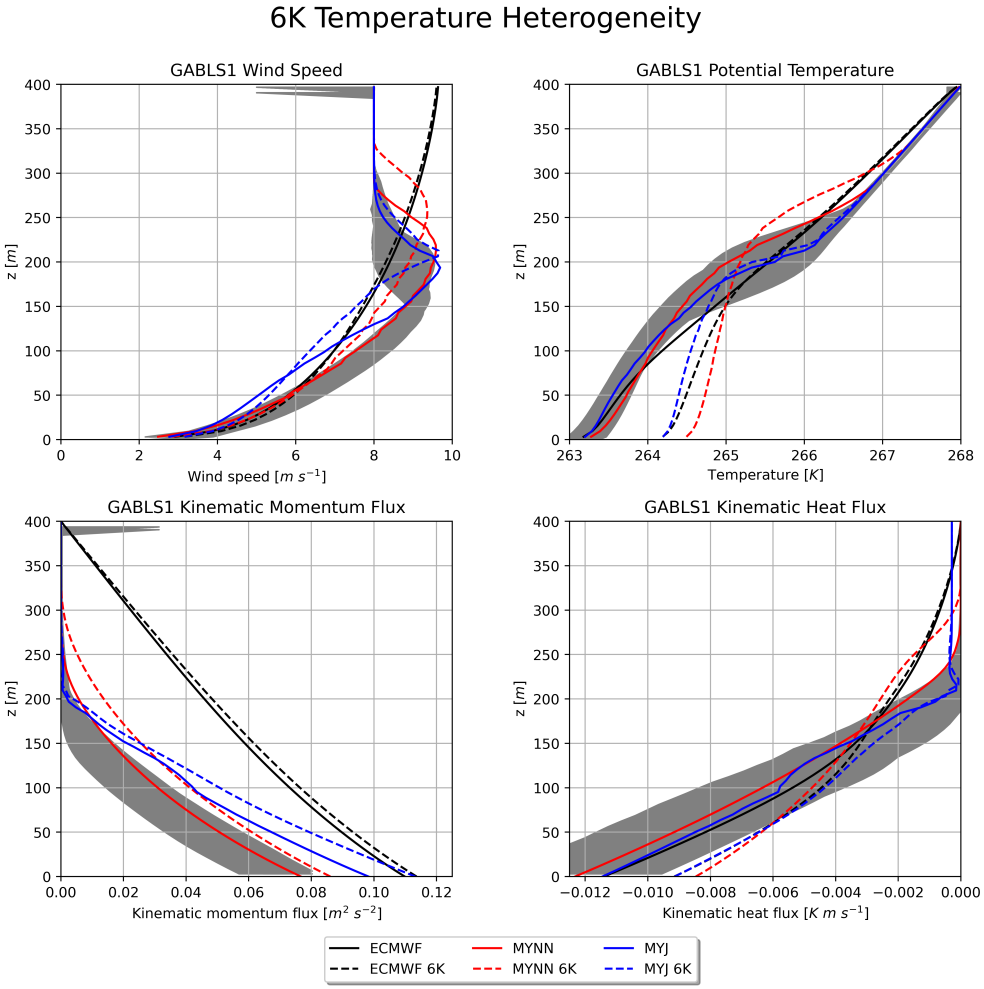

Figure 4.8: Same as previous but for 6K patches.

With the MTM the vertical profiles lie between the homogeneous case and the TM. As discussed in Chapter 2, the MTM works to improve surface flux estimations by accounting for advection over the cold stable patch. This acts to decrease the surface flux values from the TM, but still remaining larger than the homogeneous case of MOST. The profiles of wind speed in the ECMWF and MYNN scheme have nearly indistinguishable differences with the 3K temperature difference. More clear differences are seen in the 6K case with the MTM being between the homogeneous case and the

TM. This same trend of this also seen in the vertical profiles of potential temperature and is most pronounced in the 6K case.

The profiles of the kinematic momentum flux have almost no difference upon visual inspection for the ECMWF and MYNN schemes, similar to what was seen in the wind speed profile. The most significant differences in the MYJ scheme occur in the $100\,\mathrm{m} - 200\,\mathrm{m}$ layer, where spread begins between the PBL scheme in the wind profile. The kinematic heat flux profiles are messy due to their similar values, but the MTM values were between the homogeneous case and the TM, similar to what is observed in the potential temperature profile.

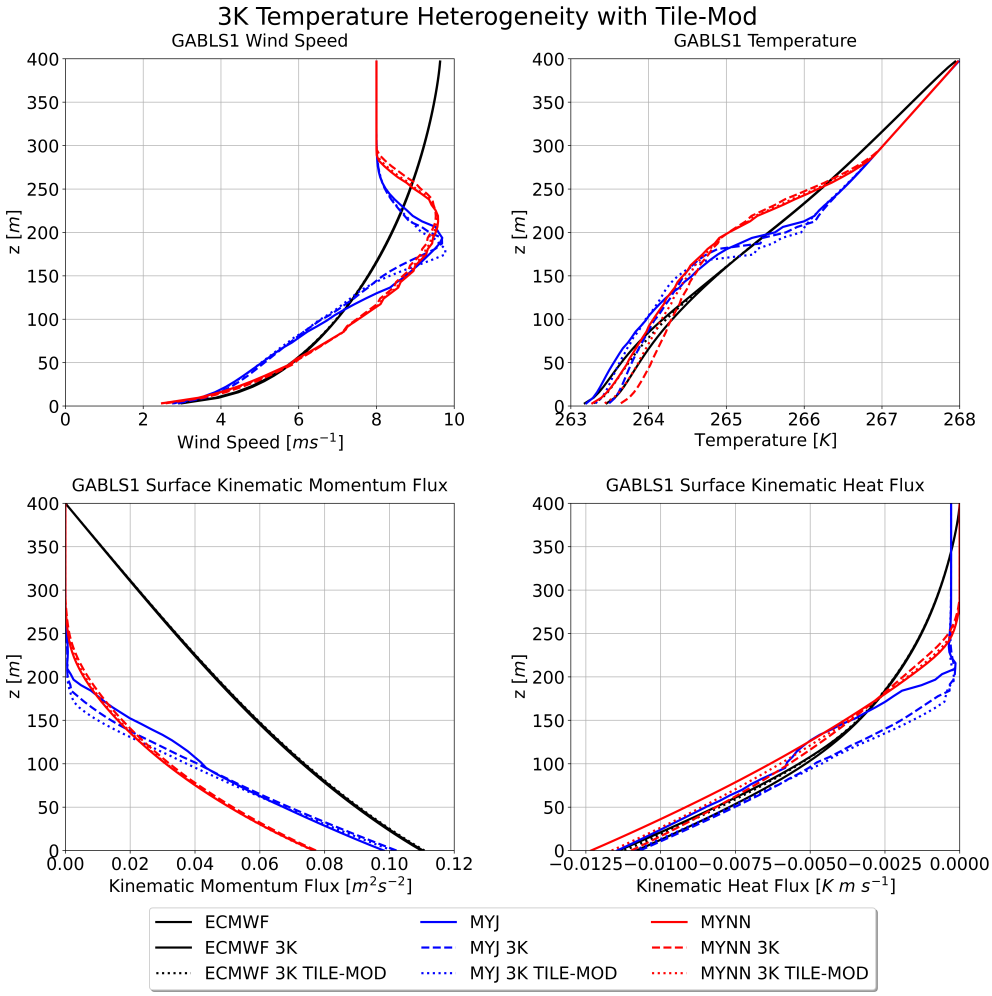

Figure 4.9: Vertical profile of the wind speed (top-left), potential temperature (top-right), kinematic heat flux (bottom-left), and kinematic momentum flux (bottom-right) averaged over the final hour of the simulation for the homogeneous case (solid), the TM with 3K patches (dashed), and the MTM with 3K patches (dotted). The ECMWF model is colored black, the MYJ blue, and the MYNN red.

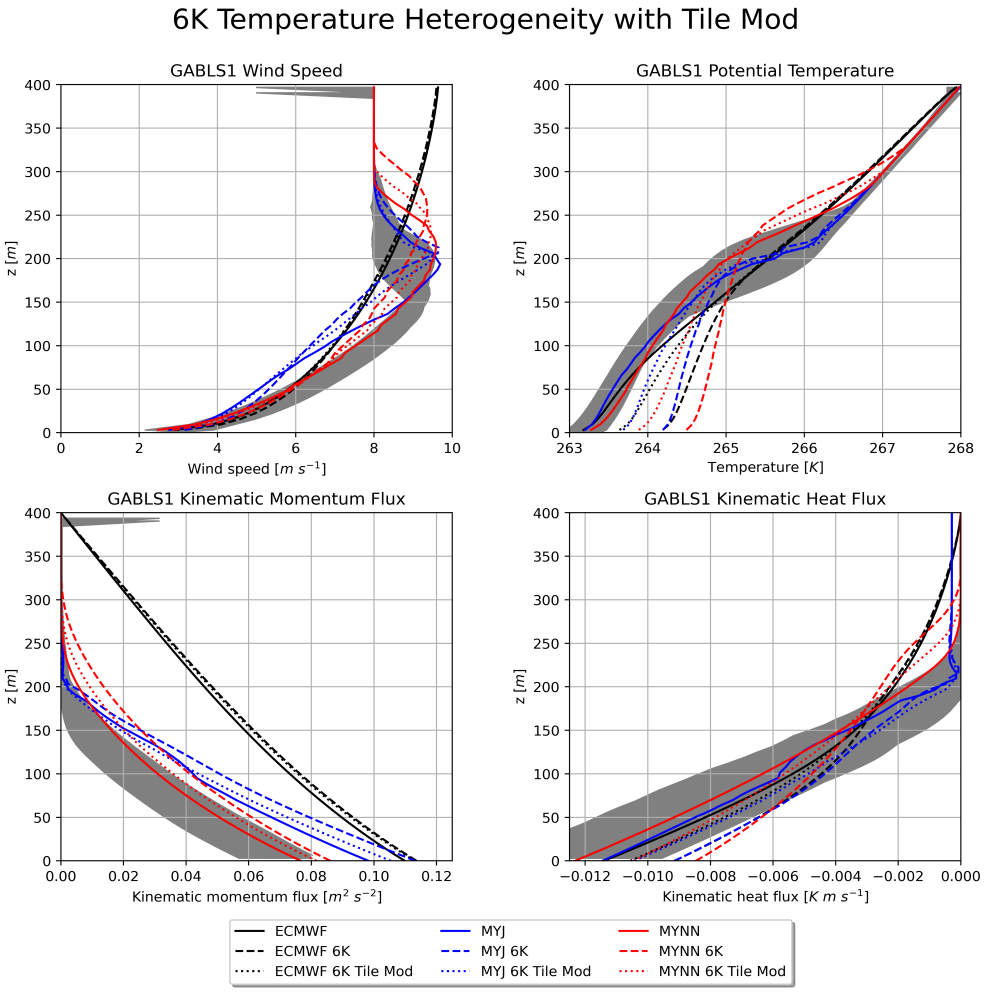

Figure 4.10: Same as previous but for 6K patches.

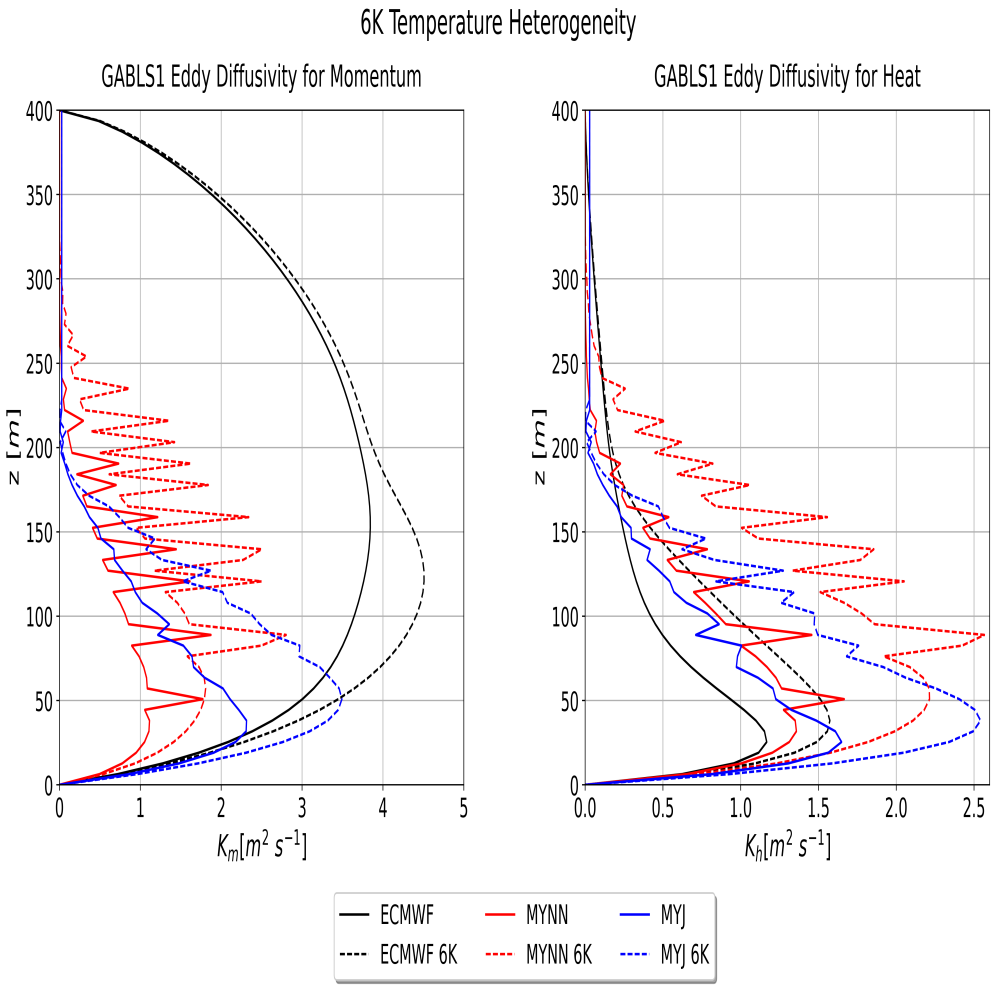

Figure 4.11: Vertical profile of the eddy diffusivities for heat and momentum for the homogeneous case (solid) and the TM with 6K patches (dashed). The ECMWF model is colored black, the MYJ blue, and the MYNN red.

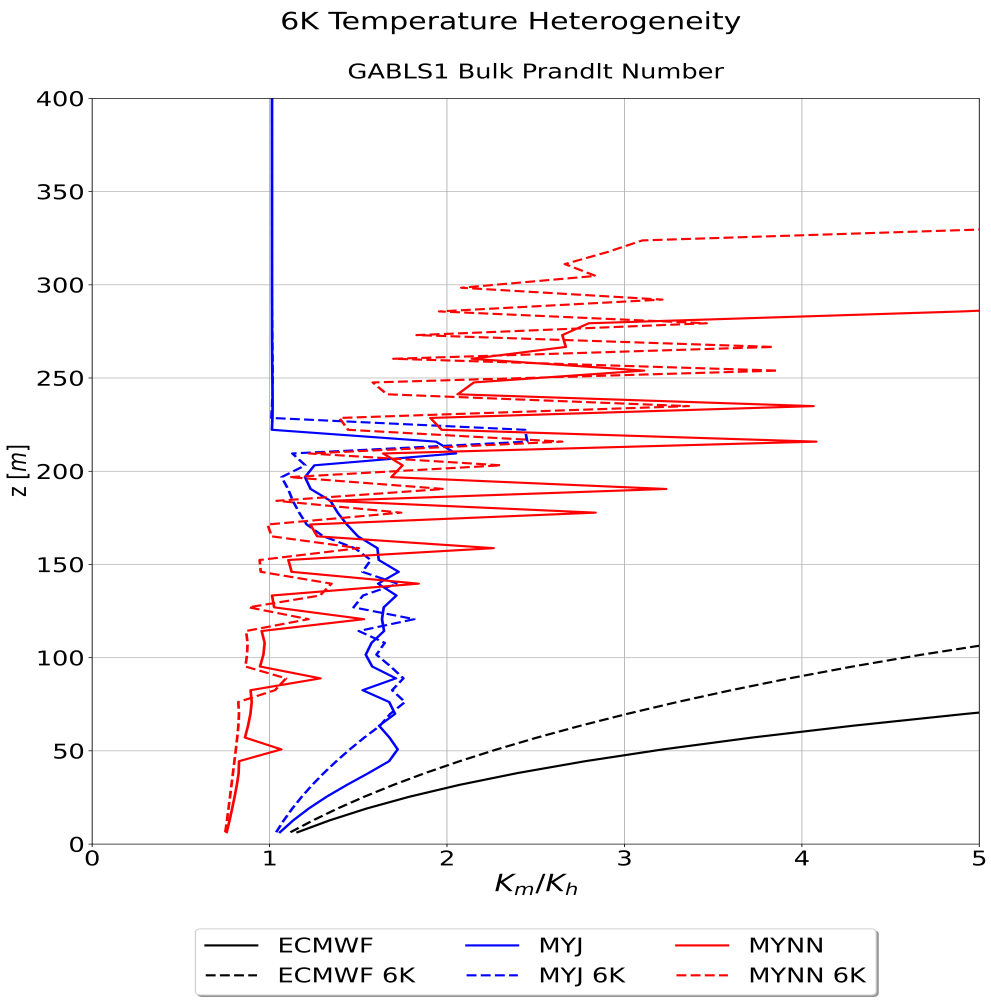

Figure 4.12: Vertical profile of the bulk turbulent Prandtl number for the homogeneous case (solid) and the TM with 6K patches (dashed). The ECMWF model is colored black, the MYJ blue, and the MYNN red.

The important difference between the various PBL schemes is based around the formulation for the PBL length scale, eddy diffusivities and stability functions. The eddy diffusivity K_m and K_h are plotted in Figure 4.11. The ECMWF scheme stands out over the other PBL schemes with large K_m values throughout the entire profile. For the homogeneous case a peak value of around $K_m = 3.8\,\mathrm{m^2\,s^{-1}}$ was obtained at about 150 m. The profile of K_h for the ECMWF scheme is much smaller in magnitude

and obtains a maximum very close to the ground near $z = 25\,\text{m}$. The MYNN and MYJ schemes both have smaller K_m values than the ECMWF scheme throughout the profile, and the maximum values are obtained closer to the surface at around 50 m. The MYNN has the smallest K_m values which is due to a different stability function formulation. The profiles of K_m and K_h in the MYNN scheme have numerous spikes which is the result of a piecewise definition for S_M and S_H based on differences between the level 2 TKE and 2.5 TKE calculation.

The behavior of how K_m and K_h change relative to one another can be explored through the bulk turbulent Prandtl number ($Pr_b = K_m/K_h$) as seen in Figure 4.12. Pr_b increases rapidly with height with the ECMWF scheme as $Pr_b > 7$ by $z = 100\,\text{m}$. This behavior is an outlier to the higher order schemes where Pr_b values are between 0.75 and 2 in the lowest 150 m. Between the higher order schemes, the MYNN has a near constant $Pr_b = 0.75$ in the lowest 100 m, and above which an increasing trend is seen. The MYJ has a different behavior where Pr_b increases from 1 at the surface to to 1.75 at $z = 50\,\text{m}$ where Pr_b is constant with height up to 150 m. Above this level Pr_b decreases to a value of 1 near $z = 225\,\text{m}$.

When incorporating the surface heterogeneity with the TM, the magnitude of the eddy diffusivities increases throughout the entire profile in each PBL scheme. The increase in magnitude of the eddy diffusivities are associated with the increases in the surface fluxes that were examined in the time series. The largest differences between the homogeneous case and using the TM occur near where height at which K_m and K_h obtain their maximum. With the TM, Pr_b is lower than the homogeneous case for each PBL scheme. With lower Pr_b values, K_h increased more significantly over K_m when incorporating the surface heterogeneity.

The PBL length scales for the three different boundary layer parameterizations are plotted in Figure 4.13. The ECMWF has the largest values of the boundary layer

length scale and achieves a maximum at the top of the model domain due to the simple length scale formulation that increases with distance from the surface. The MYJ scheme follows the ECMWF up to near $z = 40\,\mathrm{m}$ before the length scale begins to decrease. This is to be expected as the MYJ scheme length scale is similar to the ECMWF near the surface, and tends towards κz for small z. Above $z = 40\,\mathrm{m}$ the length scale decreases to zero at approximately $z = 200\,\mathrm{m}$. Near the top of the boundary layer, the MYJ scheme has spikes in the values of the turbulence length scale due to the restrictions made to the turbulence length scale for vanishing turbulence. The MYNN scheme has much smaller length scales than the ECMWF scheme, similarly to the MYJ. The MYNN length scale has a smoother profile that achieve a maximum around 150m and decreases to zero near $300\,\mathrm{m}$.

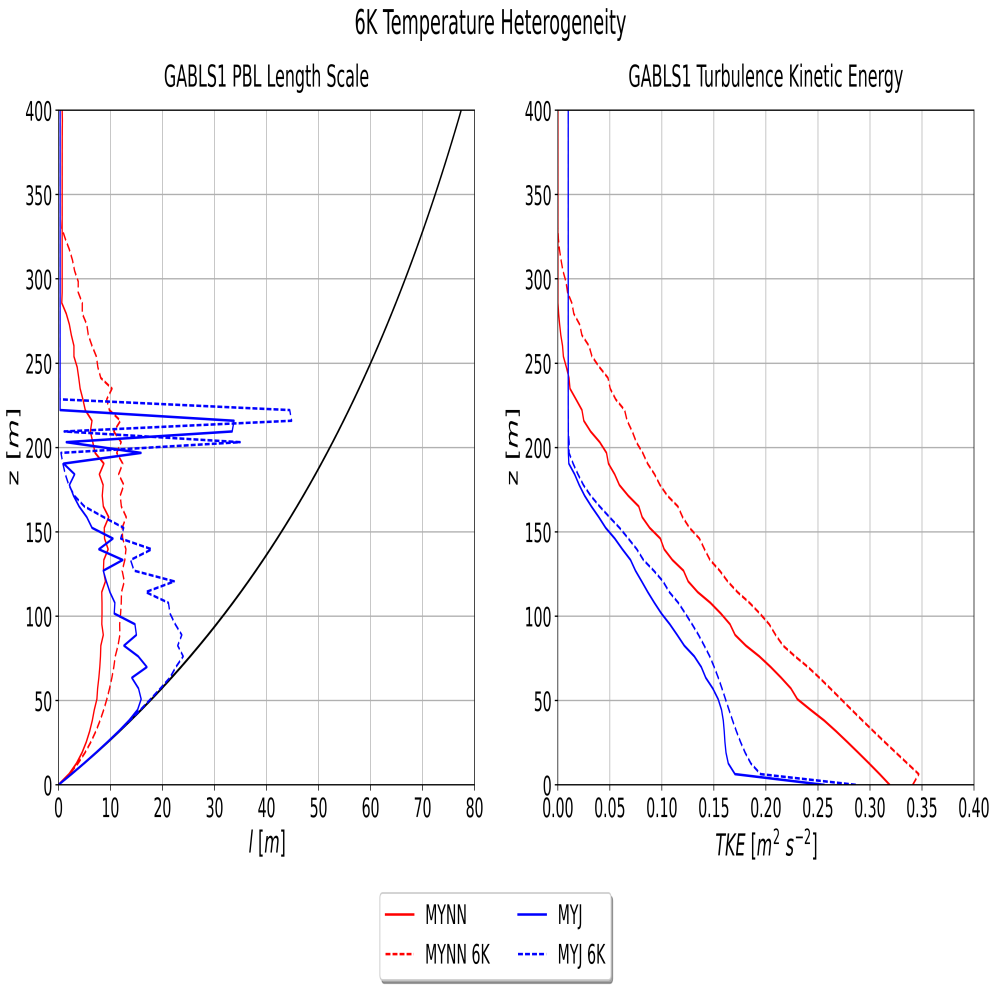

Figure 4.13: Vertical profiles of the turbulence length scale (left) and TKE (right) for the homogeneous case (solid) and the TM with 6K patches (dashed). The ECMWF model is colored black, the MYJ blue, and the MYNN red.

When surface temperature heterogeneity is present, the length scales in the MYJ and MYNN schemes increase throughout the profile, with no differences in the ECMWF as the length scale is based upon fixed variables. The higher order schemes both have an increase in the PBL length scale. MYJ follows the ECMWF curve up to a height of 65 m, higher than before. Above here the length scale begins to decrease to zero at the same height as the homogeneous case. The MYNN scheme has slightly large values

of l throughout the entire profile and decreases to zero at $z = 325\,\mathrm{m}$, a higher height than before.

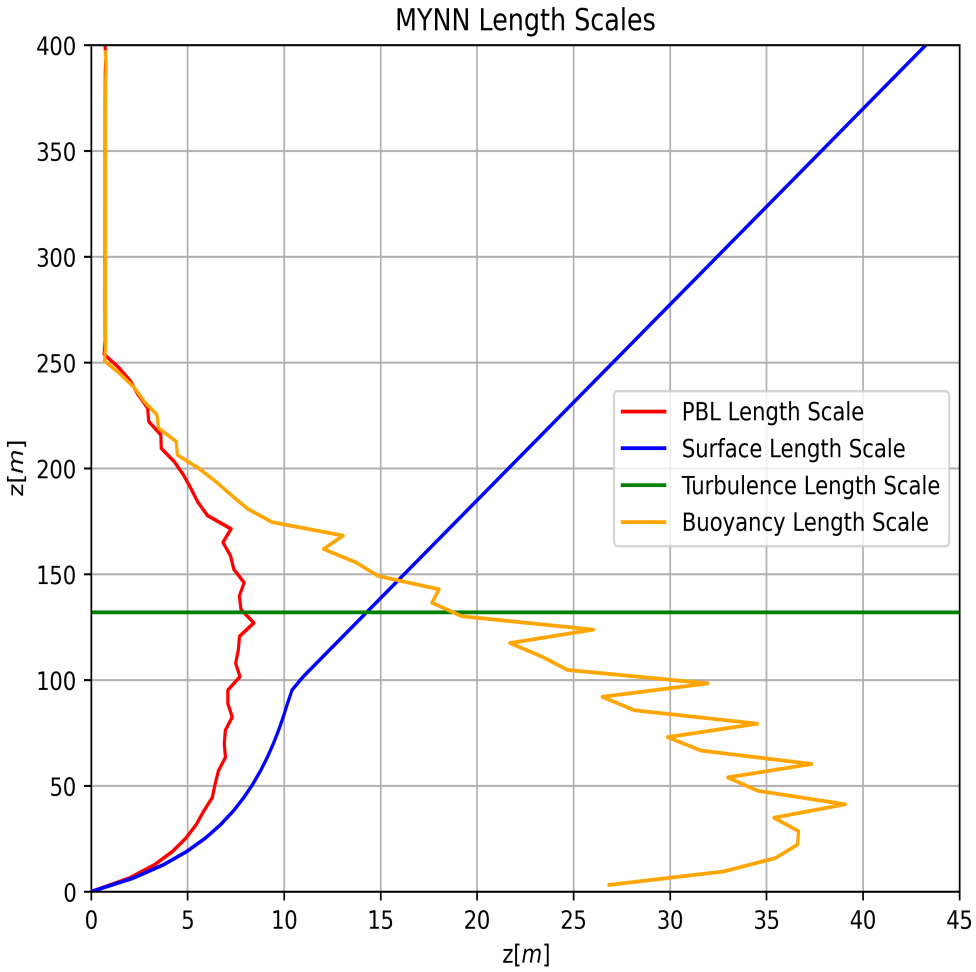

Figure 4.14: Vertical profiles of the various length scales from the MYNN scheme that define the turbulence length scale (red) including the surface length scale (blue), ABL based length scale (green), and buoyancy length scale (orange).

The MYNN has the smallest turbulence length scale of the three schemes, but can be examined further as it is composed of three individual length scales as seen in Figure 4.14. In the lowest 25 m, the PBL length scale (red) is dominated from the contributions of the surface length scale (blue). The buoyancy length scale has a peak

near to the surface at 40 m due to the large temperature gradients near the surface. Above this level the buoyancy length scale decrease towards zero and begins to have stronger contributions towards the master length scale. The maximum length scale occurs near the crossover of the surface length scale and the buoyancy length scale near 130 m. The length scale based on the boundary layer height (green) is not a vertical profile, but a scalar. To visualize the effects of this length scale, it is plotted as a horizontal line at its value of $z = 200$ m.

While the ECMWF is not a TKE-based scheme, the TKE is still worth analyzing due to the importance of TKE for the MYJ and MYNN schemes. The MYNN and MYJ both have a TKE profile with a maximum at the surface and decrease towards zero (Figure 4.13). The key difference between the two is the value at the surface and how quickly they decease towards their minimum values. The MYJ has a lower value than MYNN at the surface and reaches a minimum of zero at $z = 200$ m The MYNN scheme takes longer to decrease towards zero with a minimum near $z = 275$ m.

4.3 Roughness Differences

In addition to temperature heterogeneity, heterogeneity at the surface can be characterized by changes in surface roughness. These changes can also be investigated using an approach described in Chapter 2 to calculate an effective z_0 value based on the surface roughness values. The effective surface roughness values for momentum are calculated in an iterative loop with the blending height and the surface patches for z_0. This new effective surface roughness value is then used in regular MOST.

Using this approach the surface roughness values for two patches were adjusted to investigate how surface roughness altered the surface layer variables and mean profiles. In this scenario, one patch was held to a constant $z_0 = 0.1$ m while the other patch

was varied. The values are outputted are the effective aerodynamic roughness length z_{0e}, friction velocity u_*, Obukhov length L, and boundary layer height h. These mean values in the final hour of the simulation can be found in Table 1. The range of z_0 values chosen varies across a wide range of scales from $10^{-1} - 10^{-4}$. These ranges almost entirely make up the range of z_0 values determined for many of the land cover types from the USGS.

The trend from Table 4.3 can be seen that as the differences between z_0 patches grew larger, there was a decrease in the boundary layer height and Obukhov length.

Simulation Runs, $z_{01} = 0.1\,\mathrm{m}$						
Case	z_{0e} [m]	h [m]	L [m]	u_* [ms^{-1}]	$\langle w'\theta' \rangle$ [Kms^{-1}]	$\langle u'w' \rangle$[$\mathrm{m}^2\mathrm{s}^{-2}$]
LES Min	0.1	149.1	112.2	0.257	-0.013	0.066
LES Max	0.1	198.2	162.4	0.307	-0.010	0.094
ECMWF	0.1	346.0	214.6	0.331	-0.011	0.110
ECWMF $z_{02} = 0.01\,\mathrm{m}$	0.0495	337.3	196.7	0.312	-0.010	0.097
ECWMF $z_{02} = 0.001\,\mathrm{m}$	0.0387	334.0	191.0	0.305	-0.010	0.093
MYJ	0.1	147.3	180.7	0.313	-0.011	0.098
MYJ $z_{02} = 0.01\,\mathrm{m}$	0.0495	143.4	165.6	0.298	-0.011	0.089
MYJ $z_{02} = 0.001\,\mathrm{m}$	0.0387	100.8	165.1	0.278	-0.009	0.077
MYNN	0.1	171.2	115.7	0.277	-0.012	0.077
MYNN $z_{02} = 0.01\,\mathrm{m}$	0.0495	158.6	107.2	0.261	-0.011	0.068
MYNN $z_{02} = 0.001\,\mathrm{m}$	0.0387	155.2	105.1	0.257	-0.011	0.067

Table 4.3: Mean values for the final hour of the simulation using z_0 heterogeneity for the effective roughness length (z_{0e}), boundary layer height (h), Obukhov Length (L), friction velocity (u_*), surface heat flux ($\langle w'\theta' \rangle$) and surface momentum flux ($\langle u'w' \rangle$). Here z_{01} is the roughness length for patch 1, and z_{02} for patch 2.

A few select roughness patch values that were tested are plotted for the time series analysis in Figure 4.15. As the surface roughness value was decreased for one of the patches, the boundary layer height decreased in height across each PBL scheme. The Obukhov length also decreased in value as the surface roughness value was decreased. This results in more stable conditions with less vertical mixing as evident in the boundary layer data. The time series of the friction velocity and surface heat flux both show a decrease in magnitude in the values with the decreasing surface roughness values.

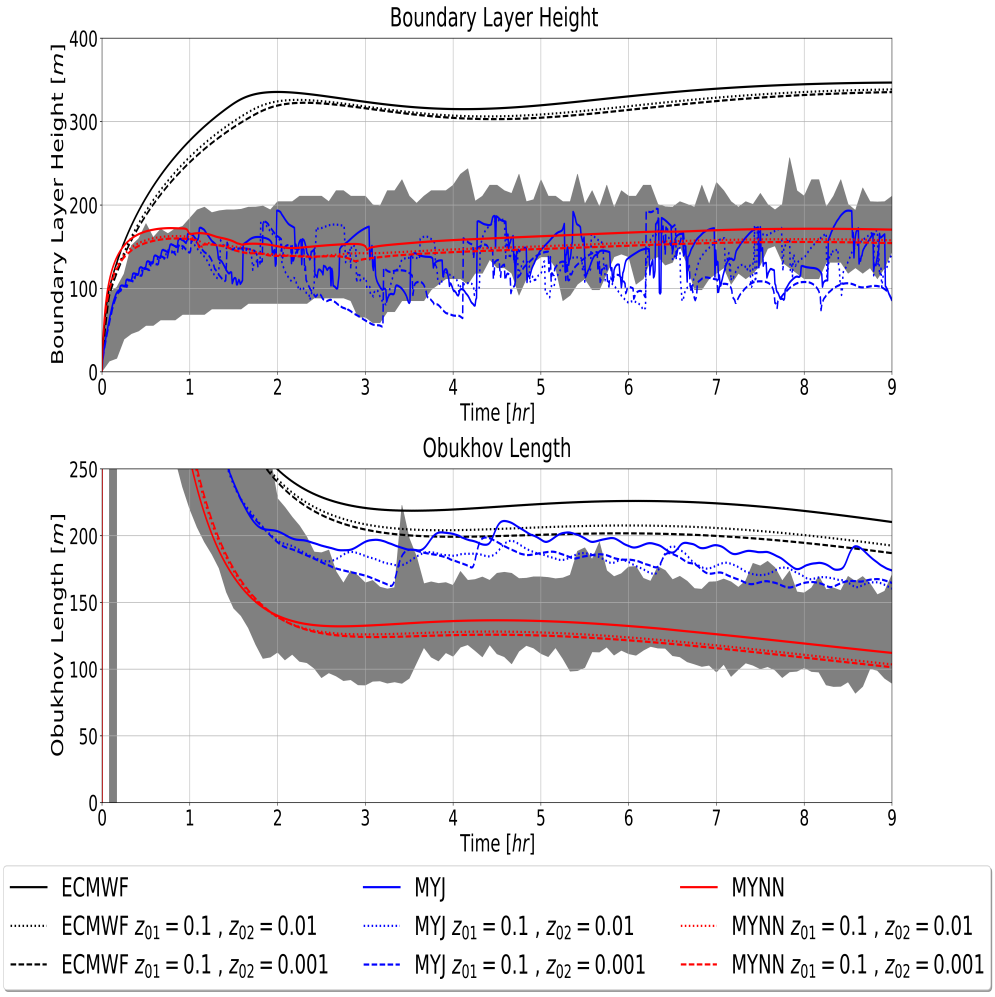

Figure 4.15: Time series of the boundary layer height (top) and Obukhov length (bottom) with the homogeneous case (solid) and surface heterogeneity for patch 2 values of $z_{02} = 0.01\,\mathrm{m}$ (dotted) and $z_{02} = 0.001\,\mathrm{m}$ (dashed). The ECMWF model is colored black, the MYJ blue, and the MYNN red. The shaded grey represents the spread from the LES of GABLS1.

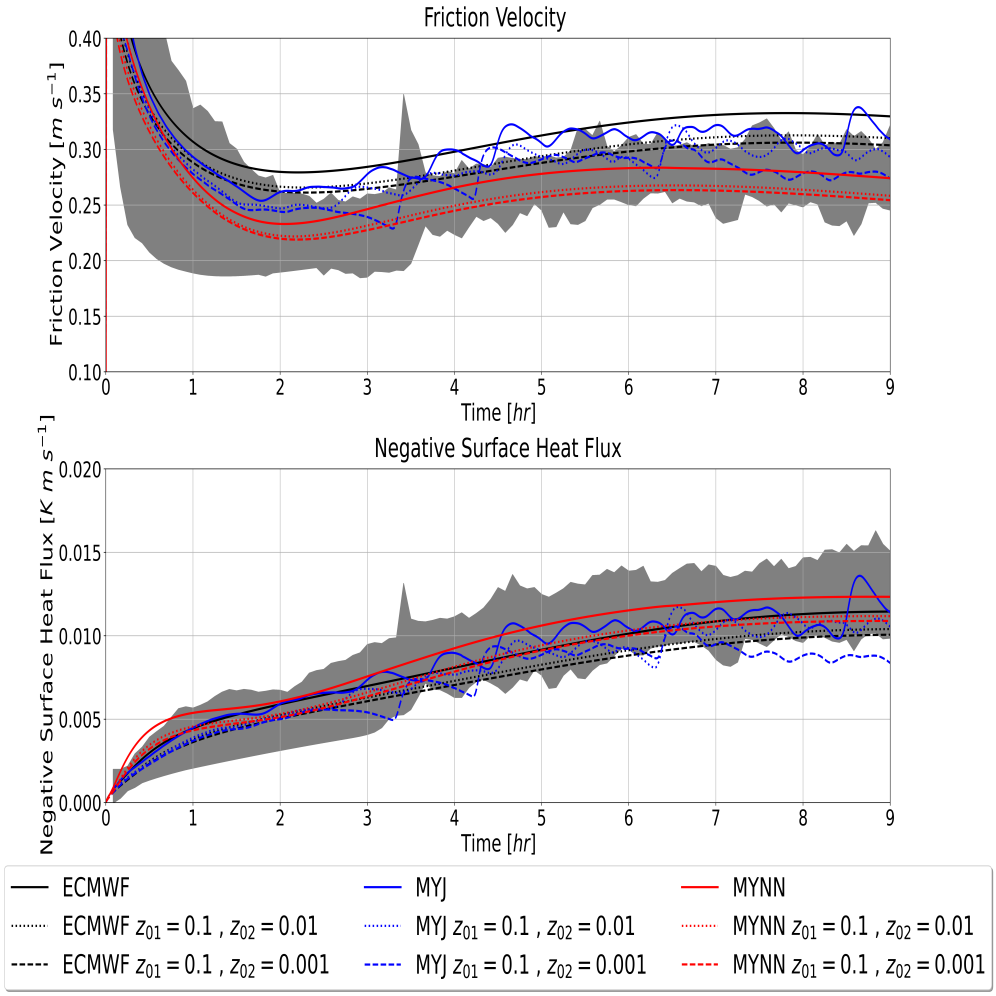

Figure 4.16: Time series of the friction velocity (top) and surface kinematic heat flux (bottom) with the homogeneous case (solid) and surface heterogeneity for patch 2 values of $z_{02} = 0.01\,\text{m}$ (dotted) and $z_{02} = 0.001\,\text{m}$ (dashed). The ECMWF model is colored black, the MYJ blue, and the MYNN red. The shaded grey represents the spread from the LES of GABLS1.

In addition to time series analysis, vertical profiles were examined for the same surface roughness values. In the MYNN scheme there is a decrease in the height of the LLJ as well as a decrease in the magnitude when there surface roughness of the patch was decreased from $z_0 = 0.01\,\text{m}$ to $z_0 = 0.0001\,\text{m}$. These trends were also noted in

the MYJ scheme, which had an extreme case of this happening with the $z_0 = 0.001\,\mathrm{m}$ case where the LLJ height was at $z = 145\,\mathrm{m}$. While the ECMWF does not produce a LLJ, there is some indication of strengthening of the winds closer to the ground and weakening at the top of the domain, which is similar to what is seen in the MYNN schemes.

The vertical profiles of temperature also exhibit a trend of increasing surface temperature for each PBL scheme. The potential temperature inversion in the MYNN scheme is slightly lower with the surface roughness differences, while almost no change is found in the MYJ scheme. The ECMWF continues to have the linearly decreasing temperature profile but is cooler than the homogeneous simulation. These differences in the surface temperature are related to the decrease in magnitude of the surface heat fluxes that can be seen in Figure 4.17. The same trend was found in the surface momentum fluxes, resulting in less vertical mixing and the lower boundary layer height.

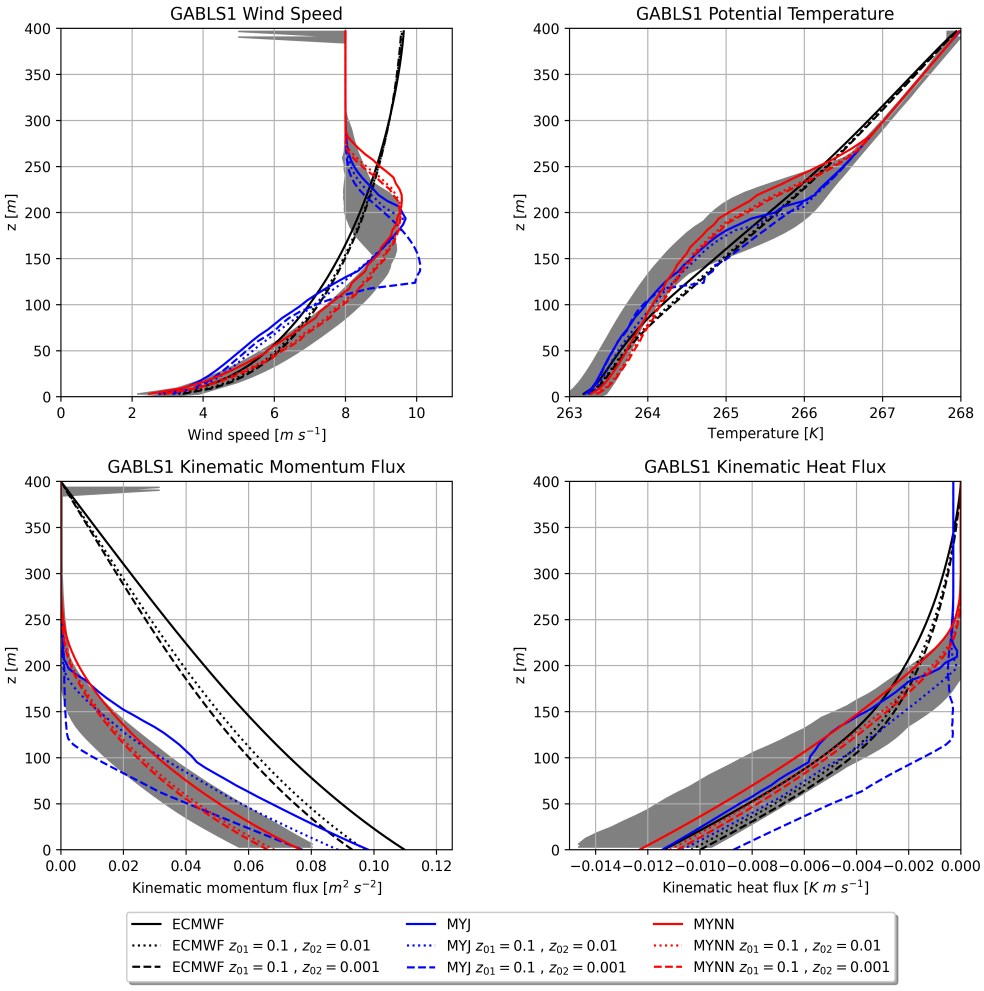

Figure 4.17: Vertical profile of the wind speed(top-left), potential temperature (top-right), kinematic heat flux (bottom-left), and kinematic momentum flux (bottom-right) with the homogeneous case (solid) and surface heterogeneity for patch 2 values of $z_{02} = 0.01\,\mathrm{m}$ (dotted) and $z_{02} = 0.001\,\mathrm{m}$ (dashed). The ECMWF model is colored black, the MYJ blue, and the MYNN red. The shaded grey represents the spread from the LES of GABLS1.

4.4 Discussion

The SCM was able to reproduce similar results to those of the LES from the GABLS1 experiments. Of the three PBL schemes tested, the MYNN scheme performed the best based upon being in the center of the spread of the LES. The other 1.5-order scheme, MYJ, performed the second best overall, while the ECMWF had the worst performance. The MYNN scheme may perform better than the MYJ due to the simpler formulation for the length scale and TKE. The MYJ scheme uses a complicated process to determine the turbulence length scale, as well as a linearization process to determine TKE. The MYNN scheme formulates the turbulence length scale based on three simple length scales.

The higher-order schemes were able to reproduce the LLJ feature that is seen in the LES, but the ECMWF has only a gradual decrease in wind with height. This was also true in the profiles of potential temperature, with the higher-order schemes resolving the subtle inversion at $z = 200\,\mathrm{m}$, but the ECMWF only having a linear decrease in height. This poor behavior is due to the simple relations made to parameterize the surface fluxes in the boundary layer.

The surface temperature heterogeneity investigated with the TM scheme showed an increase in the magnitude of the surface momentum fluxes, but a decrease in magnitude in the surface heat fluxes. The most significant changes in the surface fluxes were with the 6K case where large increases were seen in the kinematic heat and momentum fluxes. This led to slightly warmer profiles during the nighttime with increased vertical mixing as evident in the elevated LLJ. Using the MTM the surface fluxes simulated were between the homogeneous case and the TM. This was due to the improvement the MTM has with better estimating the kinematic heat fluxes from the stable (cooler) patch, which resulted in less mixing and cooling.

Investigating surface heterogeneity with surface roughness differences led to the result of a decrease in the kinematic surface fluxes for both momentum and heat with decreasing surface roughness values. This can be seen from MOST using Eq. 4.1,

$$U = \frac{u_*}{\kappa}\left[\ln\left(\frac{z}{z_{0m}}\right) - \psi_m(\zeta, \zeta_{0m})\right] \tag{4.1}$$

If the ratio of z/z_0 increases due to a decrease in z_0, this results in an increase in the natural log of the right hand side. Keeping everything else constant this makes a decrease in the friction velocity necessary to keep the left hand side of the equation equal. Using similar reasoning a similar result can be found for the kinematic heat flux by investigating Eq. 4.2,

$$\theta - \theta_s = \frac{\theta_*}{\kappa}\left[\ln\left(\frac{z}{z_{0h}}\right) - \psi_h(\zeta, \zeta_{0h})\right]. \tag{4.2}$$

With the smaller effective roughness values, the vertical profiles of wind speed had less mixing with a lower LLJ maximum, along with warmer surface temperatures and a shallower inversion.

While both temperature heterogeneity and surface roughness heterogeneity are difficult to compare, there are some interesting differences between the two. With the surface roughness heterogeneity, the effect on the fluxes are felt nearly equally in those of heat and momentum. When using the TM with lower temperature differences of 3K, the impacts are most strongly felt in the kinematic heat fluxes with much smaller differences in the kinematic momentum fluxes. Further increasing the heterogeneity to 6K the differences TM increases the kinematic surface fluxes for heat and momentum nearly equally.

Based on the results from GABLS1, the MTM and MYNN scheme should best be used to account for land-temperature heterogeneity in stable boundary layers. The

MTM had better surface flux estimations due to the better estimation of the surface heat fluxes from the cold (stable) patch. The MYNN scheme was the best performing PBL scheme when compared to the LES of GABLS1. While the MYJ and ECMWF performed well with the surface values of the kinematic heat and momentum flux, the MYNN performed the best when also analyzing the vertical profiles of wind speed and temperature, as well as the vertical profiles of the kinematic heat and momentum fluxes.

Chapter 5

Validation of SCM against GABLS2

5.1 Introduction

The second GABLS case was based on the Cooperative Atmospheric-Surface Exchange Study (CASE) 1999 based in Kansas during the early fall of 1999 (Svensson et al., 2011). Differing from GABLS1, the second GABLS experiment focused on investigating how well current turbulence parameterization schemes in models could represent a full diurnal cycle over relatively flat terrain. Here, the ECMWF and MYNN schemes are the only PBL schemes used due issues with numerical stability using MYJ. Further discussion of the numerical stability issues can be found in closing remarks section of Chapter 7.

In the GABLS2 case, the geostrophic wind is set to $9\,\mathrm{m\,s^{-1}}$ in the streamwise direction and $-3\,\mathrm{m\,s^{-1}}$ in the spanwise direction. The issue with this described in Svensson et al. (2011) is that, since the modeled simulation period consist of 59 hours over two full diurnal cycles, the geostrophic forcing was not constant over the entire period. In the first 16 hours of the simulation period the geostrophic forcing prescribed was too weak, and afterwards in the period it was too strong. To account for this, large-scale forcing was introduced 24 hours into the simulation through a sink term F_{LS} in the potential temperature equation. At the surface, the effective roughness length for momentum and heat were set to $z_{0m} = 0.03\,\mathrm{m}$ and $z_{0h} = 0.003\,\mathrm{m}$.

The initial run time for the model begins at 16 local time (LT), when conditions were unstable and moving towards the evening transition period. The initial vertical profile of potential temperature consist of three different stability layers as shown in Figure 5.1, with an initial potential temperature of 288 K. The layer in the lowest 200 m is unstable, and above which is a neutral profile until an inversion at 800 m. This is characteristic of a well mixed convective boundary layer. The surface temperature T_s at z_{0h} over the 59 hours period is prescribed in Celsius as multiple piecewise functions defined as

$$T_s = \begin{cases} -10 - 25cos(0.22t + 0.2) & t \leq 17.4 \\ -0.54t + 15.2 & 17.4 < t \leq 30 \\ -7 - 25cos(0.21t + 1.8) & 30 < t \leq 41.9 \\ -0.37t + 18.0 & 41.9 < t \leq 53.3 \\ -4 - 25cos(0.22t + 2.5) & 53.3 < t \leq 65.5 \\ 4.4 & t > 65.6 \end{cases} \tag{5.1}$$

where t is given in hours (LT) and the simulation time is given as $t - 16$. This is to set the model time to be at zero at the beginning of the simulation, as the time prescribed by the functions are given in LT, and begins at 16 LT. A portion of this surface temperature function is shown in Figure 5.1 for the first 36 hours of the simulation. For the TKE based schemes, a simple decreasing profile is used with a maximum of $0.5\,\mathrm{m^2\,s^{-2}}$ at the surface decreasing to a minimum value at 800 m.

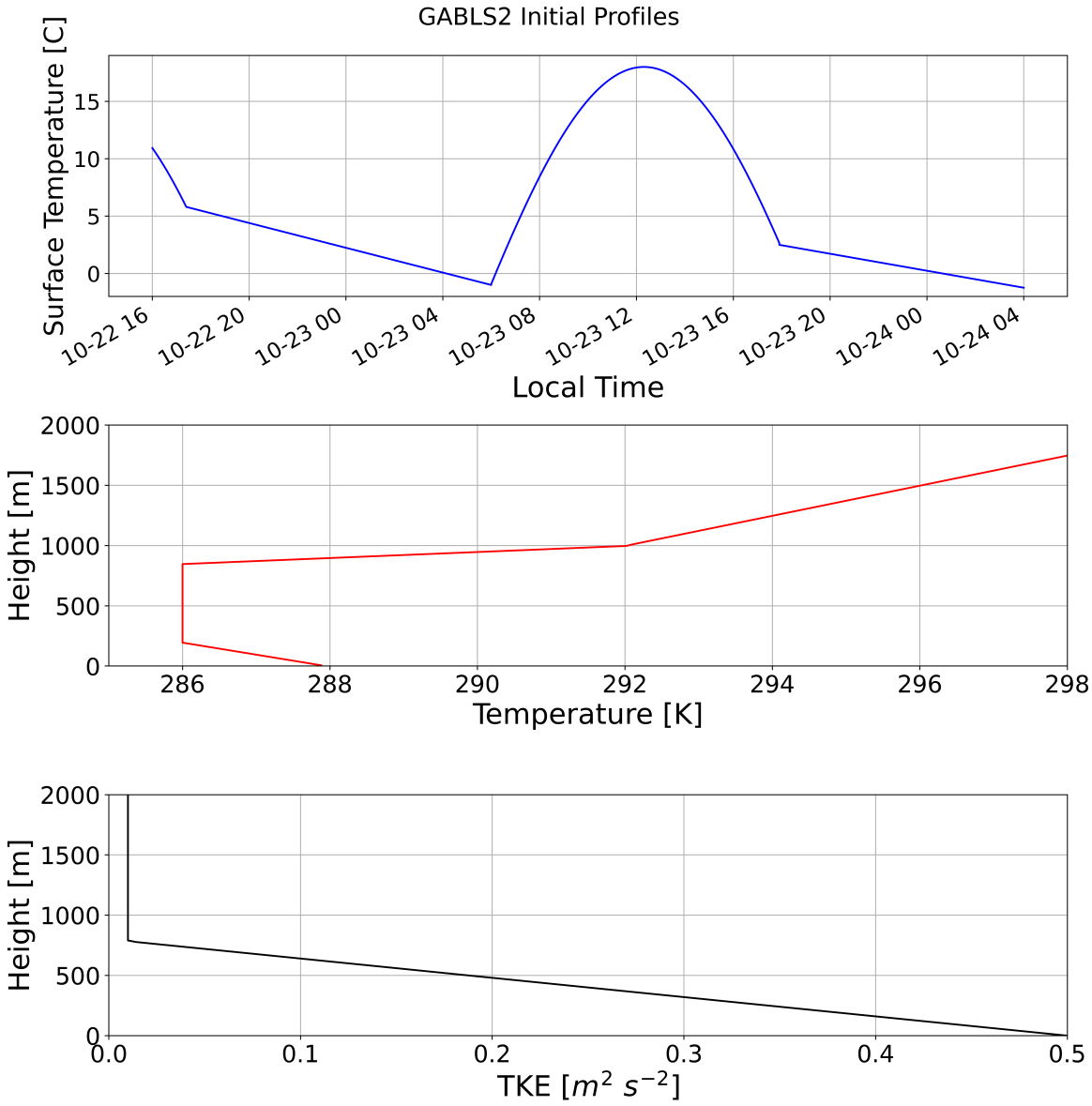

Figure 5.1: Initial profiles of the potential temperature (top), surface temperature (middle), and TKE (bottom) for the GABLS2 case.

A method similar to the one used in the GABLS1 case was used to generate the surface potential temperature heterogeneity. The cooling rates for each patch followed the same piecewise functions defined in Eq. 5.1. For the warmer patch, a value of 1.5 K is added, and for the cooler patch 1.5 K is subtracted to generate the 3K difference. For

the 6K patches a value of 3 K was added and subtracted. This resulted in the average surface temperature to be the same between the two patches.

The simulation lengths are long enough to encompass two full nighttime periods and one full day of solar insolation. The results from the simulation here are focused to the first 36 hours as that is what is primarily discussed in the literature (Svensson et al., 2011).

5.2 Surface Temperature Differences

5.2.1 Time Series

The time series of 2-m potential temperature and 10-m wind speed are shown in Figure 5.2. In the first night, all of the profiles show cooling of the 2-m temperatures that is similar to that of the spread of the SCM simulations from GABLS2. The MYNN is on the upper end the SCM spread throughout the night, while the ECMWF is in the middle of the SCM spread. Around the morning transition period both the MYNN and ECMWF scheme are in the middle of the spread of the SCM simulations and have a gradual increase in temperatures. The ECMWF has a smooth curve that resembles a cosine wave with a peak potential temperature of 14 °C at around 13 LT on 13 October, which is in the middle of the spread for the SCM simulations. The peak in the MYNN scheme is flattened and lower with a maximum value of approximately 13 °C, but this occurs at a later time near 15 LT on 13 October. Into the second night the exact same trend in the PBL schemes is seen with the MYNN being on the upper end the SCM spread throughout the night. Slightly different, the ECMWF is now on the lower end of the spread of the SCM and is approximately 2 °C cooler than the MYNN.

The wind speeds between the MYNN and ECMWF are very similar on the first night at around $2.5\,\mathrm{m\,s^{-1}} - 3\,\mathrm{m\,s^{-1}}$, well within the spread of the SCM simulations.

During the daytime the ECMWF had a slight increase in wind speeds to a maximum of $4\,\mathrm{m\,s^{-1}}$ slightly before 12 LT. While it is in the shaded grey indicating being in the spread of the SCM simulations, the sharp rise in wind speed that seems to be apparent in other schemes is not represented in the ECMWF. The MYNN scheme does have a sharp rise in wind speed with a maximum of $6.5\,\mathrm{m\,s^{-1}}$ near 11 LT, but this happens outside of the spread of the SCM simulations. Into the second night a dip is seen in the wind speed of the MYNN scheme around 16LT, before increasing to approximately the same value from the first night.

Incorporating the temperature heterogeneity with the TM showed large differences in the time series. Both the MYNN and ECMWF showed a increase in potential temperature during the first night, but the MYNN scheme was most significant with warming of approximately 1 K for the 3K and 2.5 K for the 6K heterogeneity. Around 06 LT all of the schemes begin to increase with the as surface heating begins. The differences between the homogeneous case and the TM become indistinguishable as the convective conditions work to mix out the effects of the surface heterogeneity.

With the TM a small decrease in the wind speed was found in the MYNN scheme as well as the ECMWF scheme, but this was most significant in the MYNN scheme. The increase in wind speed was largest in the 6K case where an increase of $0.5\,\mathrm{m\,s^{-1}}$ was found in the MYNN scheme. The MYNN scheme has higher wind speeds up until 11 LT, where after this time the values of the homogeneous case and the TM become the same. Into the second night the same trend from the first night is seen with the TM wind speeds being higher than the homogeneous case.

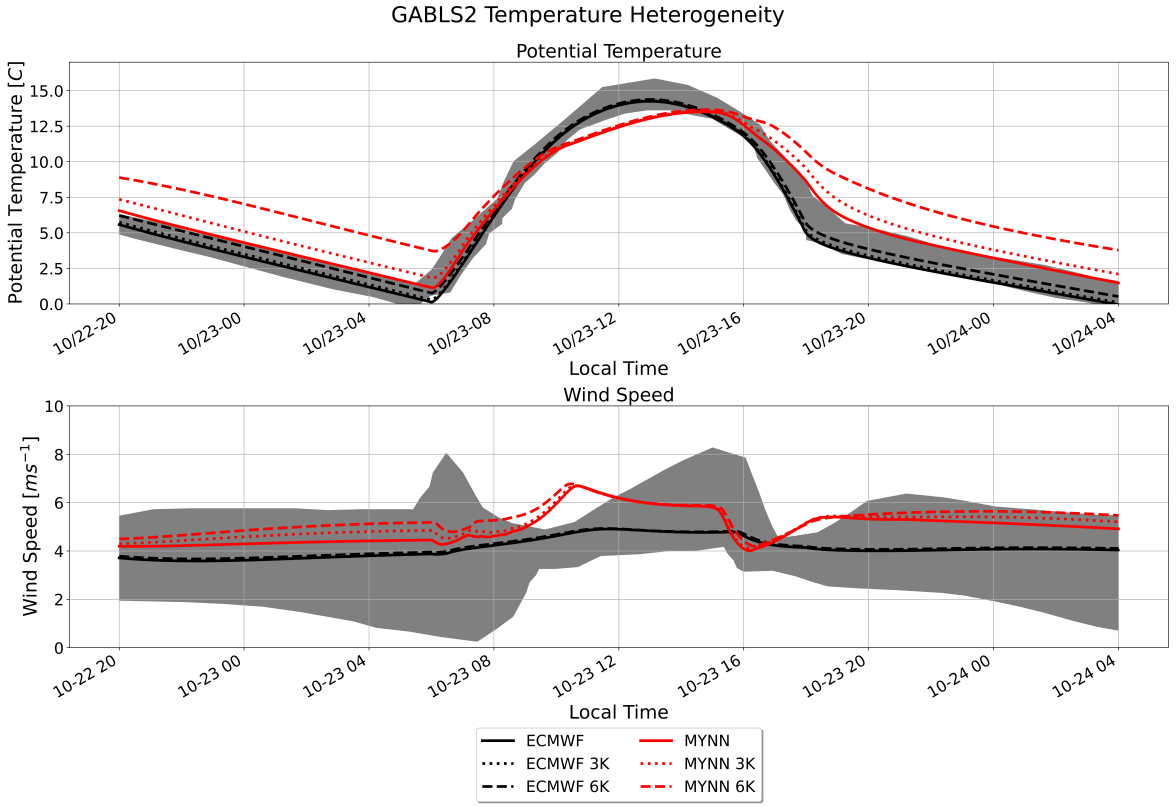

Figure 5.2: Time series of the surface potential temperature (top) and wind speed (bottom) for the homogeneous case (solid), the TM with 3K patches (dotted), and 6K patches (dashed). The ECMWF model is colored black, the MYNN red, and the shaded grey represents the spread of the SCM models from GABLS2.

With the MTM, the surface potential temperature during the first night is between the TM and the homogeneous case with the MYNN scheme. The MTM is much closer in value to the homogeneous case than the TM throughout the stable period. Once surface heating begins at around 06 LT the MTM has approximately the same value as the TM and the homogeneous case due to convective mixing. These same trends, albeit weaker, can also be seen in the ECMWF scheme.

The time series of wind speed follows a very similar pattern to what was seen in the potential temperature. The simulated wind speeds were weaker than the TM

and closer to the homogeneous case again and follow the same behavior throughout the stable period. During the night the wind speeds are fairly constant, but begin to increase around 7 LT. All of the models reach a peak at around 11 LT before collapsing onto the same value as the convective conditions mix out the heterogeneity effects. The wind speeds begin to decrease with a sharp drop located around 16 LT, where afterwards again the MTM is located between the two.

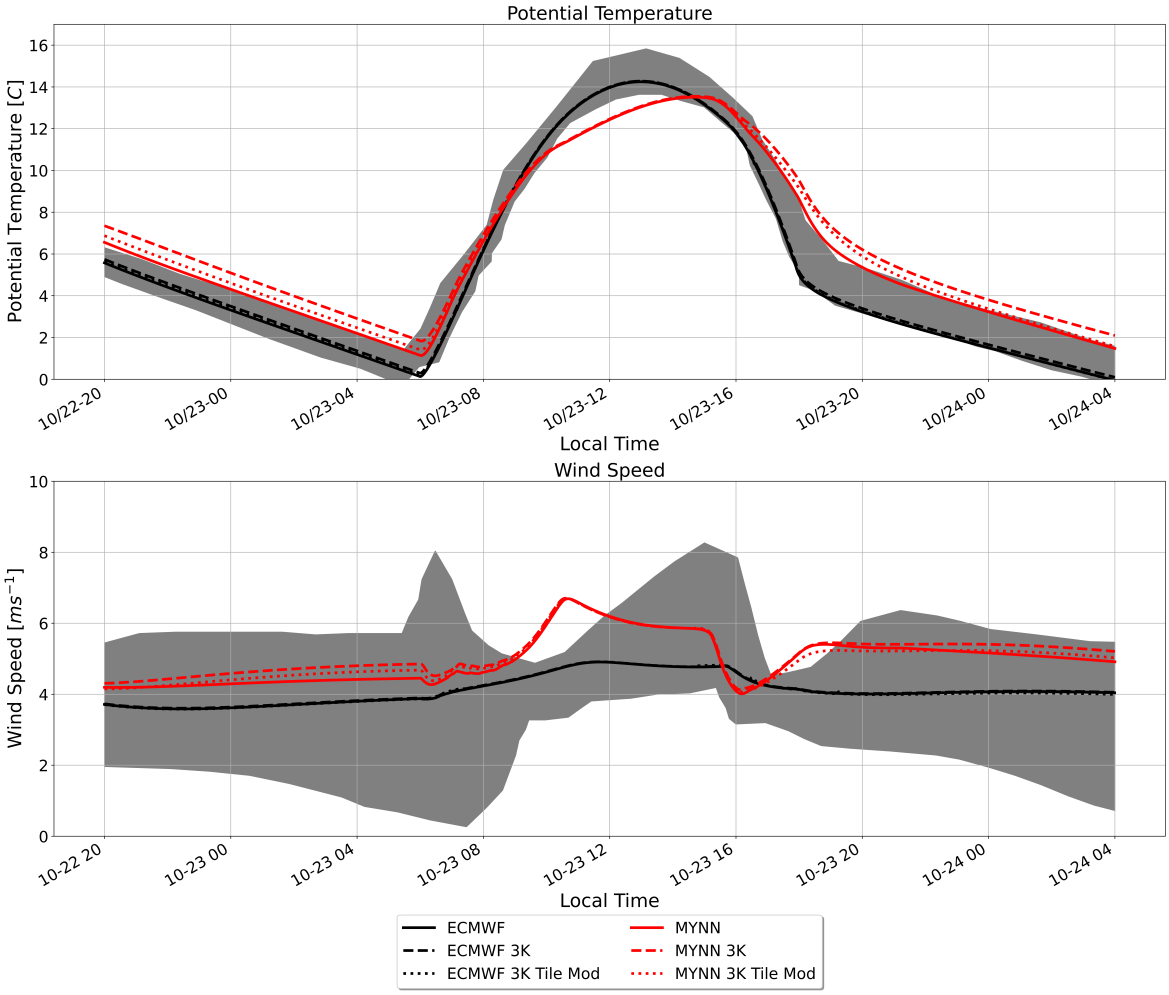

Figure 5.3: Time series of the surface potential temperature (top) and wind speed (bottom) for the homogeneous case (solid), the TM with 3K patches (dashed), and MTM with 3K patches (dotted). The ECMWF model is colored black, the MYNN red, and the shaded grey represents the spread of the SCM models from GABLS2.

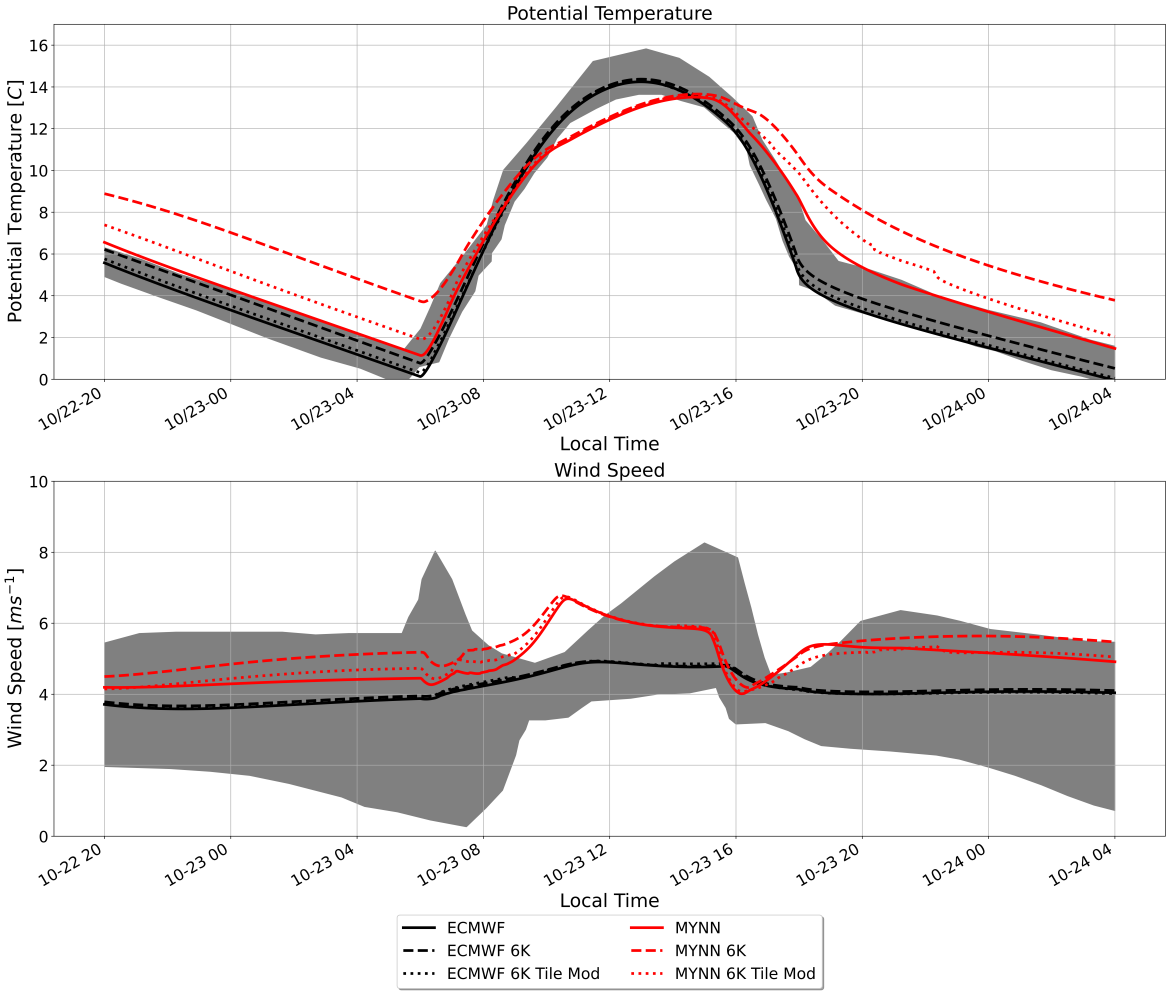

Figure 5.4: Time series of the surface potential temperature (top) and wind speed (bottom) for the homogeneous case (solid), the TM with 6K patches (dashed), and MTM with 6K patches (dotted). The ECMWF model is colored black, the MYNN red, and the shaded grey represents the spread of the SCM models from GABLS2.

The friction velocity in the ECMWF and MYNN scheme are both slightly smaller during the first night until near 06 LT. This is in contrast to what was observed in the GABLS1 case where the friction velocity was larger with the temperature heterogeneity. This may be attributed to smaller stability correction terms leading to smaller friction velocity values. The sensible heat fluxes in the both scheme do have the same trend

as GABLS1 with smaller in magnitude surface heat fluxes with increasing temperature heterogeneity.

During the nighttime the values of the friction velocity and sensible heat flux are small, so a zoomed in portion focused on the 20LT - 05LT period is plotted in Figure 5.6. It becomes more apparent of the trends described earlier. The 6K case clearly shows the decrease in the friction velocity and the decrease in magnitude of the surface heat fluxes. The PBL schemes also have the best agreement with GABLS2 in the friction velocity field as they are within the spread of the SCMs. Less agreement is seen in the sensible heat fluxes as the MYNN produces values that are too large in the beginning of the time examined.

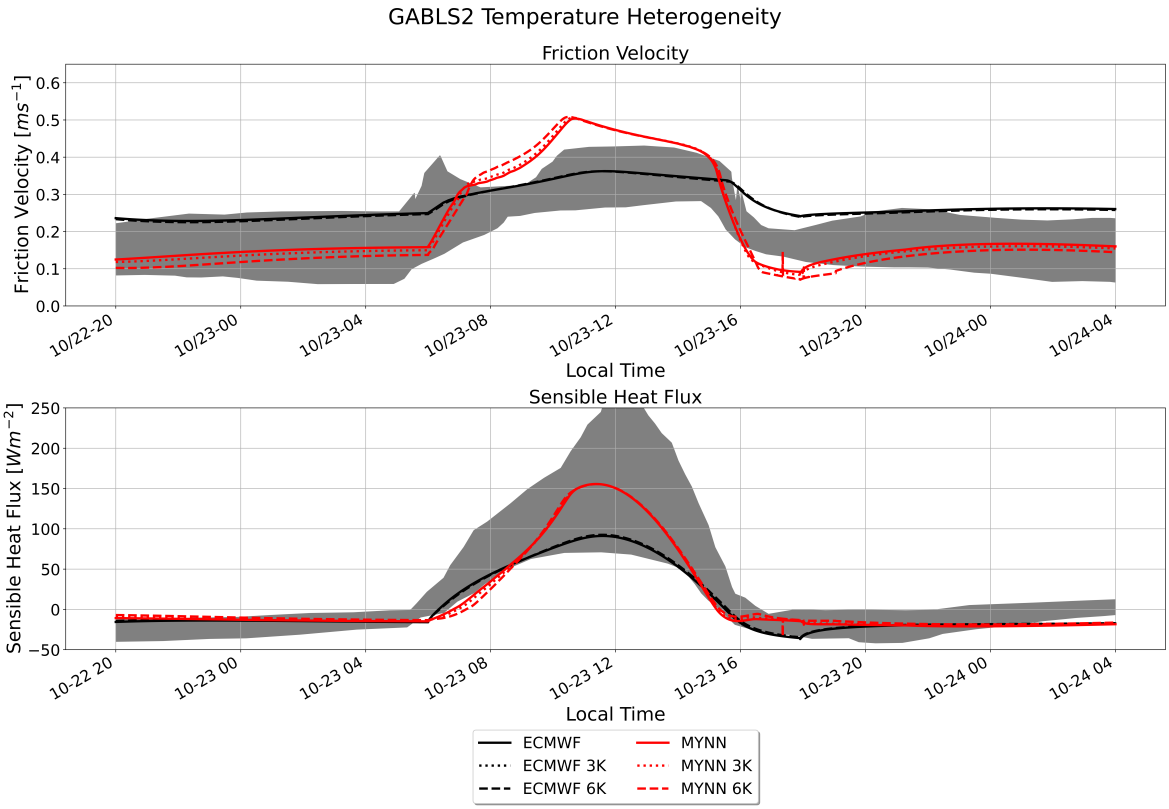

Figure 5.5: Time series of the friction velocity (top) and sensible heat flux (bottom) for the homogeneous case (solid), the TM with 3K patches (dotted), and 6K patches (dashed). The ECMWF model is colored black, the MYNN red, and the shaded grey represents the spread of the SCM models from GABLS2.

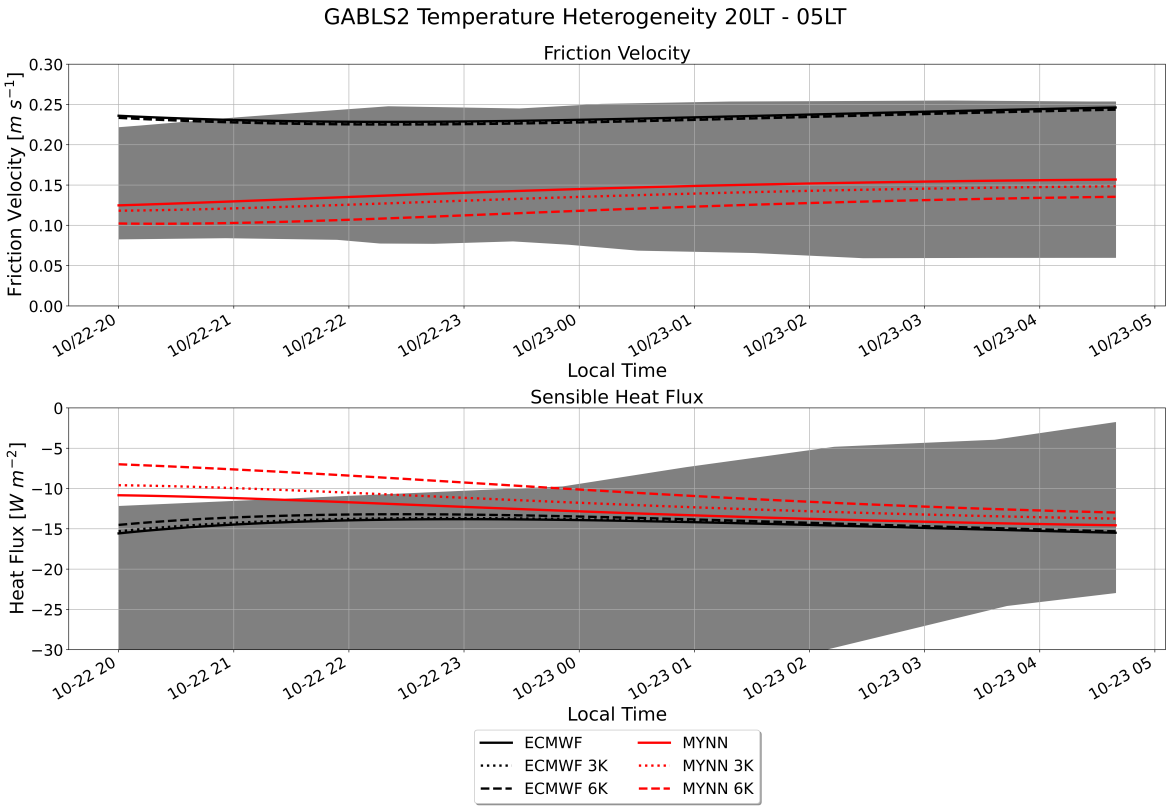

Figure 5.6: Time series of the friction velocity (top) and sensible heat flux (bottom) for the homogeneous case (solid), the TM with 3K patches (dotted), and 6K patches (dashed) focused on the period from 20 LT to 05 LT. The ECMWF model is colored black, the MYNN red, and the shaded grey represents the spread of the SCM models from GABLS2.

Using the MTM the friction velocity and sensible heat flux for the ECMWF and MYNN are between the values from the homogeneous case and the TM. Again this is the same trend that has been seen before in the previous analysis. There are some spikes in the modified version which might be an issue with some numerical instabilities, but the impacts stay thin an acceptable range.

The time series of TKE in the MYNN scheme is seen in Figures 5.9 and 5.10. To generate the time series of TKE, the mean TKE values in the lowest 50 m of the model

were used. The very small values of TKE are seen in the overnight hours with values less than $0.1\,\mathrm{m^2\,s^{-2}}$ and is on the edge of the spread from the SCMs. The TKE begins to increase as the diurnal heating begins and reaches a maximum of $1.30\,\mathrm{m^2\,s^{-2}}$ around 11 LT, about one hour before the peak in the SCMs from GABLS2. While the peak in MYNN is slightly earlier, the maximum value is comparable to the other SCMs. With the MTM, the values of TKE are again between the homogeneous and TM.

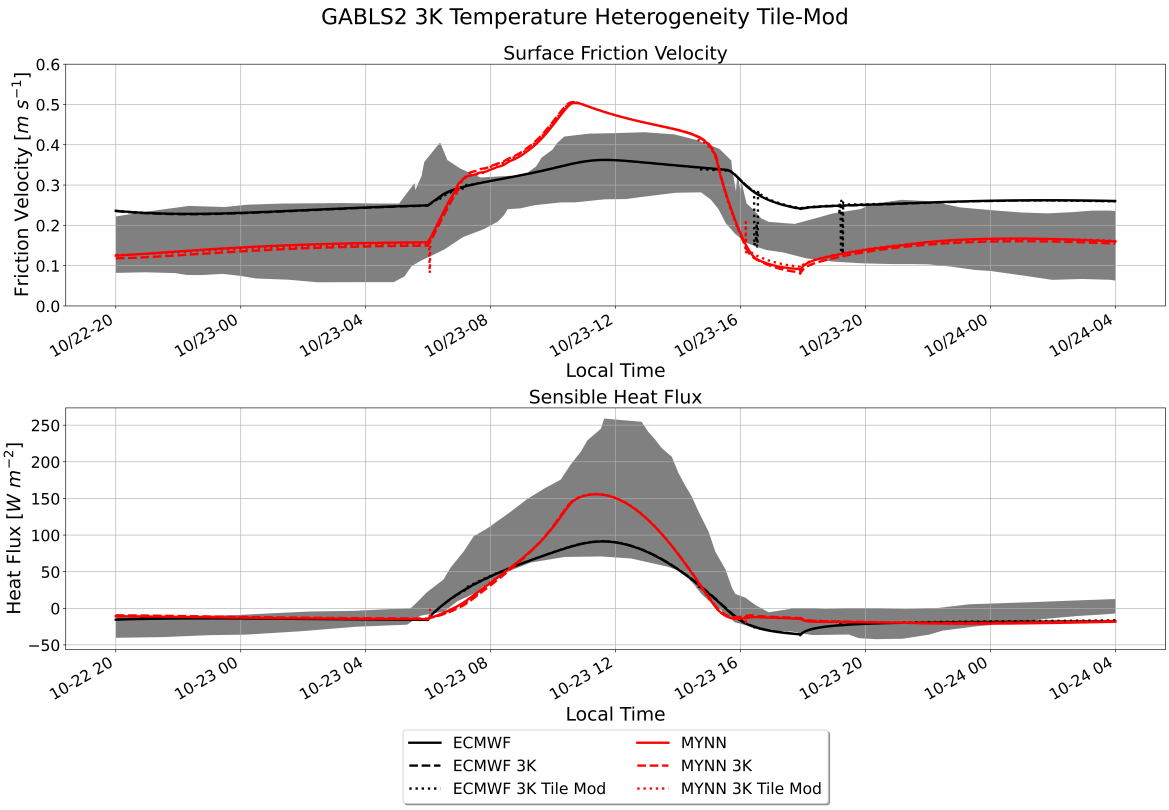

Figure 5.7: Time series of the friction velocity (top) and sensible heat flux (bottom) for the homogeneous case (solid), the TM with 3K patches (dashed), and the MTM with 3K patches (dotted). The ECMWF model is colored black, the MYNN red, and the shaded grey represents the spread of the SCM models from GABLS2.

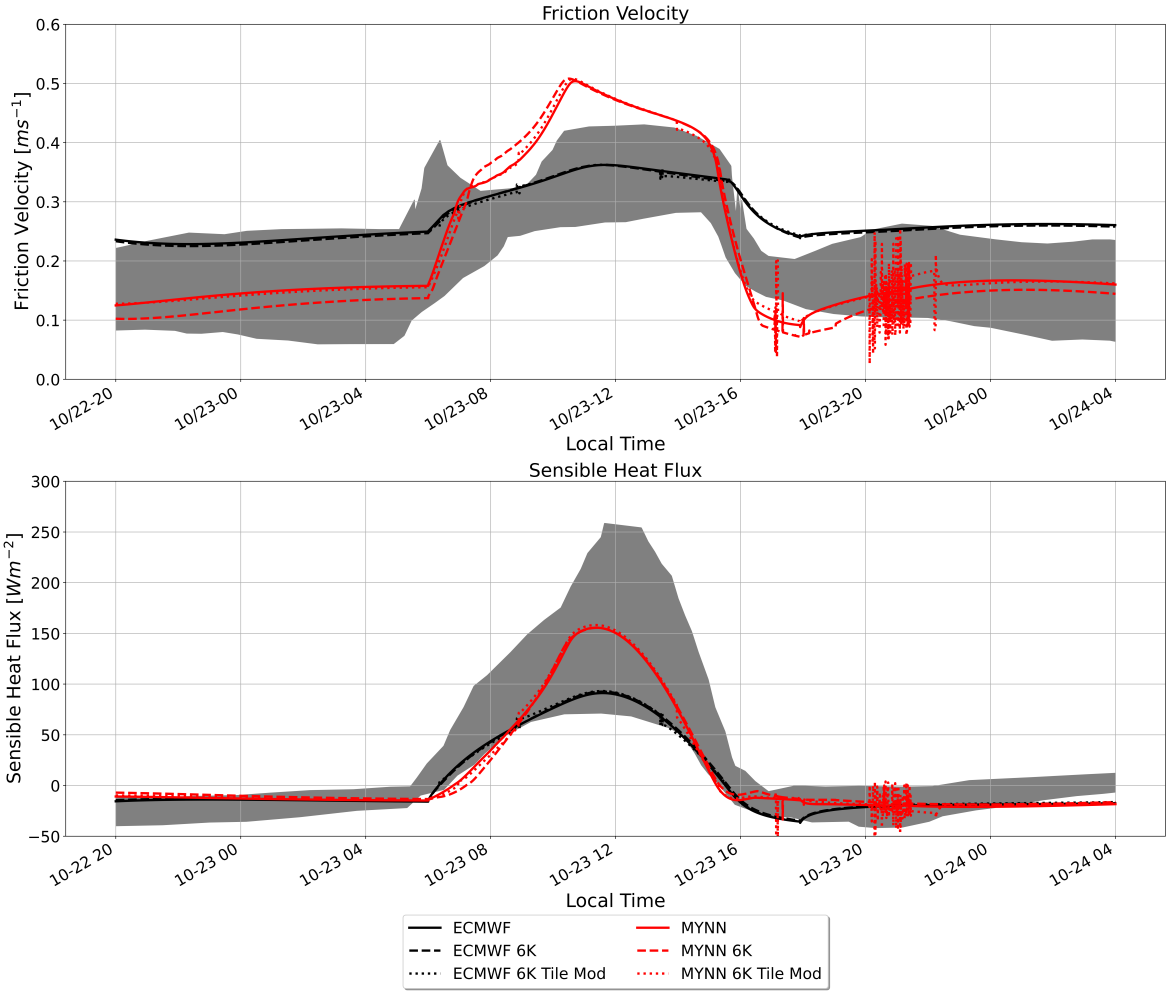

Figure 5.8: Time series of the friction velocity (top) and sensible heat flux (bottom) for the homogeneous case (solid), the TM with 6K patches (dashed), and the MTM with 6K patches (dotted). The ECMWF model is colored black, the MYNN red, and the shaded grey represents the spread of the SCM models from GABLS2.

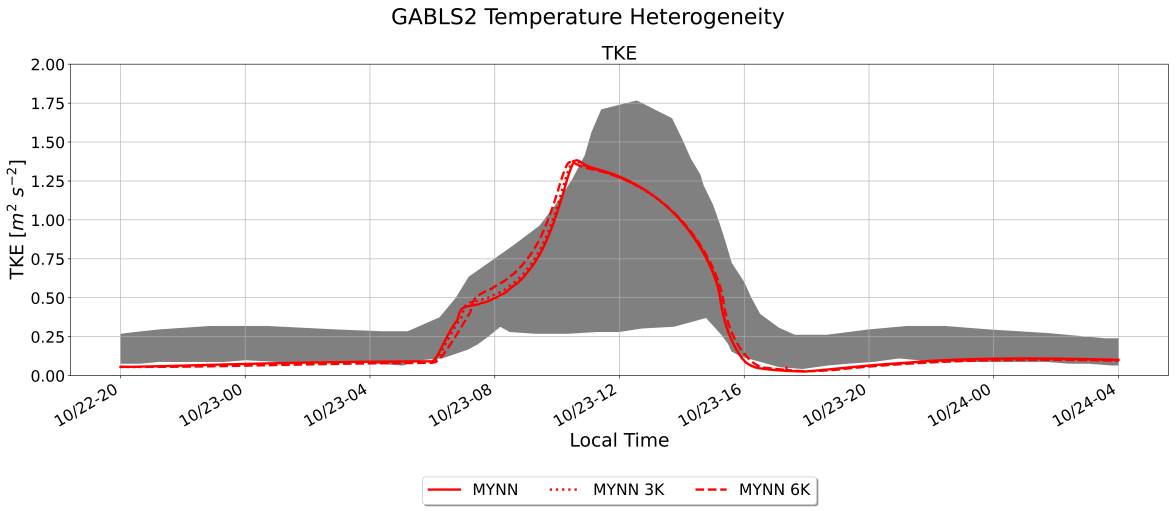

Figure 5.9: Time series of TKE for the homogeneous case (solid), the TM with 3K patches (dotted) and 6K patches (dashed). The shaded grey represents the spread of the SCM models from GABLS2.

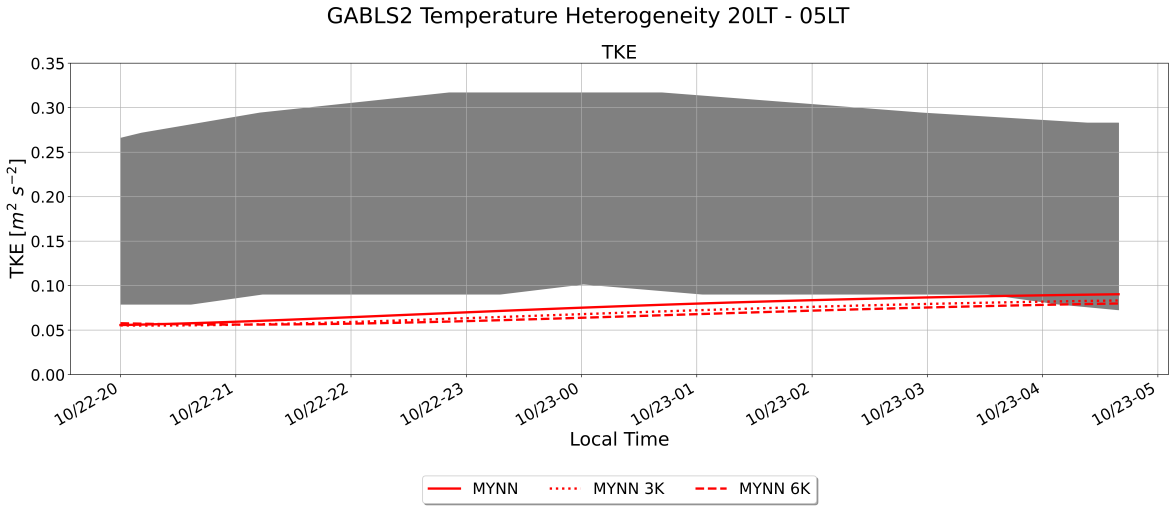

Figure 5.10: Same as above but focused on the period from 20 LT to 05 LT.

Simulation Runs					
Case	h [m]	L [m]	u_* [ms^{-1}]	$\langle w'\theta' \rangle$ [Kms^{-1}]	$\langle u'w' \rangle$ [m^{2}s^{-2}]
ECMWF	637.4	70.3	0.248	-0.016	0.061
ECMWF 3K	637.7	69.9	0.247	-0.016	0.061
ECMWF 6K	637.9	68.8	0.245	-0.015	0.061
ECMWF 6K Mod	637.1	70.2	0.247	-0.016	0.061
MYNN	71.7	19.3	0.157	-0.015	0.025
MYNN 3K	71.1	17.3	0.150	-0.014	0.023
MYNN 6K	81.2	14.0	0.136	-0.013	0.024
MYNN 6K Mod	72.6	19.0	0.155	-0.014	0.024

Table 5.1: Mean values during the hour prior to surface heating using surface temperature heterogeneity for the boundary layer height (h), Obukhov Length (L), friction velocity (u_*), surface heat flux ($\langle w'\theta' \rangle$) and surface momentum flux ($\langle u'w' \rangle$).

5.2.2 Vertical Profiles

In addition to the time series, vertical profiles are examined at different points in the diurnal cycle. First, vertical profiles of temperature and wind speed are analyzed at 05 local time, approximately one hour before surface heating begins (Figure 5.11). A strong potential temperature inversion is present at the very near surface that extends up to approximately 175 m. In the wind speed profile, the MYNN scheme develops

a LLJ approximately 150 m above the ground with a maximum of 10.5 $\mathrm{m\,s^{-1}}$. The ECMWF scheme has a more broad LLJ 800 m above the ground with a maximum of 10.0 $\mathrm{m\,s^{-1}}$. This behavior of the ECMWF having more mixing is similar to what was observed in the GABLS1 case.

With the 6K temperature patches, the surface temperatures are warmer than the homogeneous case by approximately 2.5 K. Even though this is a large difference, the height to which they decrease towards the neutral layer occurs at approximately the same height. Impacts from the temperature heterogeneity are confined to be in the lowest 200 m, or the extent of the stable boundary layer. The wind speed profiles from MYNN have slight differences, but the TM develop a stronger LLJ at a slightly higher height. In the ECMWF scheme there seems to be no distinguishable difference between the two plots.

With the MTM, similar results are found with a strong temperature gradient near the surface. The surface temperature lies between the homogeneous case and the TM, but is closer to the homogeneous case. By about $z = 175$ m each of the profiles have a constant value with height of $\theta = 286$ K. In the profiles of wind speed for the MYNN scheme, a LLJ is resolved at nearly the same height and strength as the homogeneous case. There are differences between the two though, as in the lowest 50 m the MTM is in between the homogeneous case and TM. In the ECMWF scheme, no visual differences were noted between the two.

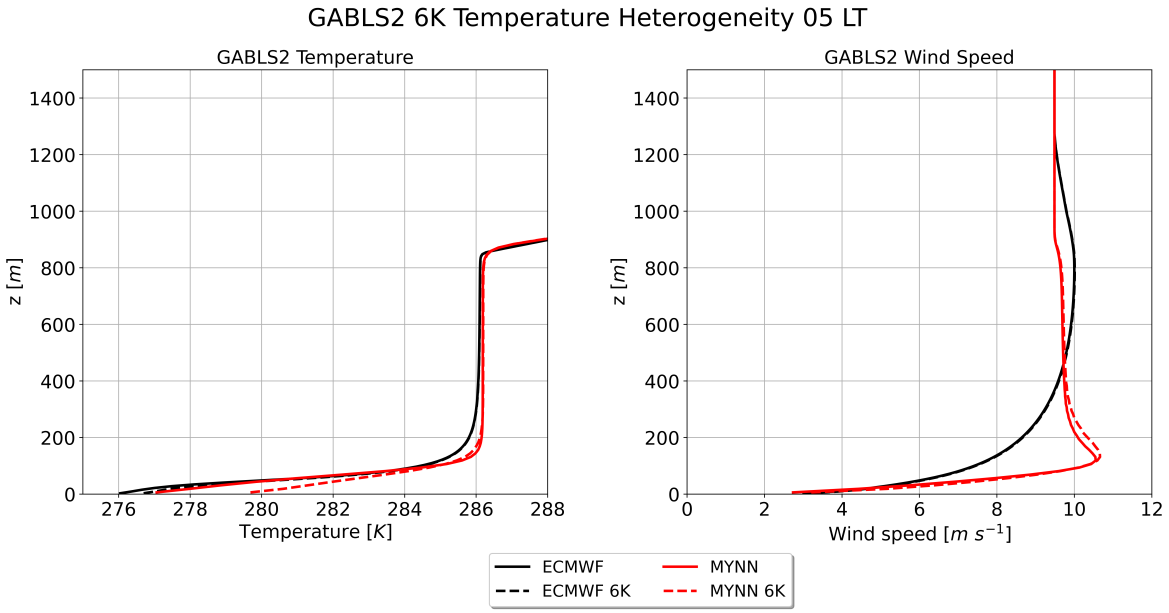

Figure 5.11: Vertical profiles of potential temperature (left) and wind speed (right) at 05 LT for the homogeneous case (solid), the TM with 6K patches (dashed). The ECMWF model is colored black, and the MYNN red. The shaded grey represents the spread of the SCM models from GABLS2.

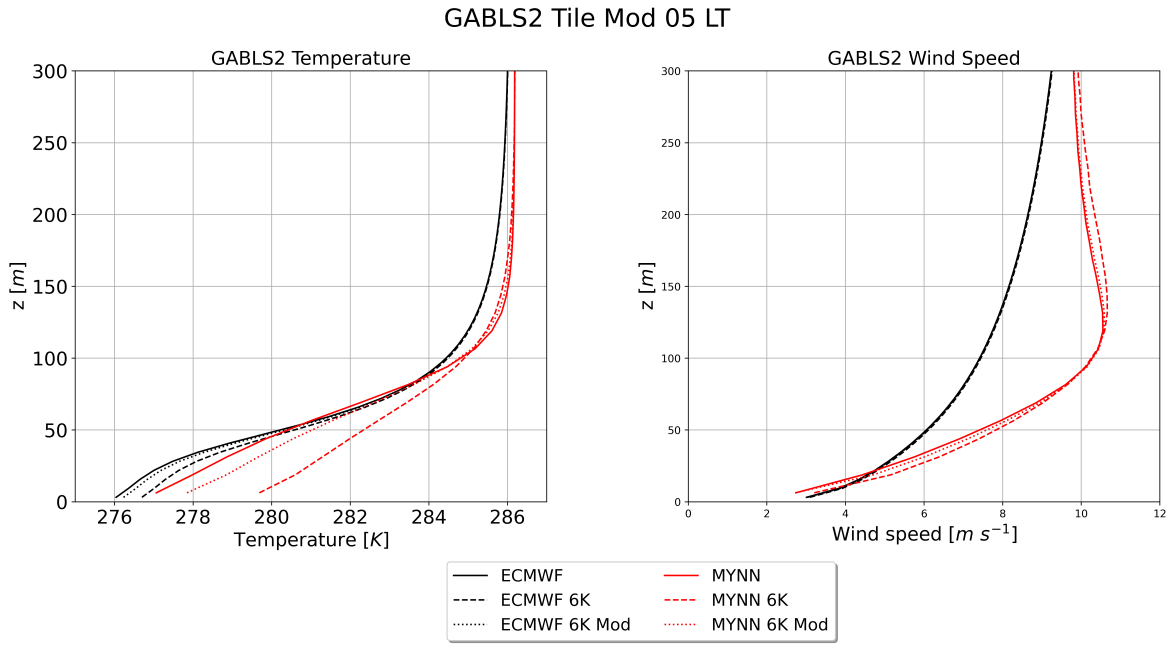

Figure 5.12: Vertical profiles of potential temperature (left) and wind speed (right) at 05 LT for the homogeneous case (solid), the TM with 6K patches (dashed), and the MTM with 6K patches (dotted). The ECMWF model is colored black, and the MYNN red. The shaded grey represents the spread of the SCM models from GABLS2.

Vertical profiles of temperature and wind speed are also analyzed at 14 LT during during convective conditions. The potential temperature profile of the MYNN scheme is characteristic of a well-mixed boundary layer, with nearly any change in potential temperature with height. The MYNN scheme is an outlier with the mean potential temperature profile 0.5 K warmer than the warmest SCM simulation. The inversion height in the MYNN scheme is also an outlier and is approximately 200 m higher than SCMs. The ECMWF inversion height has much better agreement with the SCM simulations, but has a sharp interface at the boundary layer height.

Both of the PBL schemes are within the spread of the SCM simulations for the wind speed profiles. The ECMWF is an outlier that has retained the LLJ structure

from the previous night. Instead of begin mixed out, the LLJ max has been modified and now has a strong jet that appears. The MYNN scheme is more representative of a typical boundary layer with near constant wind speeds with height in the boundary layer. The top of the inversion on the wind speed is approximately 150 m higher than the SCM simulations indication more mixing in the MYNN scheme.

The TM has very small changes in the profiles of potential temperature, with the heterogeneous case being slightly warmer by less than 0.001 K. This was also seen in the MTM which falls between the homogeneous case and TM. In the wind speed profiles, a similar behavior is seen with the homogeneous and TM overlapping one another throughout the entire profile. With the MTM, the curves for the wind speed overlap one another throughout the entire vertical profile.

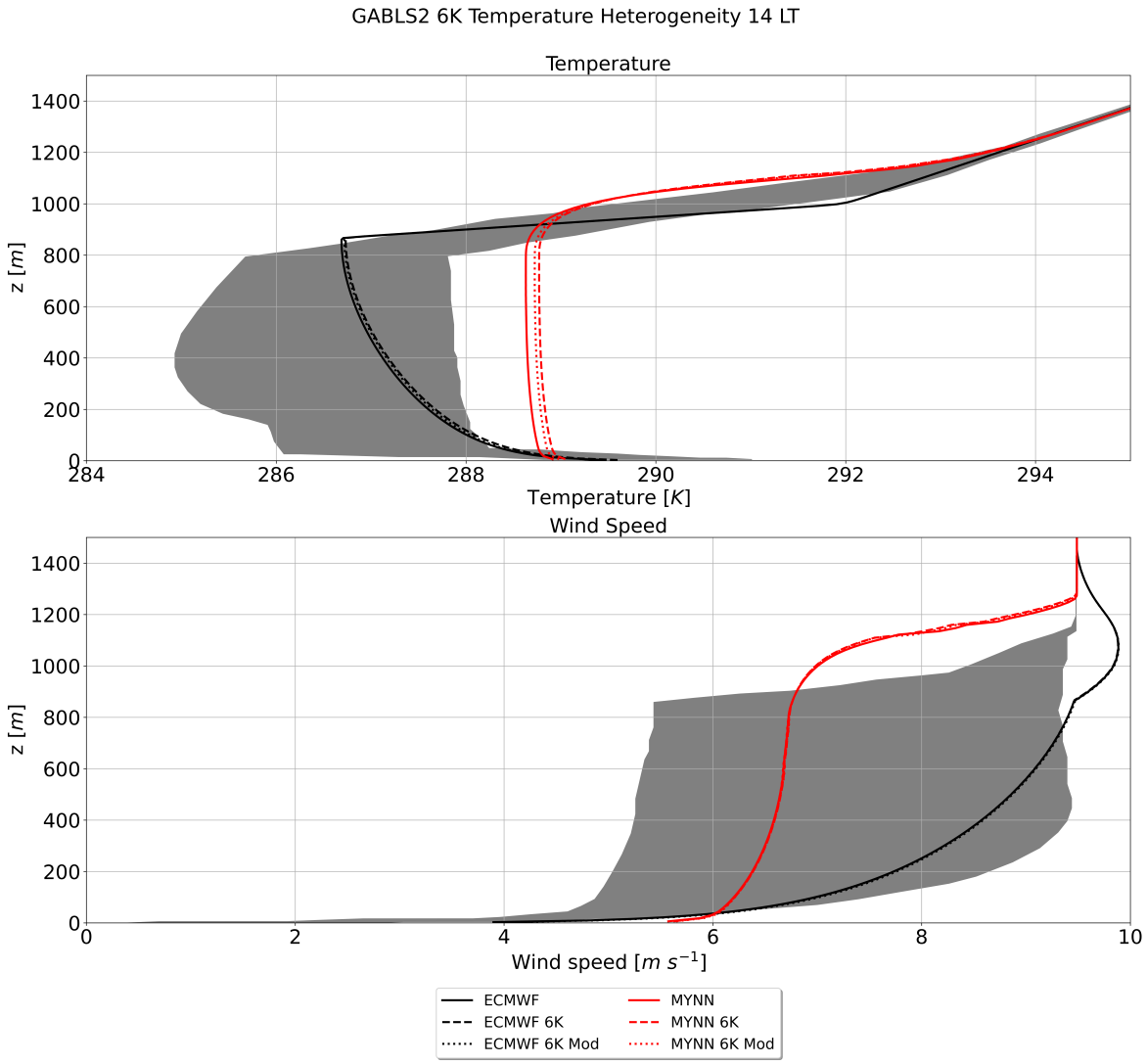

Figure 5.13: Vertical profiles of potential temperature (left) and wind speed (right) at 14 LT for the homogeneous case (solid), the TM with 6K patches (dashed), and the MTM with 6K patches (dotted). The ECMWF model is colored black, and the MYNN red. The shaded grey represents the spread of the SCM models from GABLS2.

The minimal differences between the homogeneous and surface temperature heterogeneity is expected here. During convective conditions, large turbulent eddies act to mix out the influence of surface heterogeneities. Therefore, any differences at the

surface get mixed out and the result is only very small changes. In the MYNN schemes, the difference in potential temperature in the neutral layer is less than .001K, and even smaller for the ECMWF scheme. The differences are most pronounced in the potential temperature profile since the heterogeneity is based in the temperature field. With the MTM, again only very small differences were noted due to the convective conditions. The most pronounced differences are the changes in potential temperature field for the MYNN scheme, but the trend of being between the homogeneous case and TM simulation is found here again.

The vertical profiles of TKE are also examined at 14 LT for the MYNN scheme to understand how the TKE based scheme compares to other TKE based SCM models (Figure 5.14). The MYNN scheme increases from a value of $0.8\,\mathrm{m^2\,s^{-2}}$ at the surface to a max of $1.3\,\mathrm{m^2\,s^{-2}}$ at approximately 250 m. This is well within the spread of the SCM simulations which range from a surface value of $0.25\,\mathrm{m^2\,s^{-2}}$ to $1.75\,\mathrm{m^2\,s^{-2}}$. The height at which the TKE begins to rapidly decrease at 850 m is at the upper end of the SCM simulations, and also decrease to zero at approximately the same height of 1200 m. The magnitude of the TKE is larger in convective conditions since the fluxes are larger than in stable conditions. With the MTM, almost no change is noted during convective conditions. This was expected due to the previous results and that we expect that during convective conditions the effects of the surface heterogeneity are blended out. Even more so, using the MTM almost no distinguishable differences were able to be found visually.

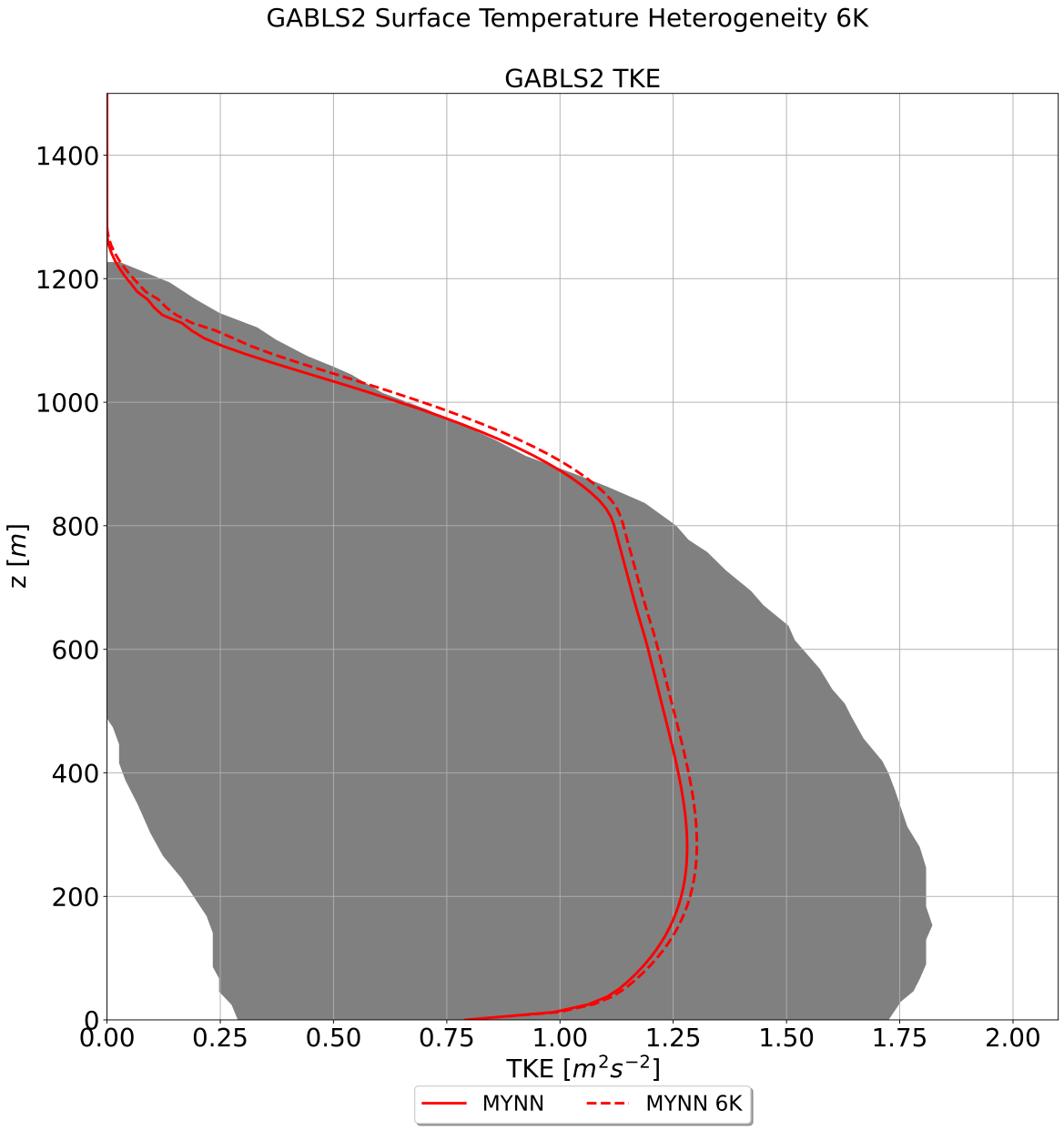

Figure 5.14: Vertical profile of TKE at 14 LT for the MYNN (red) and MYNN 6K (dashed red) cases. The shaded grey represents the spread of the SCM models from GABLS2.

5.3 Roughness Differences

Differences in roughness were also examined for the GABLS2 case. The surface roughness heterogeneity was defined by using two different patches with different surface roughness values for z_{0m}. One patch was kept constant at $z_{0m} = 0.03\,\mathrm{m}$, the same value prescribed in GABLS2, while the other was varied from $z_{0m} = 0.3\,\mathrm{m}$ to $z_{0m} = 0.0003\,\mathrm{m}$. The values for z_{0h} were defined similarly but are taken to be $z_{0h} = z_{0m}/10$. The boundary layer height (h), Obukhov Length (L), friction velocity (u_*), surface heat flux ($\langle w\theta \rangle$) and surface momentum flux ($\langle uw \rangle$) are examined in Table 6.2. The mean values were computed by taking the mean one hour prior to the beginning of the increase in surface temperature. It is clear that the cases with larger z_0 values had larger surface fluxes and were less stable.

Time series analysis of different roughness values were examined over the simulation period for surface roughness values that range from $z_0 = 0.3\,\mathrm{m}$ to $z_0 = 0.0003\,\mathrm{m}$. It is clear that with the decreasing surface roughness values, the surface temperatures are warmer during the nighttime. In addition to being warmer these simulations also had an increase in the wind speed. This agrees with the sensible heat flux time series in Figure 5.15 where the simulation runs with lower effective roughness had smaller-in-magnitude values. From Table 5.2, there was also an increase in the Obukhov length as the effective surface roughness length decreased, leading towards more stable conditions.

During the daytime during convective conditions, difference continue between the different simulations. The smaller surface roughness simulations continue to have the warmest surface temperature and the strongest wind speeds. This differs from the use of surface temperature heterogeneity where the all of the heterogeneous cases were equivalent to the homogeneous conditions.

Simulation Runs, $z_{01} = 0.03\,\mathrm{m}$						
Case	z_{0e} [m]	h [m]	L [m]	u_* [ms^{-1}]	$\langle w'\theta' \rangle$ [Kms^{-1}]	$\langle u'w' \rangle$[$\mathrm{m}^2\mathrm{s}^{-2}$]
ECWMF $z_{02} = 0.3\,\mathrm{m}$	0.1602	695.6	83.2	0.277	-0.018	0.077
ECMWF	0.03	637.4	70.3	0.248	-0.016	0.061
ECWMF $z_{02} = 0.0003\,\mathrm{m}$	0.010	601.7	63.4	0.231	-0.014	0.054
MYNN $z_{02} = 0.3\,\mathrm{m}$	0.1602	77.7	20.4	0.164	-0.016	0.027
MYNN	0.03	71.7	19.3	0.157	-0.015	0.025
MYNN $z_{02} = 0.0003\,\mathrm{m}$	0.010	64.1	17.7	0.148	-0.0132	0.022

Table 5.2: Mean values during the hour prior to surface heating using z_0 heterogeneity for the effective roughness length (z_{0e}), boundary layer height (h), Obukhov Length (L), friction velocity (u_*), surface heat flux ($\langle w'\theta' \rangle$) and surface momentum flux ($\langle u'w' \rangle$). Here z_{01} is the roughness length for patch 1, and z_{02} for patch 2.

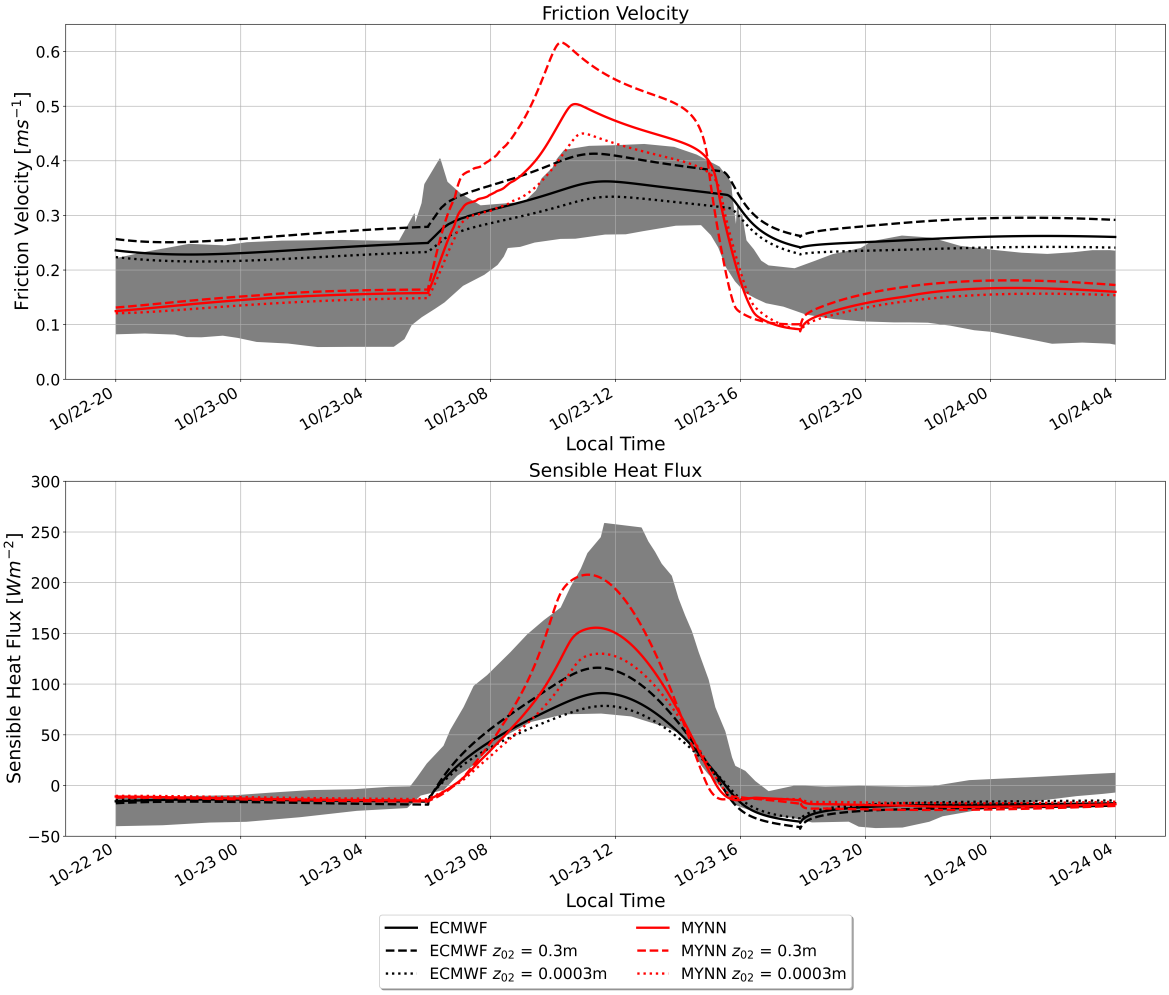

Figure 5.15: Time series of the friction velocity (top) and sensible heat flux (bottom) with the homogeneous case (solid) and surface heterogeneity for patch values of $z_0 = 0.3\,\mathrm{m}$ (dashed) and $z_0 = 0.0003\,\mathrm{m}$ (dotted). The ECMWF model is colored black, the MYNN red, and the shaded grey represents the spread of the SCM models from GABLS2.

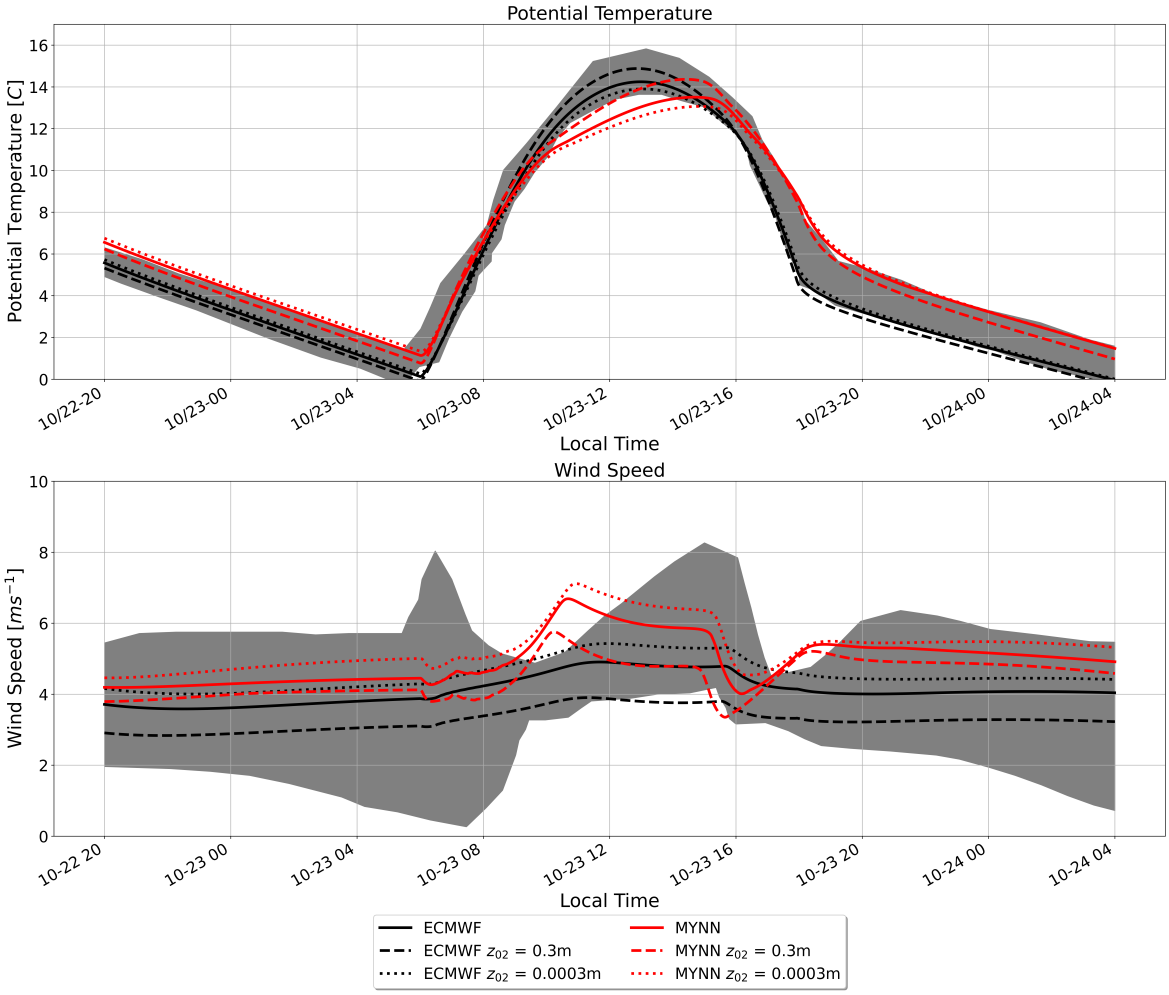

Figure 5.16: Time series of the potential temperature (top) and wind speed (bottom) with the homogeneous case (solid) and surface heterogeneity for patch values of $z_0 =$ 0.3 m (dashed) and $z_0 = 0.0003$ m (dotted). The ECMWF model is colored black, the MYNN red, and the shaded grey represents the spread of the SCM models from GABLS2.

The vertical profiles have larger differences during the convective conditions at 14 LT. The differences between the profiles for the MYNN scheme cover a range of over 1.5 K. The wide range is due to the strong impact the surface roughness has on modulating the amount of mixing in the model. The surface roughness also has

an impact on the temperature profiles by increase the inversion height with the most rough case for each PBL scheme.

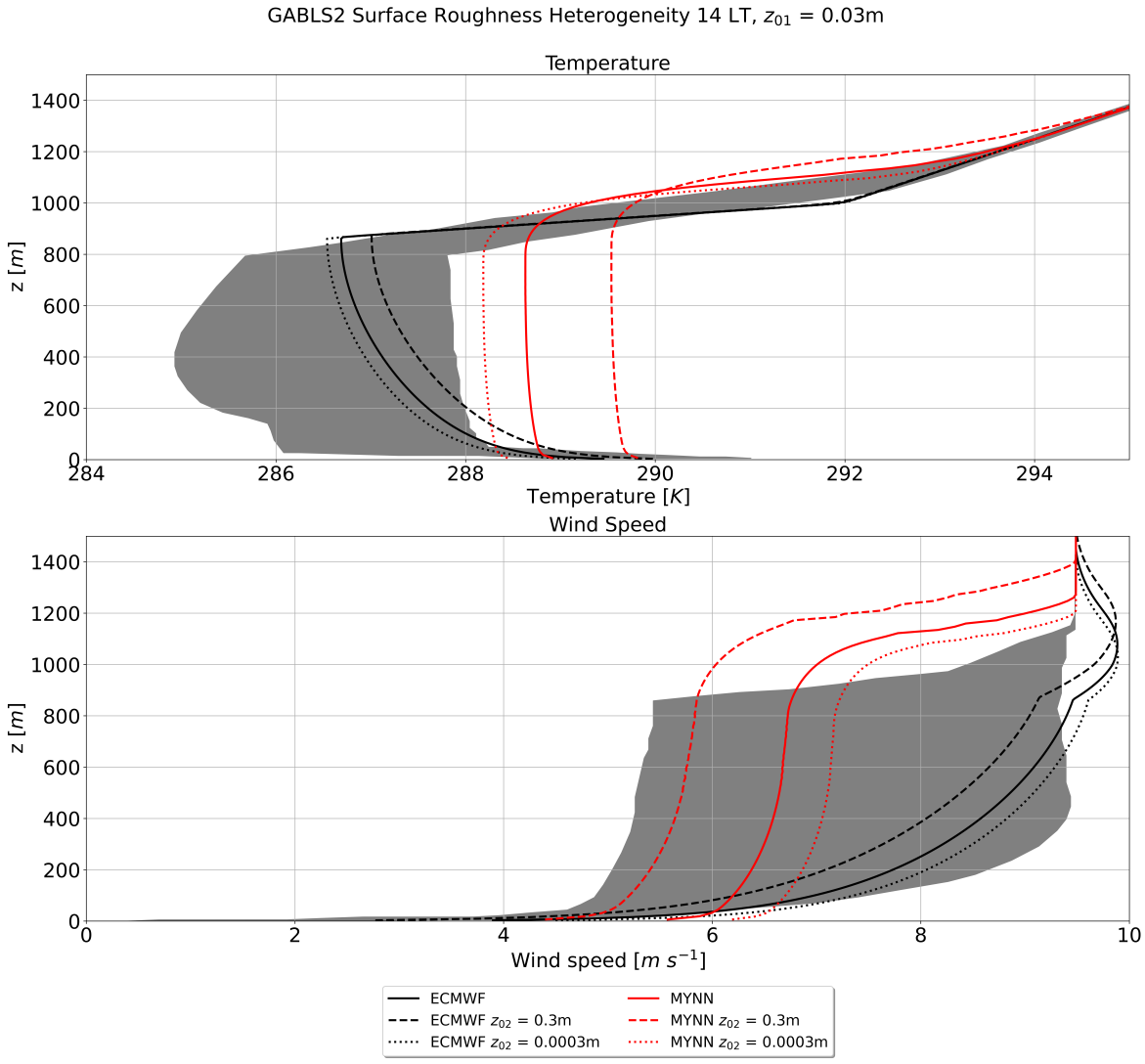

Figure 5.17: Vertical profiles of wind speed (left) and potential temperature (right) at 14 LT with the homogeneous case (solid) and surface heterogeneity for patch values of $z_0 = 0.3\,\mathrm{m}$ (dashed) and $z_0 = 0.0003\,\mathrm{m}$ (dotted). The ECMWF model is colored black, and the MYNN red.

5.4 Discussion

The SCM simulations of the two PBL schemes investigated performed well and the results were in line with other SCMs used in Svensson et al. (2011). The MYNN was on the warmer edge of the SCM simulations during the nighttime hours while the ECMWF was nearly in the center of the spread. During the day time the ECMWF continues to perform just as well with the peak temperature of 14.5 °C in line with other simulations. The MYNN lagged behind the ECMWF and obtains a lower maximum of 14 °C two hours later. Into the second night similar behavior from the first night is seen with the MYNN scheme slightly on the warm edge of the SCM simulations, while the ECMWF is not on the cool side.

With the addition of the temperature heterogeneity, the surface temperature during the nighttime were warmer, especially with the 6K temperature difference. The MYNN scheme stands out among the other schemes by being 3 °C warmer than the homogeneous case. This is likely due to the warmer patch dominating the surface heat flux estimation, resulting in a bias towards the warm patch. With the MTM, we see this problem is corrected with the additional treatments for stability over the stable patch. The resulting fluxes are slightly smaller in magnitude, but not to the degree of the TM, resulting in a lower surface temperature. This further shows the improvements made with the surface heat flux estimation using the MTM.

The surface roughness heterogeneity has significant impacts on the mean profiles in both stable and unstable conditions. With the lower surface roughness values used, the fluxes at the surface decreased leading to smaller momentum and heat fluxes at the surface. This was true for both stable and unstable conditions. This trend is further seen by increasing the surface roughness value to $z_0 = 0.3\,\mathrm{m}$, larger than the constant

patch value of $z_0 = 0.03\,\mathrm{m}$. The result of larger-in-magnitude surface fluxes is what would be expected with larger surface roughness values.

Chapter 6

Validation of SCM against BLISSFUL

The Boundary Layer Integrated Sensing and Simulation (BLISS) group at the University of Oklahoma held the Boundary Layer Integrated Sensing and Simulation Field Universalization Laboratory (BLISSFUL) experiment during the summer of 2021 at Kessler Ecological and Atmospheric Fields Station (KAEFS) located at (35.236110°, -97.464880°). During this time, state-of-the-art boundary layer sensing instruments were deployed including a Doppler LIDAR, microwave radiometer (MWR), and atmospheric emittance radiance interferometer (AERI). Also integrated was the UAS coptersonde that recorded vertical temperature and wind profiles as well as the low energy meteorological stations (LEMS) from University of Utah (Gunawardena et al. 2018) to record surface temperature. Unique to this case was the contributions from the author to collect part of the dataset, by launching weather balloon soundings and deploying the LEMS at different locations at KAEFS.

6.1 Introduction

The data from BLISSFUL is from July 6th and July 7th, 2021 at KAEFS. Using the data from the numerous observation tools available, initial conditions for the SCM were set. These initial conditions came from soundings, the Doppler LIDAR, the LEMS, and the AERI. The results were then compared to observations these same observations for validation of the SCM.

The synoptic conditions of July 6th, 2021 were typical of mid-summer in central Oklahoma. The daytime had highs in the mid 90 °Fs, with isolated thunderstorms developing throughout the day with the well mixed convective boundary layer. Ideal conditions for a transition period to a nocturnal boundary layer are clear skies with small influences from mesoscale features. On this day dying thunderstorms produced outflow boundaries that contaminated the transition period around 00Z July 7th. This is seen in the time series of surface temperature in both the LEMS and mesonet station in Figure 6.2.

There were two soundings that were available near the simulation time that enabled the calculation of the large-scale forcing from observation. The two balloon launches at 20:30Z July 6th and 10:00Z July 7th are from the same site at KAEFS where the LIDAR, coptersonde, and LEMS observations are located. With these two soundings, the wind speed was given every second by linearly interpolating between the two soundings. To determine the geostrophic wind, a similar methodology to that used in the GABLS2 case was used where the wind speed at every second in the $3\,\mathrm{km} - 4\,\mathrm{km}$ layer was averaged.

Another method was used to force the model, using a nudging procedure to influence the predicted variables u, v and θ based on real observation as described in Chapter 3. The observations for the nudging procedure were used from the LIDAR and AERI in CLAMPS. Both of these platforms have high temporal and vertical resolution in the lower boundary layer and make for an obvious choice to use in the nudging procedure.

Figure 6.1: Dr. Jeremy Gibbs, Dr. Elizabeth Smith, Dr. Tyler Bell, and author at the LEMS 03 location.

The LEMS were deployed across KAEFS, with a photo of the equipment shown in Figure 6.1. The LEMS return surface heat, moisture, wind speeds, soil moisture and temperature at each location and are then saved to a SD card. The five locations were chosen to get as large of an area of KAEFS sampled as possible. LEMS 4 was located in close proximity to the Washington mesonet station which is a well maintained by the Oklahoma Mesonet seen in Figure 6.4 (Brock et al. 1995; Crawford et al. 2007). This allowed for comparison of the observations from the LEMS to the Washington Mesonet site for verification of the LEMS data.

From Figure 6.2 and 6.3 it is evident the surface potential temperature in the LEMS is biased approximately $2\,\mathrm{K} - 3\,\mathrm{K}$ higher than the mesonet station during the day. This is likely a result of the temperature sensor not being aspirated and resulting in too warm of temperatures. The LEMS reaches a peak approximately two hours before the mesonet, but both suddenly drop to the same value at 23 UTC. This sudden drop was associated with an outflow boundary from dying thunderstorms in the area of KAEFS. After the outflow passage, the LEMS and Mesonet are in much better agreement than before with differences in potential temperature of less than $0.5\,\mathrm{K}$. The dying thunderstorm outflow boundaries would also influence the complex wind profiles that are observed, making the geostrophic forcing difficult to determine. With this in mind, the nudging procedure was used in order influence the simulations towards the observations.

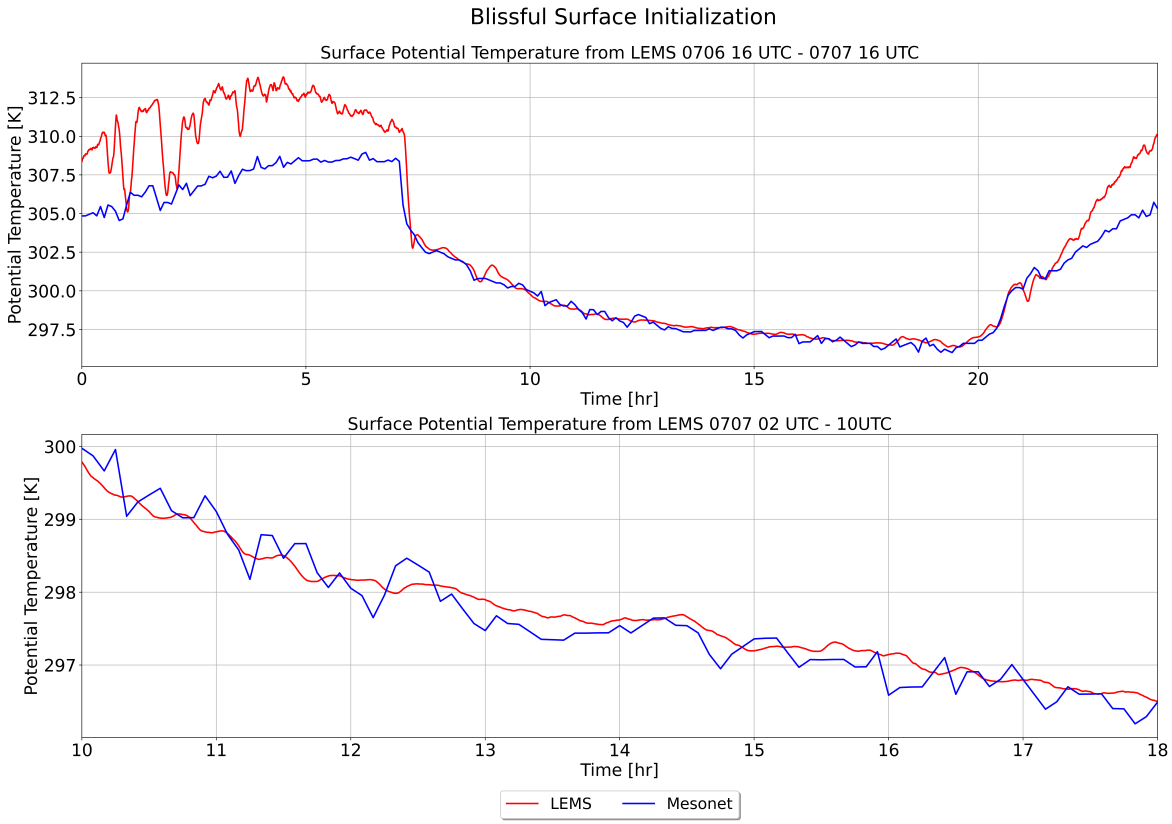

Figure 6.2: Surface potential temperature from the LEMS (red) and the Washington mesonet site (blue) from July 6, 16 UTC to July 7, 16 UTC (top) and the focused period during the simulation from July 7, 02 UTC to July 7, 10 UTC (bottom).

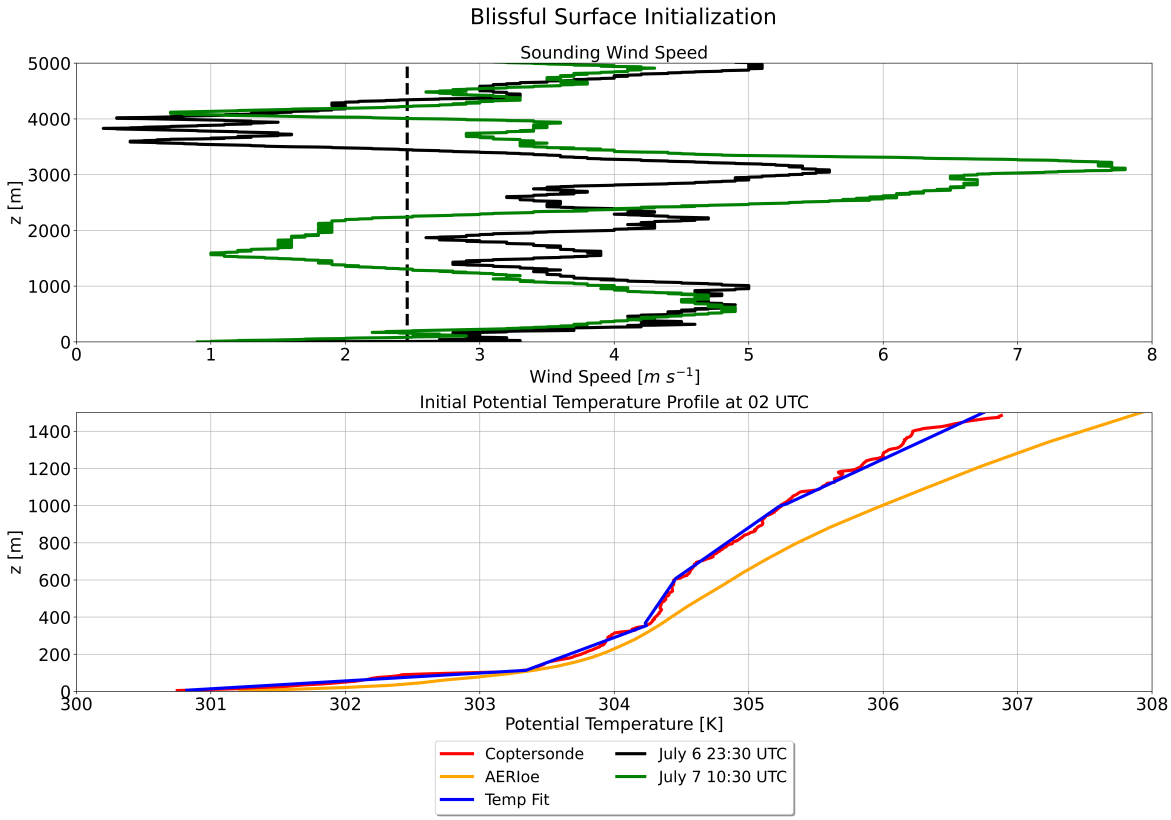

Figure 6.3: Vertical profiles of the two different soundings of wind speed on the top are shown at July 6, 23:30 UTC (black) and July 7, 10:30 UTC (green) and the forcing used in the simulations (dashed black). On the bottom is the initial profiles of potential temperature from the AERI (orange) and coptersonde (red) at July 7, 02 UTC and the initial profile used in the model (blue).

From the analysis of the two observations above, the surface temperatures for the simulation was determined by using the surface temperature data from the LEMS 4. This was the LEMS that was located next to the mesonet station, and the CLAMPS and coptersonde launch points. An important note here is that a 5-minute running mean was applied to the raw data from the LEMS, and then linear interpolation was used between each period to get the surface temperature at every second in time.

Initial profiles of temperature were set by fitting a series of linear lines to the vertical profile of potential temperature from the 02Z coptersonde launch. The vertical profile of the coptersonde, AERI, and the best fit lines of potential temperature are shown in Figure 6.3. A very shallow and strong inversion is present with lapse rates in the lowest 100 m approaching $25\,\mathrm{K\,km^{-1}}$. Above this level the profile is still stable, but with weaker lapse rates ranging from $1\,\mathrm{K\,km^{-1}}$ to $4\,\mathrm{K\,km^{-1}}$.

Since CLAMPS1 and CLAMPS2 were both located within proximity to each other ($\approx 100\,\mathrm{m}$) and had similar land-surface types at each site. The initial profile of TKE was generated by using the vertical stares of w from CLAMPS2 and u, v components from CLAMPS1. Since the vertical stares have much higher temporal frequency ($\approx 0.25\,\mathrm{s}$) than the VADs ($\approx 35\,\mathrm{s}$), the vertical velocity was averaged over a 5-minute period at 02Z to generate the initial TKE profile up to 1500 m. The data is noisy at the upper limit due to loss of scatterers in the free atmosphere, so the TKE profile had to be truncated to a limit. Above this truncation limit the TKE was set to a minimum value of $0.1\,\mathrm{m^2\,s^{-2}}$, similar to what was done in the setup for GABLS2.

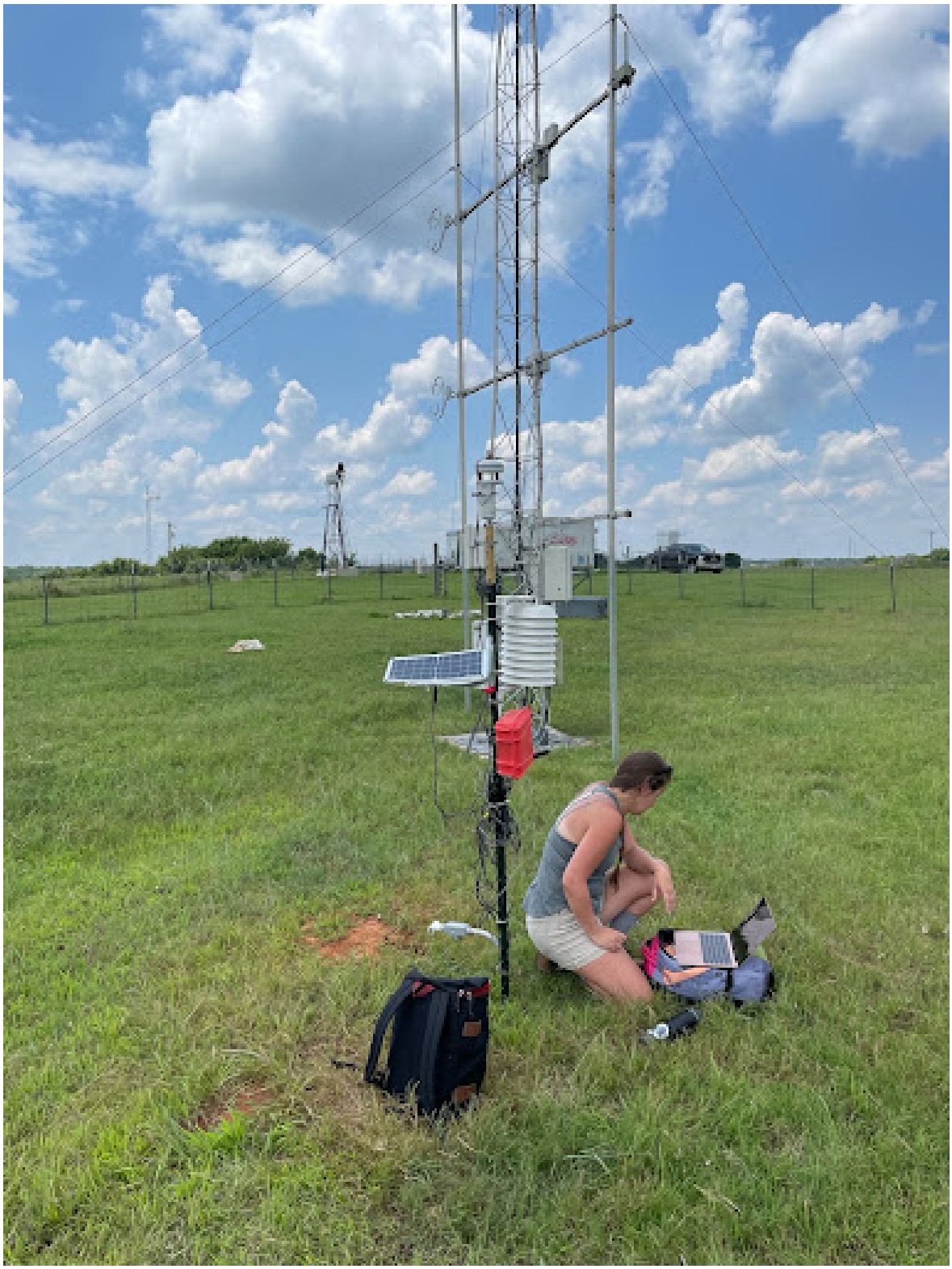

Figure 6.4: LEMS 04 location next to the Washington Mesonet site with Dr. Elizabeth Smith pictured.

6.2 Results

6.2.1 Vertical Profiles

The vertical profiles of potential temperature show a very sharp inversion near the surface in all three PBL schemes due to the very strong cooling taking place at the surface (Figures 6.5 and 6.6. The PBL schemes do not have enough cooling aloft and are warmer than the observations from the coptersonde and AERI retrievals. The wind profiles show almost no change from the initial conditions with a constant wind with height from 100 m to 1500 m. Compared to the observations from the coptersonde and LIDAR, all three PBL schemes perform poorly and do not resolve the LLJ that occurs at around 800 m.

Using the nudging procedure (Eq. 3.5) available in the SCM, significant improvements were made to the wind profiles in all three PBL schemes. Each PBL scheme is able to simulate the key profile features from the LIDAR observations including a sharp wind maximum very near to the surface at 150 m as well as the LLJ feature at approximately 800 m. The MYJ and MYNN schemes lie exactly on top of one another up to 1100 m before diverging.

The profile of the fluxes reveal some of the behavior seen in the profiles of wind speed and temperature (Figures 6.7 and 6.8. With no nudging, the MYJ and MYNN both have a smooth decreasing profile of the kinematic momentum flux that obtains a minimum of zero around 100 m, with the ECMWF slightly higher in height at 250 m. With the nudging profile there is a sharp spike that occurs in the MYJ and MYNN schemes around 100 m, then begins to decrease to zero. The MYNN scheme decreases all the way to zero, while the MYJ scheme still has a slightly positive value. Near the top of the model domain at 1200 m, the MYJ and MYNN schemes both show a

very large spike in the kinematic momentum flux. With the nudging procedure, the ECMWF scheme had bad values that did not agree with the rest of the schemes.

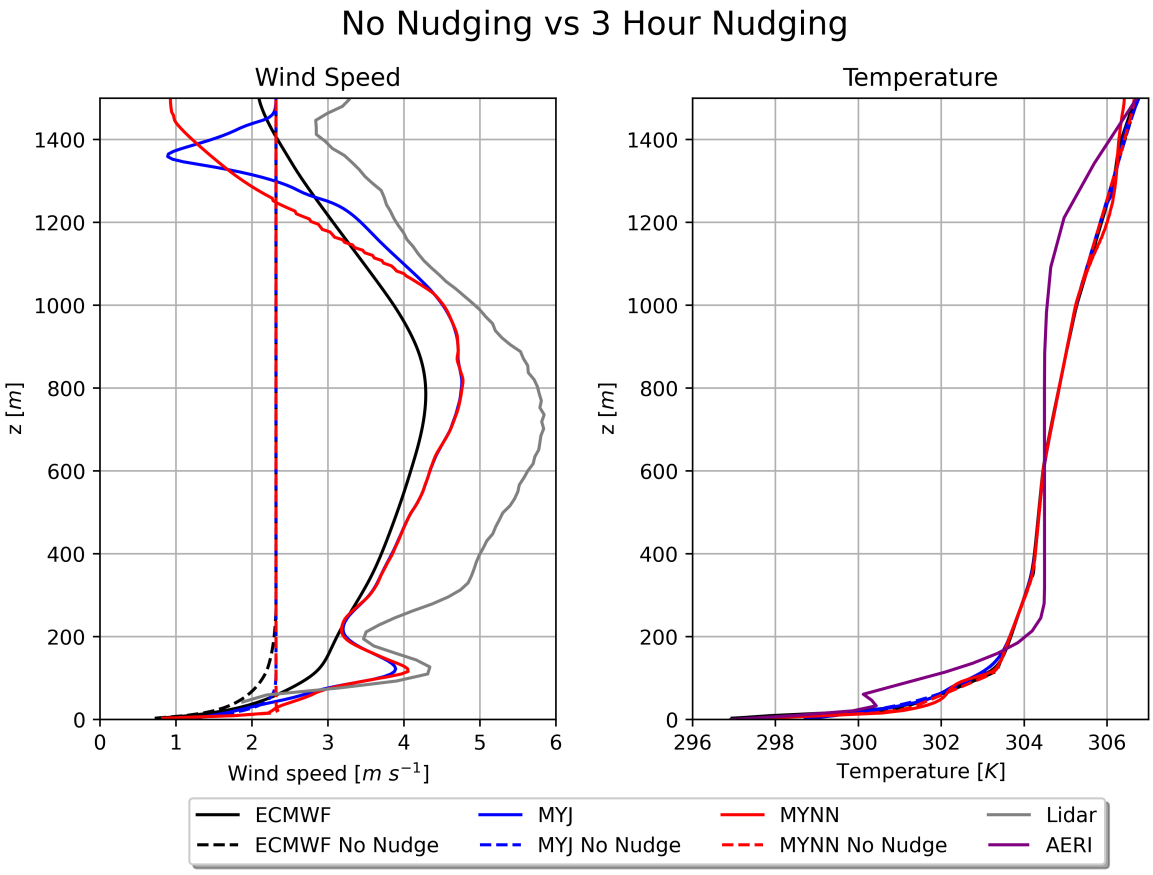

Figure 6.5: Vertical profiles of wind speed (left) and potential temperature (right) averaged over the final hour of the simulation using no nudging (dashed) and nudging (solid). The ECMWF model is colored black, the MYJ blue, and the MYNN red along with observations from the Doppler Lidar (grey) and retrievals from the AERI (dark purple).

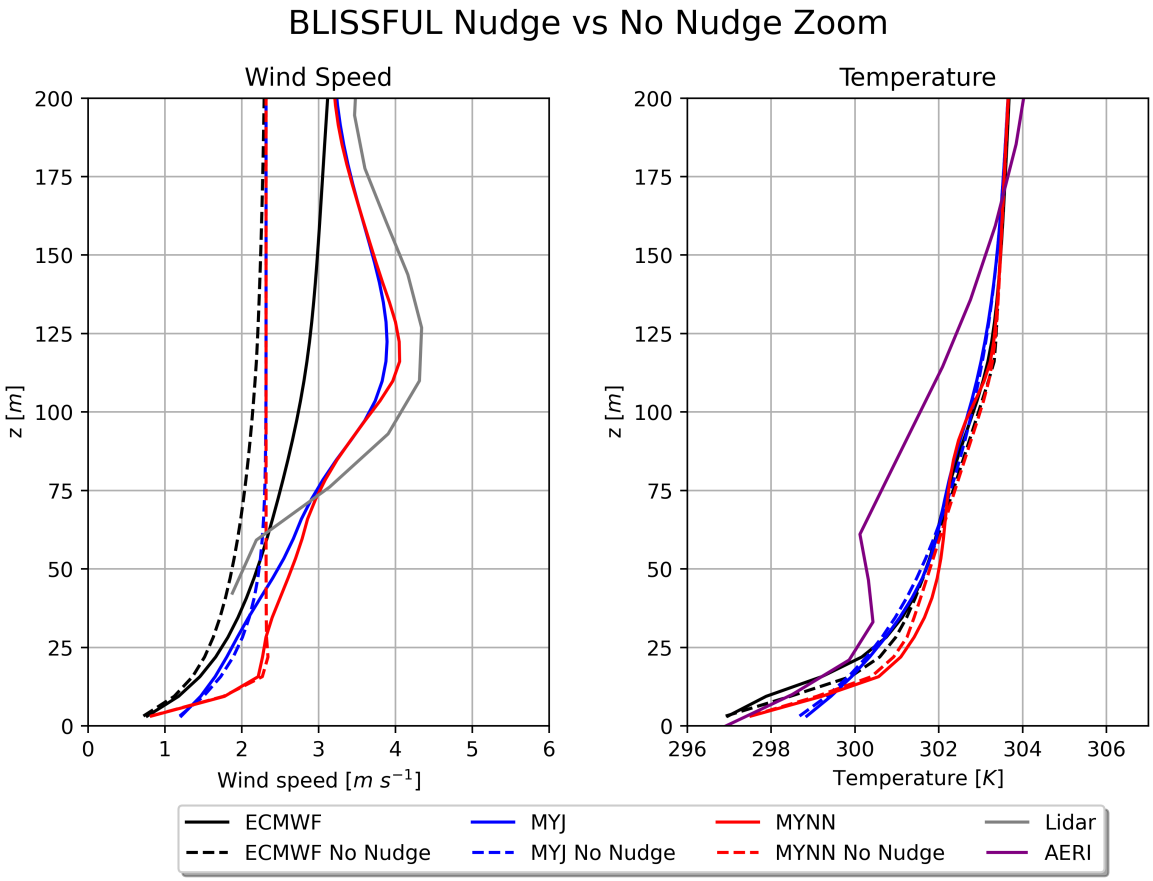

Figure 6.6: Same as previous but the vertical axis has changed to $z \in [0, 200]$.

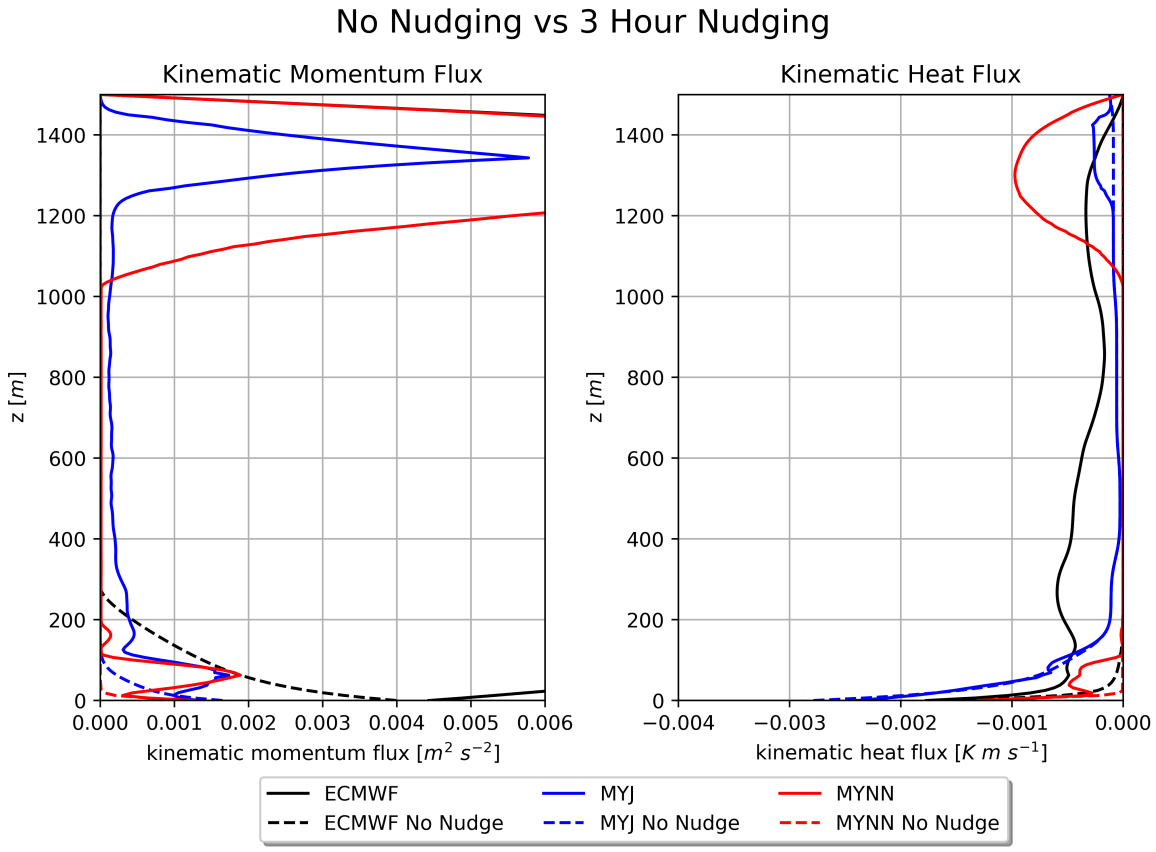

Figure 6.7: Vertical profiles of the kinematic momentum flux (left) and kinematic heat flux (right) averaged over the final hour of the simulation using no nudging (dashed) and nudging (solid). The ECMWF model is colored black, the MYJ blue, and the MYNN red.

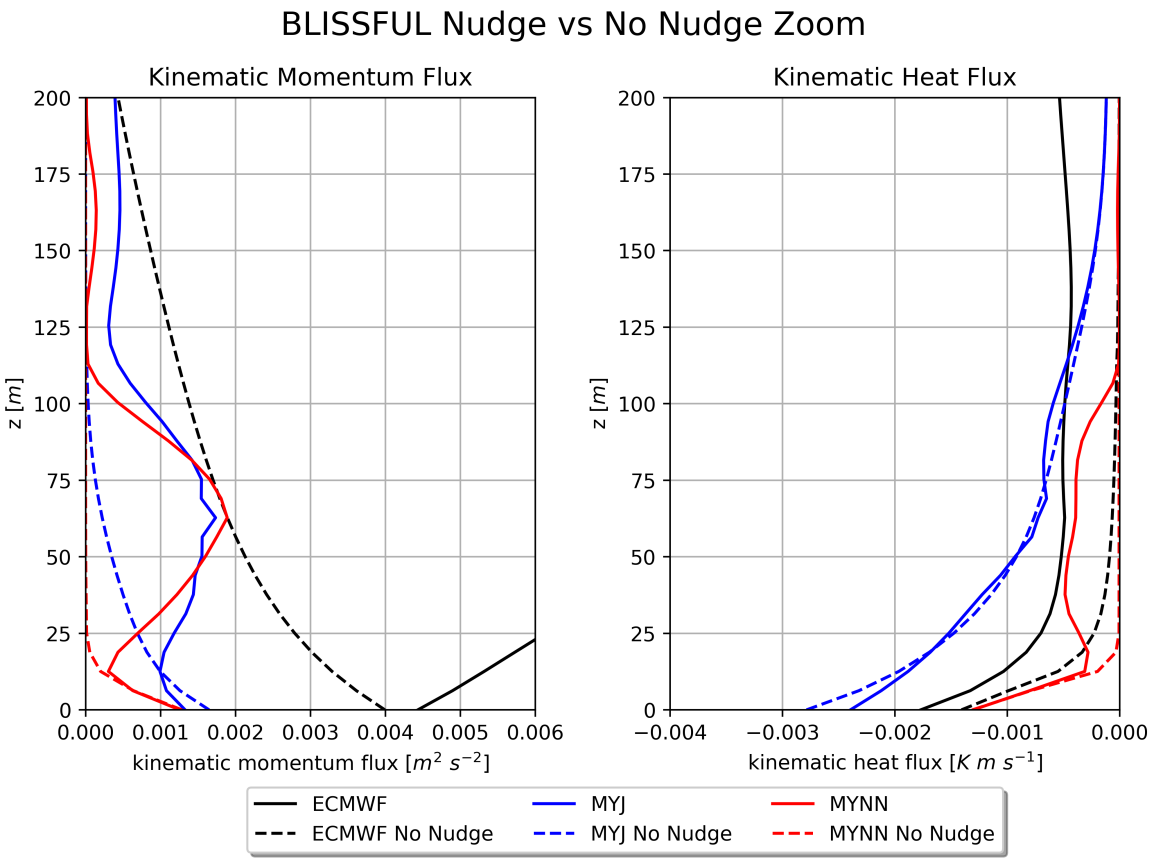

Figure 6.8: Same as previous but the vertical axis has changed to $z \in [0, 200]$.

With the surface temperature heterogeneity, no visible changes were seen in the vertical profiles of temperature or wind speed as seen in Figure 6.9 and 6.10, as well as Table 6.1. While differences were seen in the GABLS1 and GABLS2, the nudging procedure may be influencing the effects from the surface model. The first model level might be being over forced from the nudging procedure, limiting the influence from the temperature heterogeneity.

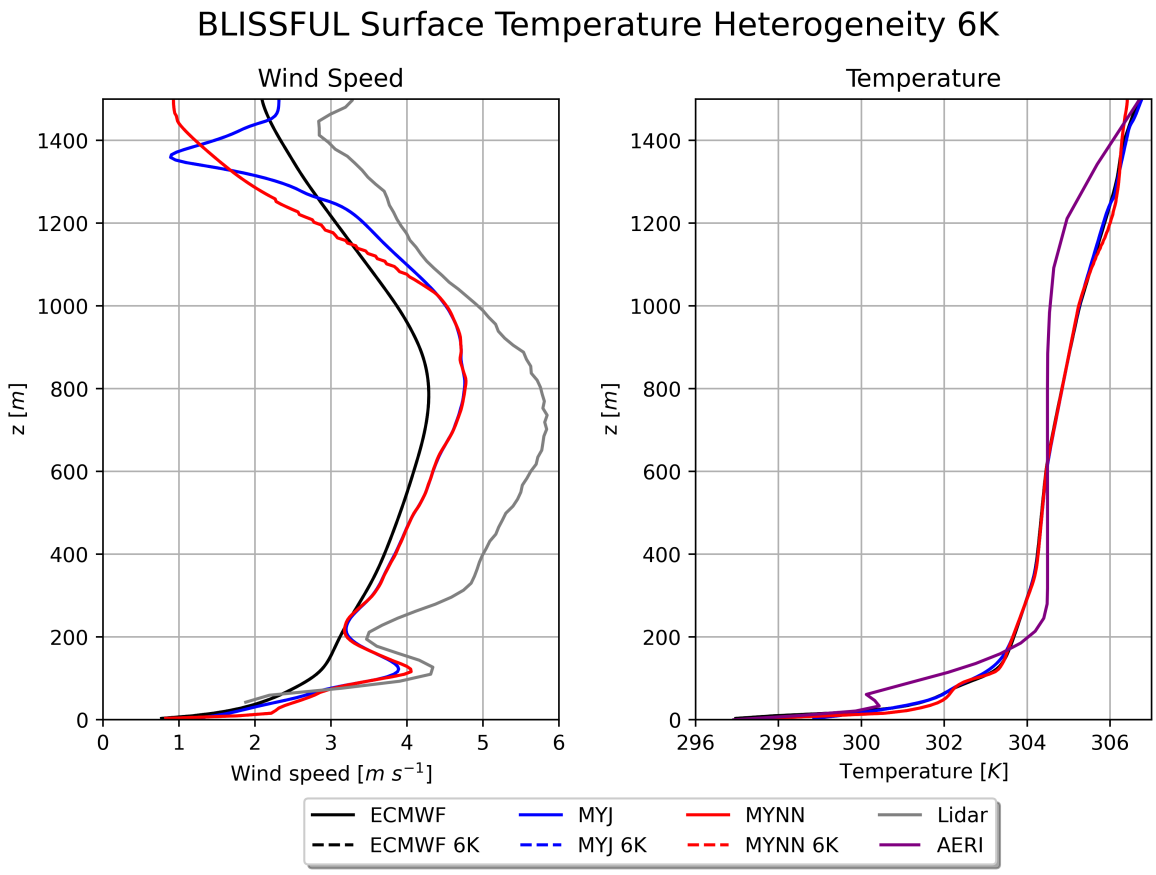

Figure 6.9: Vertical profiles of wind speed (left) and potential temperature (right) averaged over the final hour of the simulation for the homogeneous case (solid) and the TM with 6K patches (dashed). The ECMWF model is colored black, the MYJ blue, and the MYNN red.

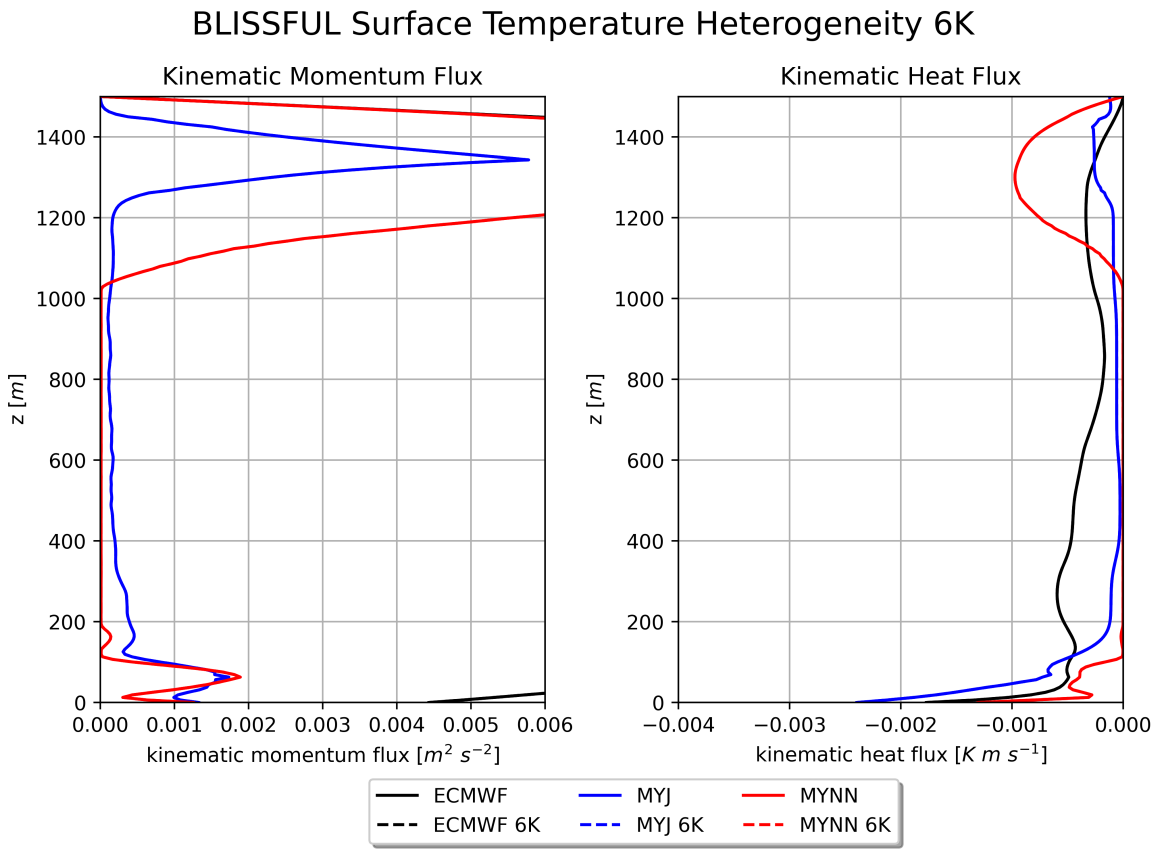

Figure 6.10: Vertical profiles of kinematic momentum flux (left) and kinematic heat flux (right) averaged over the final hour of the simulation for the homogeneous case (solid) and the TM with 6K patches (dashed). The ECMWF model is colored black, the MYJ blue, and the MYNN red.

Simulation Runs					
Case	h [m]	L [m]	u_* [ms^{-1}]	$\langle w'\theta' \rangle$ [Kms^{-1}]	$\langle u'w' \rangle$ [m^{2}s^{-2}]
ECMWF	1500.0	12.7	0.066	-0.0018	0.0044
ECMWF 3K	1500.0	12.7	0.066	-0.0018	0.0044
ECMWF 6K	1500.0	12.7	0.066	-0.0018	0.0044
ECMWF 6K Mod	1500.0	12.7	0.066	-0.0018	0.0044
MYJ	31.0	1.5	0.036	-0.0024	0.0013
MYJ 3K	31.0	1.5	0.036	-0.0024	0.0013
MYJ 6K	31.0	1.5	0.036	-0.0024	0.0013
MYJ 6K Mod	31.0	1.5	0.036	-0.0024	0.0013
MYNN	68.3	2.6	0.035	-0.0013	0.0013
MYNN 3K	68.3	2.6	0.035	-0.0013	0.0013
MYNN 6K	68.3	2.6	0.035	-0.0013	0.0013
MYNN 6K Mod	68.3	2.6	0.035	-0.0013	0.0013

Table 6.1: Mean values for the final hour of the simulation using surface temperature heterogeneity for the boundary layer height (h), Obukhov Length (L), friction velocity (u_*), surface heat flux ($\langle w'\theta' \rangle$) and surface momentum flux ($\langle u'w' \rangle$).

6.2.2 Time Series

Time-series traces of the friction velocity and surface kinematic heat flux show similar behavior across all PBL schemes (Figure 6.11). The friction velocity reaches a peak near $0.3\,\mathrm{m\,s^{-1}}$ and decreases to values less than $0.1\,\mathrm{m\,s^{-1}}$ for all cases. The surface heat fluxes have a minimum of $-0.02\,\mathrm{K\,m\,s^{-1}}$ that decrease in magnitude to $-0.0025\,\mathrm{K\,m\,s^{-1}}$. As was seen in the vertical profiles, the the plots of the surface temperature heterogeneity overlap with those from the homogeneous case. The ECMWF scheme has the largest friction velocity values throughout the simulation time, and also the largest in magnitude kinematic heat flux values. The boundary layer height and Obukhov length time series is plotted in Figure 6.12. The most stable PBL schemes are the MYJ and MYNN schemes with Obukhov lengths of around $L \approx 2\,\mathrm{m}$–$3\,\mathrm{m}$, while the ECMWF scheme is larger with $L \approx 12\,\mathrm{m}$.

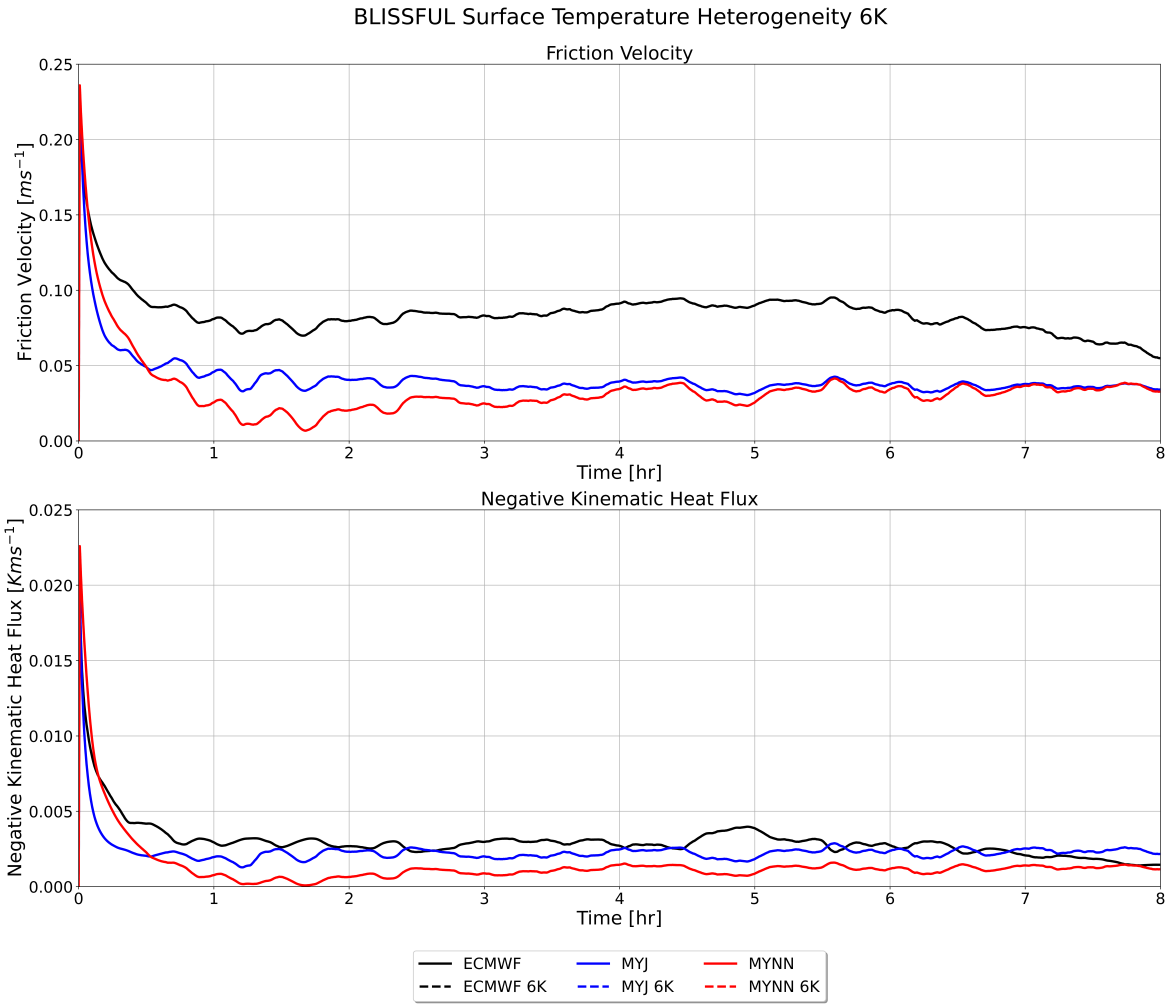

Figure 6.11: Time series of the friction velocity and surface kinematic heat flux with the homogeneous case (solid) and using the TM with 6K patches (dashed). The ECMWF model is colored black, the MYJ blue, and the MYNN red.

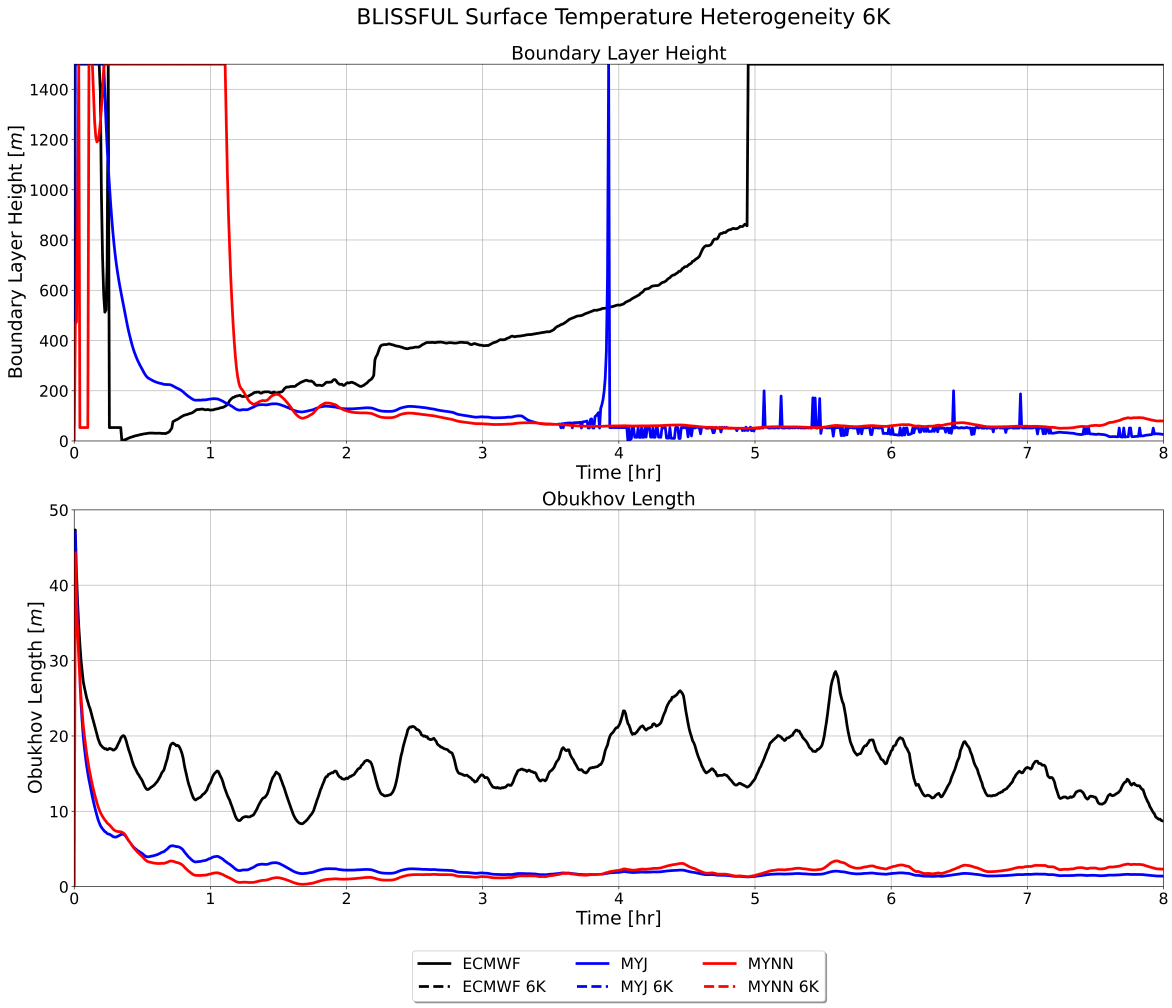

Figure 6.12: Time series of the boundary layer height and Obukhov length with the homogeneous case (solid) and using the TM with 6K patches (dashed). The ECMWF model is colored black, the MYJ blue, and the MYNN red.

6.3 Roughness Differences

While no differences were seen with the surface temperature heterogeneity, surface roughness heterogeneity was still tested. Vertical profiles of different surface roughness values for momentum for are shown in Figure 6.13. From a visual standpoint, there are

no differences between the roughness heterogeneity and the homogeneous case. This can be seen in Figures 6.13, 6.14 as all the values are the same as the homogeneous case. Upon closer inspection, there is a slight trend which can be seen in Table 6.2. This is the same trend seen before, where as the effective surface roughness values decreased, there was a decrease in the magnitude of the kinematic surface fluxes of heat and momentum. Related to this, there were also lower friction velocity values and a smaller Obukhov length, indicating more stable conditions. For the MYJ and MYNN case, the boundary layer height was much lower ($\approx 35\,\mathrm{m}$ - $65\,\mathrm{m}$) when compared to the ECMWF scheme ($\approx 1500\,\mathrm{m}$). While there are slight differences, these differences are out 10^{-3} and 10^{-4} decimal places, making their impact on the resultant profile negligible.

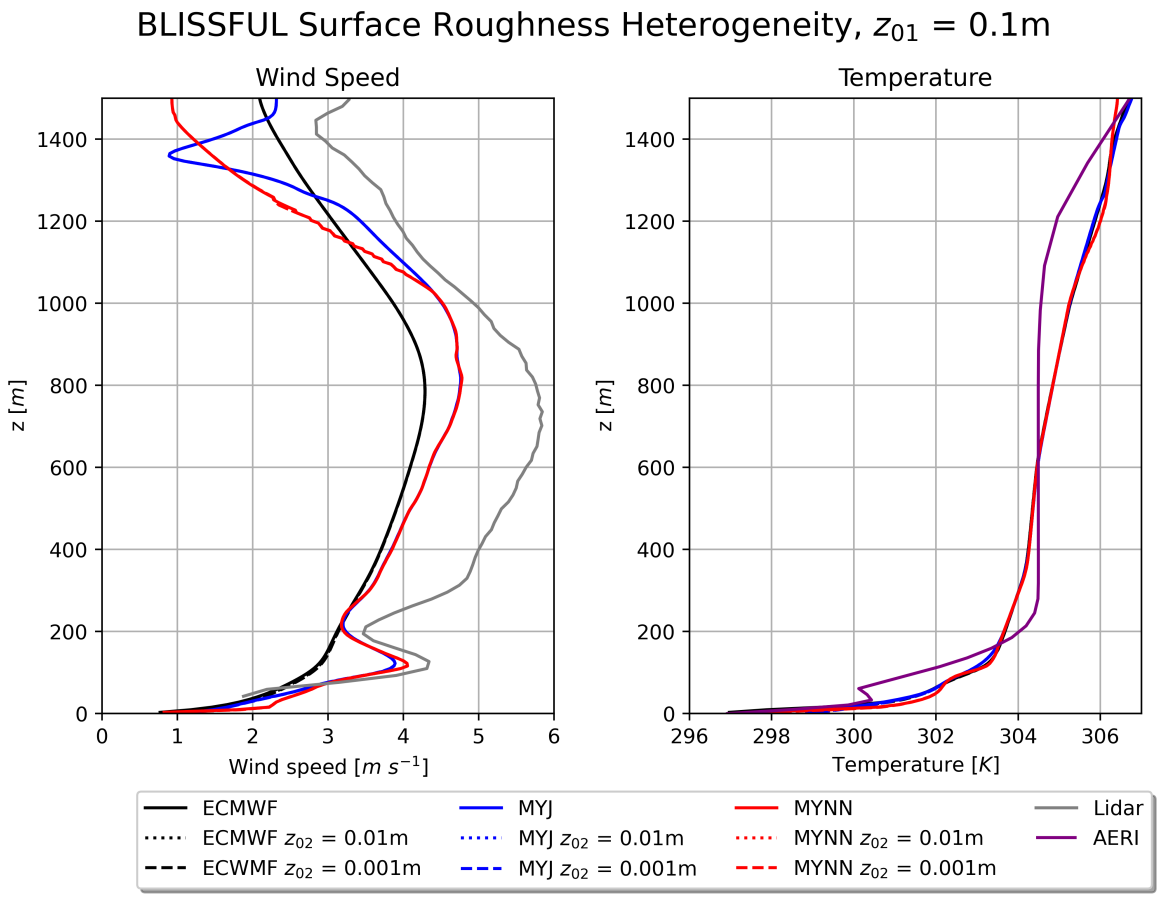

Figure 6.13: Vertical profiles of wind speed (left) and potential temperature (right) averaged over the final hour of the simulation with the homogeneous case (solid) and surface heterogeneity for patch values of $z_{02} = 0.01\,\mathrm{m}$ (dotted) and $z_{02} = 0.001\,\mathrm{m}$ (dashed). The ECMWF model is colored black, the MYJ blue, and the MYNN red.

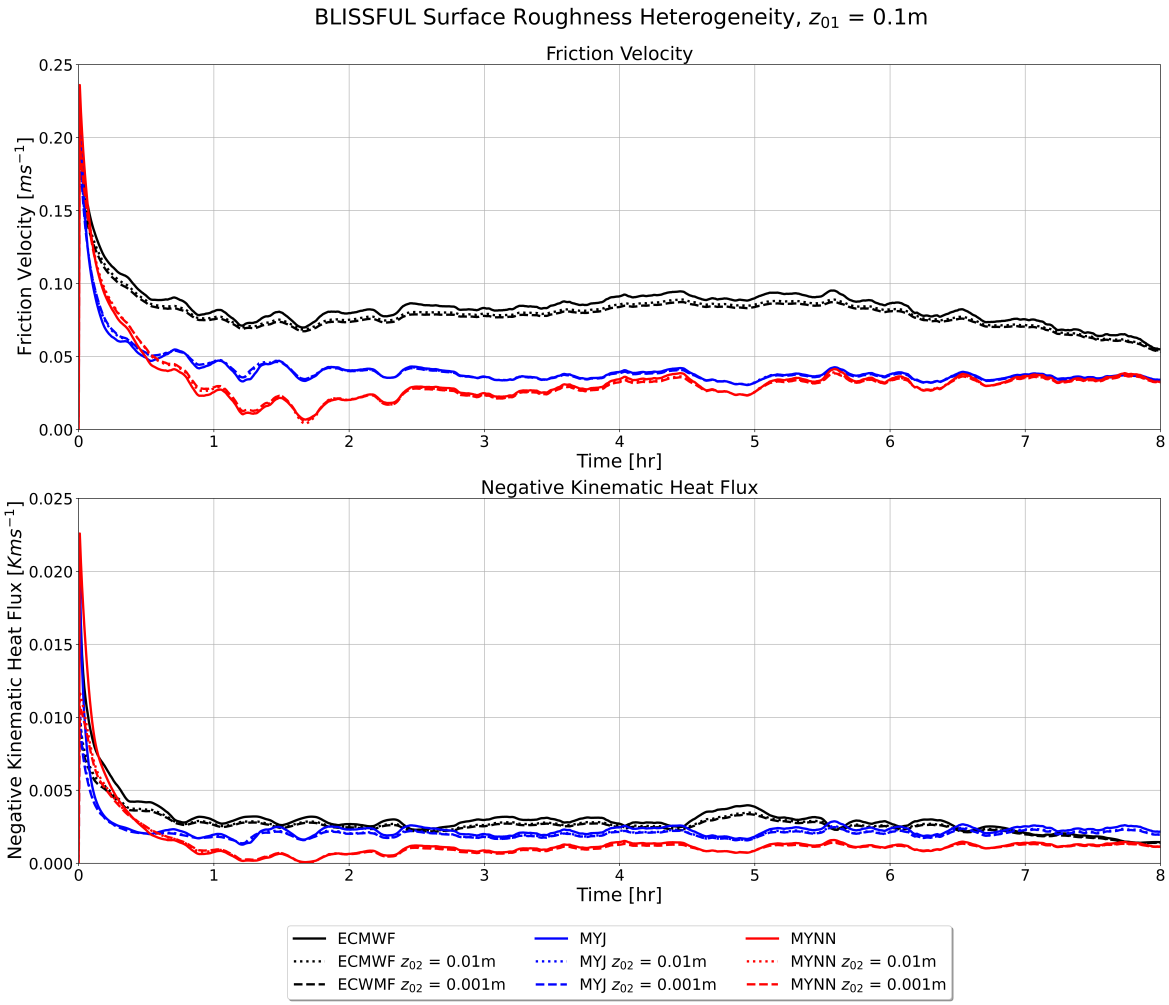

Figure 6.14: Time series of the friction velocity and surface kinematic heat flux with the homogeneous case (solid) and surface heterogeneity for patch values of $z_{02} = 0.01\,\mathrm{m}$ (dotted) and $z_{02} = 0.001\,\mathrm{m}$ (dashed). The ECMWF model is colored black, the MYJ blue, and the MYNN red.

Simulation Runs, $z_{01} = 0.1\,\mathrm{m}$						
Case	z_{0e} [m]	h [m]	L [m]	u_* [ms^{-1}]	$\langle w'\theta' \rangle$ [Kms^{-1}]	$\langle u'w' \rangle$[m^{2}s^{-2}]
ECWMF	0.1	1500.0	12.7	0.066	-0.0018	0.0044
ECWMF $z_{02} = 0.01\,\mathrm{m}$	0.0496	1500.0	11.6	0.064	-0.0017	0.0041
ECWMF $z_{02} = 0.001\,\mathrm{m}$	0.0387	1500.0	11.3	0.063	-0.0017	0.0040
MYJ	0.1	31.0	1.5	0.036	-0.0024	0.0013
MYJ $z_{02} = 0.01\,\mathrm{m}$	0.0496	35.3	1.6	0.036	-0.0022	0.0013
MYJ $z_{02} = 0.001\,\mathrm{m}$	0.0387	35.6	1.6	0.036	-0.0022	0.0013
MYNN	0.1	68.3	2.6	0.035	-0.0013	0.0013
MYNN $z_{02} = 0.01\,\mathrm{m}$	0.0496	64.1	2.5	0.035	-0.0013	0.0012
MYNN $z_{02} = 0.001\,\mathrm{m}$	0.0387	64.6	2.5	0.034	-0.0012	0.0012

Table 6.2: Mean values for the final hour of the simulation using z_0 heterogeneity for the effective roughness length (z_{0e}), boundary layer height (h), Obukhov Length (L), friction velocity (u_*), surface heat flux ($\langle w'\theta' \rangle$) and surface momentum flux ($\langle u'w' \rangle$). Here z_{01} is the roughness length for patch 1, and z_{02} for patch 2.

6.4 Discussion

The BLISSFUL simulation without using the nudging procedure had very poor results. There was almost no vertical mixing which resulted in almost no change from the initial profiles. When using the nudging procedure, the results from the simulation drastically improved. Without the nudging procedure the SCM was not able to reproduce the key features observed from the LIDAR such as the LLJ. The nudging procedure acts like a rubber band to the SCM simulation, gradually influencing u, v, and θ towards observed values. The relaxation time scale α was tested from $\alpha = 3600\,\mathrm{s}$ to $\alpha = 10.800\,\mathrm{s}$. Smaller values of α over forced the simulation and made the simulation values of u, v, and θ to be equal to the observations. To bring the solution towards reality, the value was increased to $\alpha = 10.800\,\mathrm{s}$. This improved the simulation results but did not over force them to the same degree as $\alpha = 3600\,\mathrm{s}$.

The dominance of the nudging procedure may provide a reason for why the fluxes are so small. At the beginning of the simulation, there is a very large imbalance seen between the observations and the model initializations. With the primary forcing being driven by the observation, the modeled fluxes will then be changing based up the conditions being forced to it. This could lead to erroneous values in the kinematic fluxes, while still having good results in the temperature and wind profiles.

While the nudging procedure greatly improves the results, there are still differences between the observations and the simulations. The MYJ and MYNN schemes almost exactly overlap one another for a majority of the modeled domain, which may give some reason to the strange behavior in the fluxes. The forcing terms seem to be dominated by the nudging force, as the fluxes for momentum and heat go to zero fairly quickly, except for the ECMWF case which is an outlier.

As noted in the introduction of the case, outflow boundaries from dissipating thunderstorms came through the area resulting in the sharp temperature drop. This played a major factor in disrupting the clear diurnal transition to stable conditions. Mesoscale influences were a much larger factor here during this period, which is important to consider when trying to understand how to initialize the model and interpret results. The mesoscale influences undoubtedly disturbed the atmosphere and makes the BLISSFUL case not as ideal as GABLS1 or GABLS2. It is hard to compare the BLISSFUL case to the other two due to the setup and testing that is still needed to determine proper initial conditions for the case.

Chapter 7

Summary and Conclusions

7.1 Closing Remarks

The OU-NSSL SCM reproduced results that were in the range from previous well-cited atmospheric boundary layer studies encompassing stable and diurnally evolving such as GABLS1 and GABLS2. When incorporating various surface temperature heterogeneity, similar trends were seen across all PBL schemes. The momentum fluxes increased in magnitude with the temperature differences, and this was most significant in the 6K case. A different trend was noted in the heat fluxes, with smaller in magnitude differences associated with increasing temperature heterogeneity. The increase in the surface momentum flux led to slightly more mixing and a higher boundary layer height. With smaller surface heat flux values, the surface temperatures did not cool as significantly, which led to slightly warmer temperature profiles.

Results from using the MTM showed the improvement of the surface heat flux values with the modifications made to the stability functions. The values for the kinematic fluxes were between the homogeneous case and the TM which was expected. This decrease is associated with better heat flux estimation from the stable (cooler) patch, which was seen in the GABLS1 and GABLS2 cases. The effectiveness of the MTM is seen across all of the PBL schemes investigated.

With differences in surface roughness, changes were also prevalent in the profiles of temperature and wind speed. As the surface roughness values tested were decreased, a

decrease in the height of the LLJ was noted as well as the inversion height of temperature. These changes were related to the decrease in surface fluxes of both heat and momentum, which was a result of the smaller effective surface roughness values.

Comparing the two different types of surface heterogeneity, surface temperature and surface roughness, is not straightforward. The differences in surface roughness seem to affect the fluxes of heat and momentum nearly equally, which decrease with decreasing effective roughness. Investigating the TM with temperature heterogeneity, the 3K case had large changes in the surface heat fluxes, but only minimal changes in the surface momentum flux. It seems as though the momentum fluxes become more influenced by larger surface temperature heterogeneities. More temperature differences could be used to further test surface temperature heterogeneity influence.

Compared to the GABLS1 case, the GABLS2 adds more complexity with a complicated changing surface temperature, an additional value for z_{0h}, and the addition of large-scale forcing. With all of these additional factors, the SCM performed well when simulating a complex case with a full diurnal cycle. The simulations from both PBL schemes fell in line with those from the range of SCM simulations from GABLS2. The ECMWF scheme was near the center of the spread of the simulations, while the MYNN was on the warmer edge of the spread from the SCM simulations.

Results from the BLISSFUL case match the observation at KAEFS well when using the nudging technique. The simulations develop a LLJ that matches the general shape to the observations from the LIDAR. This is strongly influenced by the use of the nudging technique. The simulations without the nudging factor did not mix vertically and did not develop the LLJ at $800m$, but instead had a constant wind with height. While the BLISSFUL case was not an idealized setup like the previous GABLS1 and GABLS2 cases, more fine tuning is being done to improve the forcing for the model.

Based on this work, the MTM incorporated surface heterogeneity while improving the surface kinematic flux estimations. The TM was shown to have very large values with the strongest temperature heterogeneity of 6K. The MTM corrected for this and relaxed be improving the surface kinematic heat flux estimation of the colder (stable) patch. The scheme would pair best with the MYNN PBL scheme, which for the GABLS1 case was the best performing scheme. The MYNN also performed well in the GABLS2 when, notably having a better representation of the boundary layer profiles of temperature and wind speed when compared to the ECMWF scheme. These results may change if MYJ could be incorporated into the GABLS2 case, but for now the results would indicate MYNN performing the best.

7.2 Future Work

Additional features to the OU-NSSL SCM can be added to possibly improve results. First, an equation for water vapor, q, can be added to the SCM as a prognostic variable. With the addition of q the potential temperature now has an additional term to account for water vapor, leaving us with the virtual potential temperature. This has the most affect through the Obukhov length which is connected to the virtual potential temperature flux. With this there are also new stability functions for those with moisture. This additional prognostic variable to the SCM could improve the results seen in the GABLS2 simulations, as q was used in the GABLS2 simulations from Svensson et al. (2011).

The addition of an adaptive time-stepping scheme is of interest to correct the numerical stability issues that arose in the GABLS2 case. The adaptive time-stepping would eliminate the need to guess the correct time step to keep a stable numerical

solution. This is done by changing the time step based on the diffusion number of the simulated flow.

The SCM currently has a basic implementation of the blending height and effective surface roughness calculations. The blending height and surface roughness can add in the effects of stability through a stability correction term from Wood and Mason (1991). This would improve the blending height corrections by accounting for stability, but also by adding in the surface heat flux into the calculation for the blending height. This may give a better estimate for the blending height for when surface temperature heterogeneity is being used with the TM and MTM.

The PBL models considered herein can also be expanded. Currently the higher-order schemes implemented are the MYJ and MYNN schemes, both local in nature. With a PBL scheme such as the Yonsei University (YSU) (Hong 2010) scheme, further analysis can be done to understand how the surface fluxes change using a non-local scheme. Additional schemes such as the quasi-normal scale elimination (QNSE) (Sukoriansky et al. 2005) could also be implemented to see if these same trends can be seen across different types of PBL schemes.

Reference List

Avissar, R., and R. A. Pielke, 1989: A parameterization of heterogeneous land surfaces for atmospheric numerical models and its impact on regional meteorology. *Monthly Weather Review*, **117 (10)**, 2113 – 2136, https://doi.org/10.1175/1520-0493(1989)117⟨2113:APOHLS⟩2.0.CO;2.

Beare, R. J., and Coauthors, 2006: An intercomparison of large-eddy simulations of the stable boundary layer. *Boundary-Layer Meteorology*, **118 (2)**, 247–272, https://doi.org/10.1007/s10546-004-2820-6.

Beljaars, A., 2002: The parametrization of the planetary boundary layer. ECMWF, URL https://www.ecmwf.int/node/16959.

Bogenschutz, P. A., S. Tang, P. M. Caldwell, S. Xie, W. Lin, and Y.-S. Chen, 2020: The E3SM version 1 single-column model. *Geoscientific Model Development*, **13 (9)**, 4443–4458, https://doi.org/10.5194/gmd-13-4443-2020.

Brock, F. V., K. C. Crawford, R. L. Elliott, G. W. Cuperus, S. J. Stadler, H. L. Johnson, and M. D. Eilts, 1995: The oklahoma mesonet: A technical overview. *Journal of Atmospheric and Oceanic Technology*, **12 (1)**, 5 – 19, https://doi.org/10.1175/1520-0426(1995)012⟨0005:TOMATO⟩2.0.CO;2.

Clarke, R. H., A. J. Dyer, R. Brook, D. Reid, and A. Troup, 1971: The Wangara experiment: Boundary layer data. Tech. Rep. 19, Div. Meteor. Phys. CSIRO, Australia.

Crawford, K., R. Mcpherson, C. Fiebrich, and R. Elliott, 2007: Statewide monitoring of the mesoscale environment: A technical update.

Curry, J. A., J. O. Pinto, T. Benner, and M. Tschudi, 1997: Evolution of the cloudy boundary layer during the autumnal freezing of the beaufort sea. *Journal of Geophysical Research: Atmospheres*, **102 (D12)**, 13 851–13 860, https://doi.org/https://doi.org/10.1029/96JD03089.

Cuxart, J., and Coauthors, 2006: Single-column model intercomparison for a stably stratified atmospheric boundary layer. *Boundary-Layer Meteorology*, **118 (2)**, 273–303, https://doi.org/10.1007/s10546-005-3780-1.

Deardorff, J. W., 1970: Convective velocity and temperature scales for the unstable planetary boundary layer and for Rayleigh convection. *Journal of Atmospheric Sciences*, **27 (8)**, 1211 – 1213.

Dyer, A. J., and B. B. Hicks, 1970: Flux-gradient relationships in the constant flux layer. *Quarterly Journal of the Royal Meteorological Society*, **96 (410)**, 715–721, https://doi.org/https://doi.org/10.1002/qj.49709641012.

Gunawardena, N., E. R. Pardyjak, R. Stoll, and A. Khadka, 2018: Development and evaluation of an open-source, low-cost distributed sensor network for environmental monitoring applications. *Measurement Science and Technology*, **29 (2)**, 024 008, https://doi.org/10.1088/1361-6501/aa97fb.

Hong, S.-Y., 2010: A new stable boundary-layer mixing scheme and its impact on the simulated east asian summer monsoon. *Quarterly Journal of the Royal Meteorological Society*, **136 (651)**, 1481–1496, https://doi.org/https://doi.org/10.1002/qj.665.

Janjic, Z., 2002: Nonsingular implementation of the mellor–yamada level 2.5 scheme in the ncep meso model. *NCEP Office Note*, **436**.

Kosović, B., and J. A. Curry, 2000: A large eddy simulation study of a quasi-steady, stably stratified atmospheric boundary layer. *Journal of the Atmospheric Sciences*, **57 (8)**, 1052 – 1068, https://doi.org/10.1175/1520-0469(2000)057⟨1052:ALESSO⟩2.0.CO;2.

Lee, W., 2011: Tridiagonal matrices: Thomas algorithm. *MS6021, Scientific Computation, University of Limerick*.

Louis, J.-F., M. Tiedtke, and J.-F. Geleyn, 1982: A short history of the pbl parameterization at ecmwf. *Workshop on Planetary Boundary Layer parameterization, 25-27 November 1981*, ECMWF, Shinfield Park, Reading, ECMWF, 59-79.

Mason, P. J., 1988: The formation of areally-averaged roughness lengths. *Quarterly Journal of the Royal Meteorological Society*, **114 (480)**, 399–420, https://doi.org/https://doi.org/10.1002/qj.49711448007.

Mason, P. J., 1989: Large-eddy simulation of the convective atmospheric boundary layer. *Journal of Atmospheric Sciences*, **46 (11)**, 1492 – 1516, https://doi.org/10.1175/1520-0469(1989)046⟨1492:LESOTC⟩2.0.CO;2.

Mellor, G. L., and T. Yamada, 1974: A hierarchy of turbulence closure models for planetary boundary layers. *Journal of Atmospheric Sciences*, **31 (7)**, https://doi.org/10.1175/1520-0469(1974)031⟨1791:AHOTCM⟩2.0.CO;2".

Mellor, G. L., and T. Yamada, 1982: Development of a turbulence closure model for geophysical fluid problems. *Reviews of Geophysics*, **20 (4)**, 851–875, https://doi.org/https://doi.org/10.1029/RG020i004p00851.

Miller, N. E., and R. Stoll, 2013: Surface heterogeneity effects on regional-scale fluxes in the stable boundary layer: Aerodynamic roughness length transitions. *Boundary-Layer Meteorology*, **149 (2)**, 277–301, https://doi.org/10.1007/s10546-013-9839-5.

Monin, A. S., and A. M. Obukhov, 1954: Basic laws of turbulent mixing in the ground layer of the atmosphere. *Contrib. Geophys. Inst. Acad. Sci.*, **151**, 163–187.

Nakanishi, M., 2001: Improvement of the Mellor–Yamada turbulence closure model based on large-eddy simulation data. *Boundary-Layer Meteorology*, **99 (3)**, 349–378, https://doi.org/10.1023/A:1018915827400.

Nakanishi, M., and H. Niino, 2004: An improved Mellor–Yamada level-3 model with condensation physics: Its design and verification. *Boundary-Layer Meteorology*, **112**, 1–31, https://doi.org/10.1023/B:BOUN.0000020164.04146.98.

Nakanishi, M., and H. Niino, 2006: An improved Mellor–Yamada level-3 model: Its numerical stability and application to a regional prediction of advection fog. *Boundary-Layer Meteorology*, **119 (2)**, 397–407, https://doi.org/10.1007/s10546-005-9030-8.

Nakanishi, M., and H. Niino, 2009: Development of an improved turbulence closure model for the atmospheric boundary layer. *Journal of the Meteorological Society of Japan. Ser. II*, **87 (5)**, 895–912, https://doi.org/10.2151/jmsj.87.895.

Nieuwstadt, F. T. M., 1984: The turbulent structure of the stable, nocturnal boundary layer. *Journal of Atmospheric Sciences*, **41 (14)**, 2202 – 2216.

Prandtl, L., 1925: 7. bericht über untersuchungen zur ausgebildeten turbulenz. *ZAMM - Journal of Applied Mathematics and Mechanics / Zeitschrift für Angewandte Mathematik und Mechanik*, **5 (2)**, 136–139.

Skamarock, W. C., J. B. Klemp, J. Dudhia, D. O. Gill, Z. Liu, J. Berner, and X. Huang, 2021: A description of the advanced research WRF model version 4.3. Tech. Rep. NCAR/TN-556+STR, NCAR. https://doi.org/10.5065/1dfh-6p97.

Stoll, R., and F. Porté-Agel, 2009: Surface heterogeneity effects on regional-scale fluxes in stable boundary layers: Surface temperature transitions. *Journal of the Atmospheric Sciences*, **66 (2)**, 412 – 431, https://doi.org/10.1175/2008JAS2668.1.

Stull, R. B., 1988: *An Introduction to Boundary Layer Meteorology*. Kluwer Academic Publishing.

Sukoriansky, S., B. Galperin, and V. Perov, 2005: Application of a new spectral theory of stably stratified turbulence to the atmospheric boundary layer over sea ice. *Boundary-Layer Meteorology*, **117 (2)**, 231–257, https://doi.org/10.1007/s10546-004-6848-4.

Svensson, G., and Coauthors, 2011: Evaluation of the diurnal cycle in the atmospheric boundary layer over land as represented by a variety of single-column models: The second GABLS experiment. *Boundary-Layer Meteorology*, **140 (2)**, 177–206, https://doi.org/10.1007/s10546-011-9611-7.

Williamson, J., 1980: Low-storage runge-kutta schemes. *Journal of Computational Physics*, **35 (1)**, 48–56, https://doi.org/https://doi.org/10.1016/0021-9991(80)90033-9.

Wood, N., and P. J. Mason, 1991: The influence of static stability on the effective roughness lengths for momentum and heat transfer. *Quarterly Journal of the Royal Meteorological Society*, **117**, 1025–1056.